RCA REVIEW

a technical journal

Published quarterly by
RCA LABORATORIES
in cooperation with all subsidiaries and divisions of
RADIO CORPORATION OF AMERICA

VOLUME XXVII | MARCH 1966 | NUMBER 1

CONTENTS

RCA REVIEW is regularly abstracted and indexed by *Abstracts of Photographic Science and Engineering Literature, Applied Science and Technology Index, Bulletin Signalétique des Télécommunications, Chemical Abstracts, Electronic and Radio Engineer, Mathematical Reviews, and Science Abstracts* (I.E.E.-Brit.).

RCA REVIEW

THE TIROS IX WHEEL SATELLITE

By

A. Schnapf

RCA Astro-Electronics Division
Princeton, N. J.

Summary—This paper describes the design and performance of the TIROS IX satellite. This satellite employs a "wheel configuration" in which the spin axis is normal to the orbital plane rather than parallel to it as had been the case for previous TIROS satellites. The television camera system and photocoverage are described, as are the various control systems, including a refined magnetic attitude control system. The performance of previous TIROS satellites is reviewed and the TIROS Operational System (TOS) is discussed.

Introduction

TIROS is the designation of a series of earth-orbiting satellites that supply television and infrared information on cloud cover that is used for meteorological purposes. As of February 15, 1966, eleven such satellites had been launched and successfully operated. TIROS satellites are spin-stabilized, hat-box-shaped spacecraft 42 inches in diameter, 22 inches high, and weighing approximately 300 pounds. The first eight satellites were in the so-called standard configuration, in which the two television cameras are pointed parallel to the spin axis of the satellite, as shown in the bottom of Figure 1. A satellite in this configuration is launched with its spin axis essentially parallel to the orbital plane and remains in this attitude throughout its operational life. With this arrangement, the cameras view earth during only one segment of each orbit.

TIROS IX uses a "wheel" configuration. In this case, the satellite is launched with the same attitude as in the standard configuration, but a special attitude maneuver is initiated shortly after launch in order to position the spin axis to be *normal* to the orbital plane. Once this attitude is achieved, the satellite appears to roll along its orbit—hence, the designation wheel-configuration—and its cameras view earth once during each rotation. As shown in Figure 1, the television cameras are pointed radially. In this configuration, the satellite can take pictures at any point in its orbit, provided ground illumination

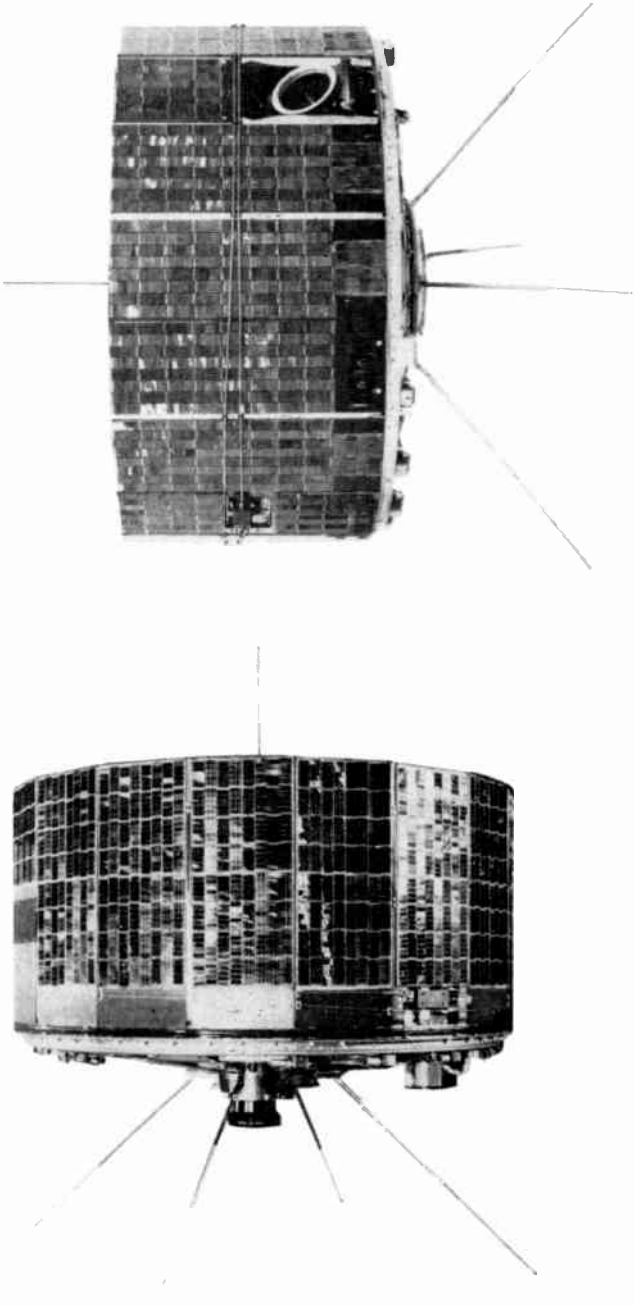

Fig. 1—The TIROS Satellite. The "wheel" configuration is shown above, standard configuration below.

is adequate. As can be seen in Figure 2, wheel-configuration satellites provide the advantage of greatly increased photocoverage compared to satellites of the standard-configuration. TIROS IX is basically a research and development spacecraft that utilizes proven technology wherever possible. TIROS IX includes the same basic subsystems as the other TIROS satellites, but more refined dynamics control and command and control subsystems are necessary.

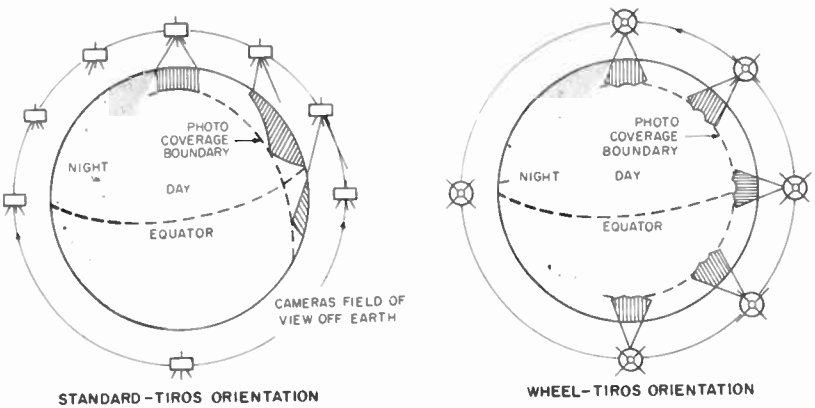

Fig. 2—Comparison of photocoverage provided by standard mode (left) and wheel mode (right) TIROS satellites.

Satellite Design

The primary objectives of the TIROS IX system were to demonstrate operational feasibility of the basic concepts for the forthcoming TIROS Operational System (TOS), namely, the use of a wheel-mode satellite to obtain contiguous photocoverage of the entire surface of the earth on a daily basis, and the utilization of such data on an operational basis. To meet these objectives and to take maximum advantage of the increased capabilities afforded by the wheel-mode of operation, TIROS IX was designed for operation in a near-polar circular orbit, having an altitude of 400 nautical miles and an inclination of 98.4 degrees. This combination of orbital altitude and inclination was selected to provide a sun-synchronous orbit, i.e., an orbit in which the orbital plane revolves about the earth's polar axis with the same velocity at which the earth rotates about the sun, and to extend the area of photocoverage. The primary advantage of such an orbit is that the solar illumination on the portions of the earth directly beneath the satellite remains essentially constant on each orbit and, thus, each

television picture has essentially the same scene brightness. Due to a malfunction during launch, however, TIROS IX did not achieve a sun-synchronous orbit.

Figure 3 is a functional block diagram of the TIROS IX satellite, while Figure 4 shows the components mounted on the baseplate. The salient features of the system design are the inclusion of a relatively simple but effective magnetic attitude-control system to provide precise control of attitude, and a camera-triggering system to ensure that the cameras take pictures only when they view the area of the earth directly beneath the satellite.

Dynamics-Control System

The magnetic attitude-control system comprises part of the dynamics control subsystem, which also includes nutation dampers, a despin mechanism, and spin-control devices. The nutation dampers are used to achieve spin-axis stability after separation from the third-stage rocket, and to maintain stability despite small disturbances that might be experienced during orbital operation. Each of the two dampers consists of a small sliding mass that is automatically uncaged when the satellite separates from the launch vehicle and allowed to oscillate back and forth along a curved track whose chord is parallel to the satellite spin axis. Friction between the oscillating mass and the monorail dissipates the nutational energy and reduces satellite "wobble" to less than 0.5 degree. These mechanisms are located diametrically opposite each other on the inside walls of the satellite "hat" to provide optimum mechanical balance.

The despin mechanism, consisting of a pair of one-pound weights attached to steel cables wrapped about the periphery of the hat, is used to reduce the satellite spin rate from the orbit injection rate of 125 rpm to an operational rate of 8 to 12 rpm. To achieve despin, the weights and cables are automatically released shortly after the satellite separates from the launch vehicle. Centrifugal force unwraps the weights and cables from the satellite, and they are cast off into space. The resulting energy loss accomplishes the desired spin-rate reduction within one-half second.

The magnetic attitude control system includes both a Quarter Orbit Magnetic Attitude Control (QOMAC) device and a Magnetic Bias Control (MBC) device, as well as attitude-sensing devices. The operation of the QOMAC and MBC devices is based on the generation of controlled electromagnetic fields that interact with the earth's magnetic field to develop a torque that will precess the spin axis to a desired position.

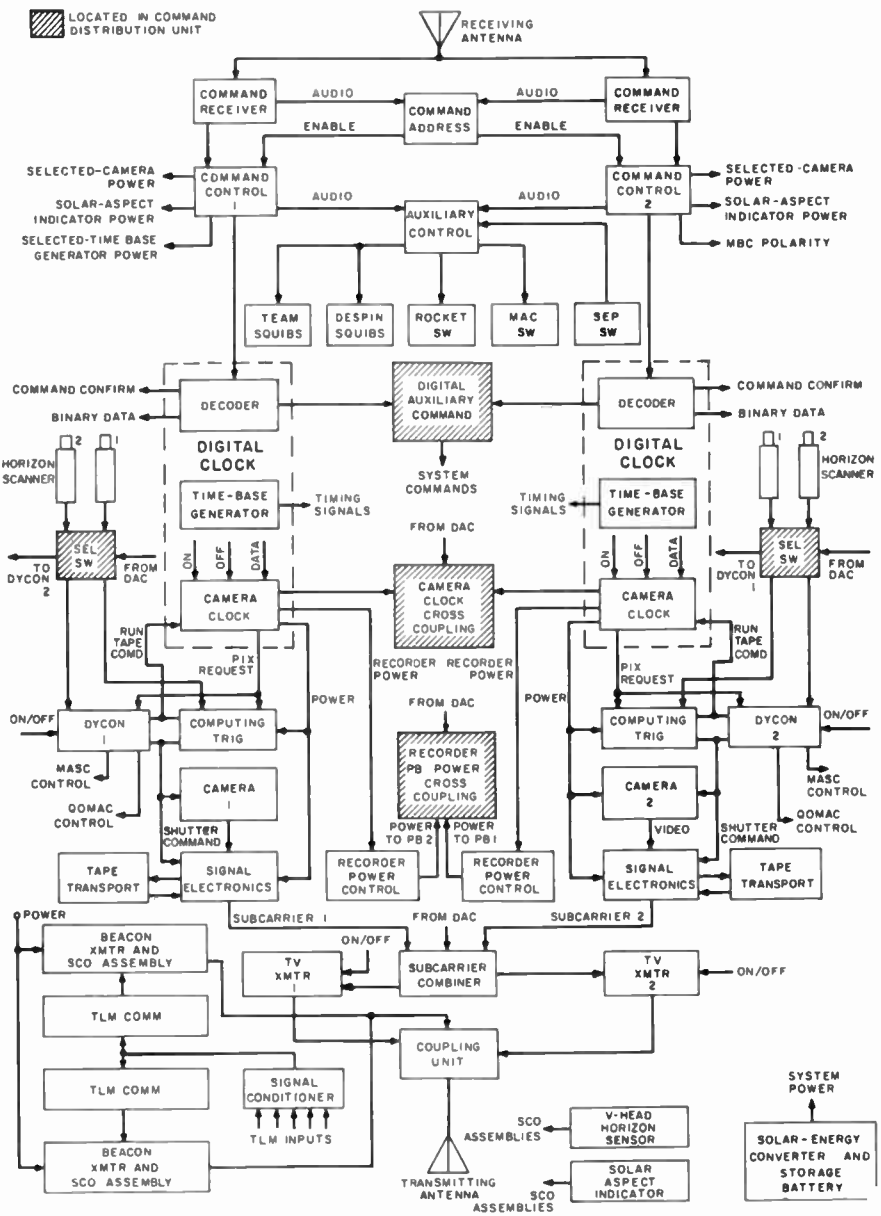

Fig. 3—Functional block diagram of TIROS IX satellite.

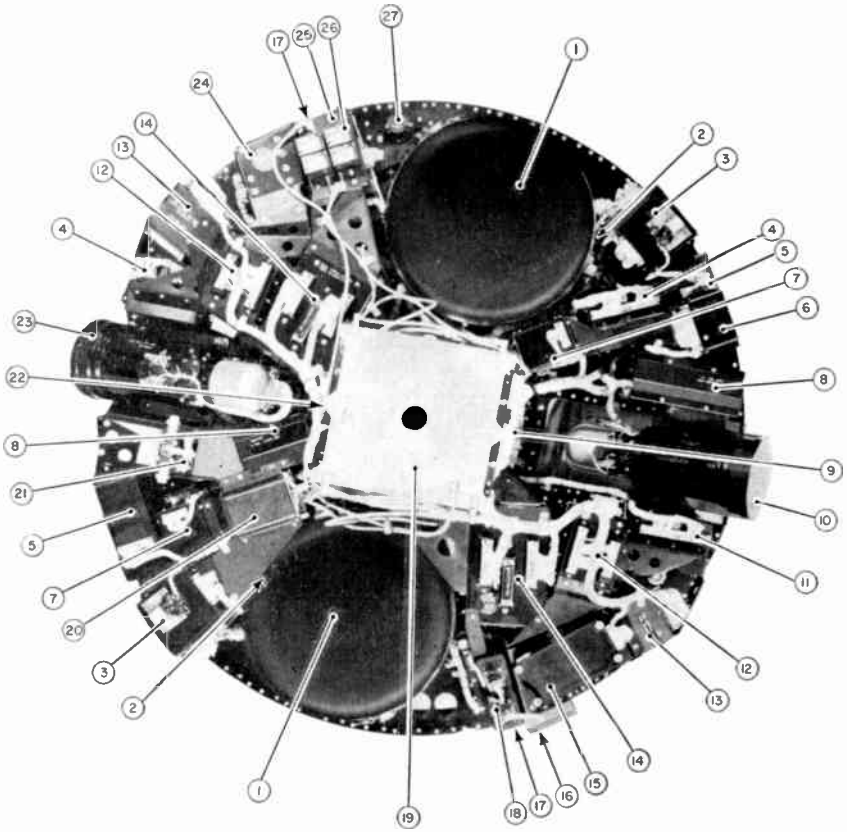

1. Tape Recorder
2. Power Control Unit (Hidden)
3. Recorder Electronics
4. Command Control
5. Recorder Power Converter
6. MBC Switch
7. Voltage Regulator
8. Camera Electronics
9. Command Distribution Unit
10. TV Camera No. 2 (Viewing 26.5° Upward)
11. Auxiliary Control
12. Dycon
13. Computing Trigger
14. Digital Clock
15. Power Supply Protection Unit (Hidden)
16. Solar Aspect Indicator (With Cover)
17. Two Orthogonal Horizon Sensors (Hidden)
18. Solar Aspect Indicator Electronics
19. Antenna Coupling Network
20. TV Transmitters and Video Coupling Network
21. Command Receivers
22. Battery Pack (Hidden)
23. TV Camera No. 1 (Viewing 26.5° Downward)
24. Telemetry Commutators and Signal Conditioner
25. Beacon Transmitters
26. Subcarrier Oscillators
27. V-Head Attitude Sensor

Fig. 4—Components Mounted on TIROS IX Baseplate

The MBC device, which is essentially identical to the magnetic attitude control device employed on TIROS II through VIII, consists primarily of a coil of wire and a stepping switch to regulate the amount and direction of the current in the coil. Its primary function is to provide for the generation of a selectable, constant electromagnetic field whose dipole moment is colinear with the satellite's spin axis, as shown in Figure 5. The magnitude and polarity of the dipole moment

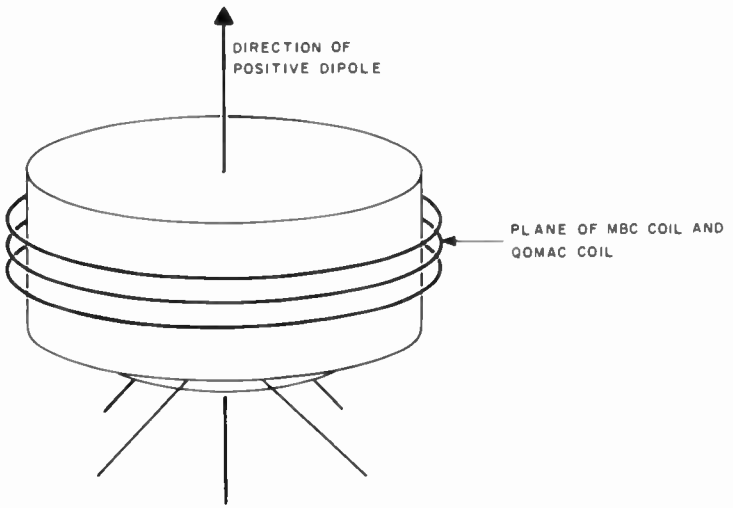

Fig. 5—Orientation of attitude coil.

can be controlled by ground command to compensate for the satellite's residual dipole moment (due to ferromagnetic materials used in its construction) and to provide approximately a 1-degree per day shift in spin-axis attitude. With this shift in attitude, the satellite tracks the regression of the orbital plane in a sun-synchronous orbit, thus reducing the number of QOMAC operations required for station keeping, i.e., maintaining the wheel orientation.

Like the MBC device, the QOMAC device affords control over the satellite's attitude by generating controllable electromagnetic fields that interact with the earth's magnetic field. However, provisions are also made for reversing the dipole moment generated by this device at quarter-orbit intervals, for selecting between one and sixteen consecutive QOMAC cycles (1 cycle consists of 1 quarter orbit of positive dipole followed by 1 quarter orbit of negative dipole), and for selecting the point in orbit at which the first QOMAC cycle will begin. The

combined effect of these capabilities, which are made possible by the enhanced command and control equipment carried by TIROS IX, permits the selection of a precession axis such that the spin axis can be moved to and maintained in the desired attitude.

The QOMAC device, therefore, must provide two capabilities: (1) precise maintenance of the wheel attitude, and (2) rapid and efficient achievement of the proper wheel attitude after the satellite is injected into orbit. To meet these two requirements, the QOMAC device has two modes of operation, namely, a high-torque mode for achieving gross attitude changes, such as those required during the initial wheel-orientation maneuver, and a low-torque mode for station keeping. In the high-torque mode, the QOMAC device generates a dipole moment of 30 ampere-turns-meter^2. At the planned orbital altitude of 400 nautical miles, this value of dipole moment provides a spin-axis precession of approximately 10 degrees per orbit, allowing the orientation maneuver to be completed in approximately 14 orbits. The low-torque mode of operation provides a dipole moment of 6 ampere-turns-meter^2, which provides a spin-axis precession of approximately 2 degrees per orbit. In normal station-keeping operations, with the MBC device set to provide the 1 degree per day movement described previously, the QOMAC device need be energized only once every 4 or 5 days. Thus, the average power consumed by the QOMAC device is very low.

To permit the attitude of the satellite to be closely monitored, two separate attitude sensors are employed. The primary sensor, a V-head horizon sensor, consists of infrared (IR) bolometers whose optical axes intersect at an included angle of 100 degrees. These bolometers are mounted on the baseplate in such a way that when the satellite is in the correct attitude, i.e., "on station," their optical axes "sweep out" equal cones in space and intersect the earth for equal periods. Similarly, when the satellite is not on station, i.e., when an attitude error exists, the optical axis of one sensor intersects the earth for a longer period than that of the other and provides an output of longer duration. The outputs of the two IR sensors are telemetered to ground and recorded to provide a presentation similar to that shown in Figure 6.

Because TIROS is spin stabilized, an attitude error consists of two components that are 90 degrees out of phase and that vary sinusoidally. Because of this variation, and since only one component, the roll component, can be detected by the V-head sensor, approximately 10 minutes of consecutive data are required to accurately determine the satellite's attitude and what, if any, corrective measures are necessary.

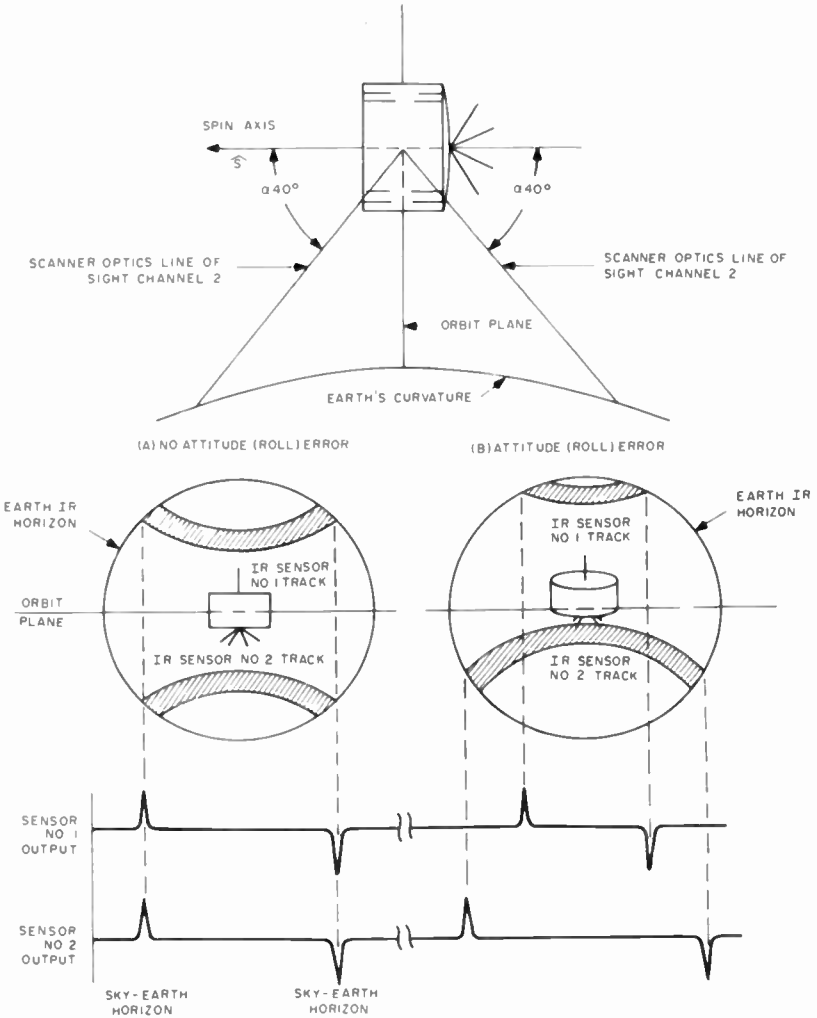

Fig. 6—Attitude sensor geometry and data format.

The second attitude-sensing device is a digital solar aspect indicator. This device provides a direct, digital readout of the satellite sun angle (the angle between the spin axis and a line from the satellite to the sun). In turn, this angle can be used in conjunction with a limited amount of V-head sensor data to determine the satellite's attitude within ±0.1 degree.

Since the satellite is spin-stabilized, it is necessary to maintain a nominal rotational velocity of 8 to 12 rpm about the axis of maximum

moment of inertia. On previous TIROS satellites, the decay in spin rate (due primarily to the effect of eddy currents) was cancelled by firing spin-up rockets whenever the spin rate dropped below 8 rpm. For TIROS IX, these rockets have been included, but only as backup for the new Magnetic Spin Control (MASC) device. This device, whose operation is analogous to that of a d-c motor, can be used bi-directionally (i.e., for spin up or spin down) to maintain the spin period within ±100 milliseconds of a selected value.

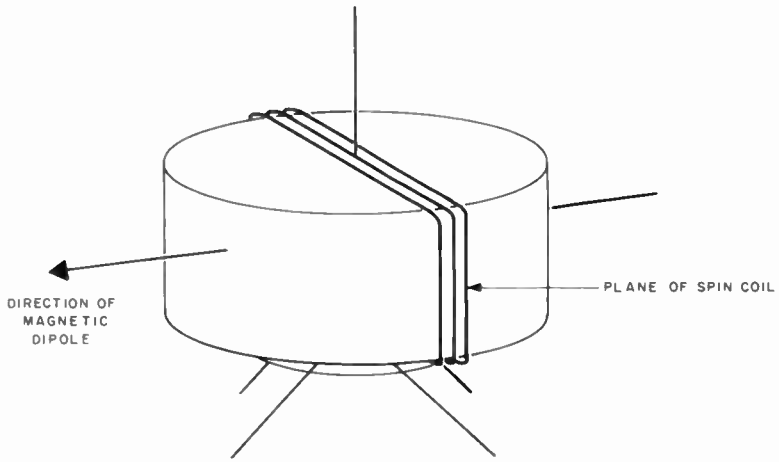

Fig. 7—Orientation of MASC coil.

Like the attitude control devices, the MASC system utilizes a current through a coil to generate electromagnetic fields that interact with the earth's magnetic field and, thereby, produce a torque that can be used to either increase or decrease the satellite spin rate. The MASC coil is mounted perpendicular to the attitude-control coils, and the magnetic dipole moment generated by the MASC device (see Figure 7) is at right angles to the spin axis. In order to obtain a net torque that will effect the desired change in spin rate, the current through the MASC coil is commutated, or reversed, every half revolution of the satellite. The commutation is performed by a dynamics control (Dycon) unit that reverses the direction of the current in the coil each time that an associated orthogonal horizon scanner senses a sky-to-earth transition. Since spin-control torquing is most efficient in the region of the earth's magnetic poles, where the earth's field intensity is greatest, quarter-orbit switching is used to turn the MASC coil "on" in the two quadrants of the earth that contain the poles and "off" while the satellite is in the other two quadrants.

Television-Camera System

The two television-camera subsystems are very similar to those employed on the standard-configuration TIROS satellites. However, because of the wheel orientation, the cameras are mounted to look out through the sides of the satellite rather than through the baseplate. In addition, a more sophisticated triggering system is employed, as noted earlier, and more programming flexibility is provided by the enhanced command and control equipment.

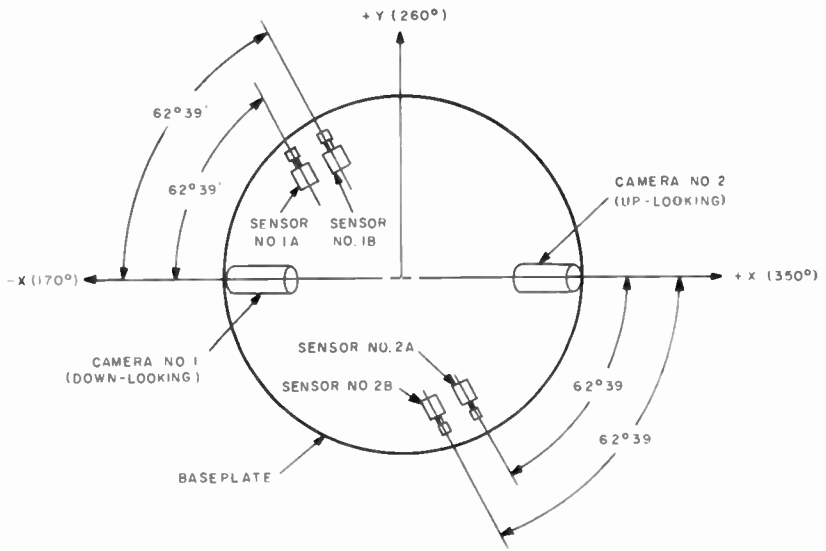

Fig. 8—Relative locations of television cameras and trigger sensors.

Each of the camera subsystems includes a 1/2-inch-vidicon camera equipped with a 104-degree wide-angle lens, camera triggering and control circuits, video-processing circuits, and a complete recording system capable of storing up to 48 television photographs. The two television cameras are mounted diametrically opposite one another and, as shown in Figures 4 and 8, one camera is canted to one side by 26 degrees (with respect to the plane of the baseplate) and the second is canted to the opposite side by 26 degrees. As shown in Figure 9, because of the satellite's operational attitude, this canting results in one camera looking eastward and the other looking westward.

As in the case of TIROS I through VIII, the television cameras can be programmed to take pictures either in the direct or the remote mode of operation. Direct operation is used when the satellite is being interrogated from ground, and the pictures are transmitted directly

to the interrogating station. Conversely, remote operation is used to take pictures when the satellite is not within communications range of a ground station. In this mode of operation, picture-taking operations are controlled by the satellite's two digital command programmers, and the pictures are stored on magnetic tape until such time as the tape recorders are commanded to playback.

During the playback operation, the satellite can be commanded to

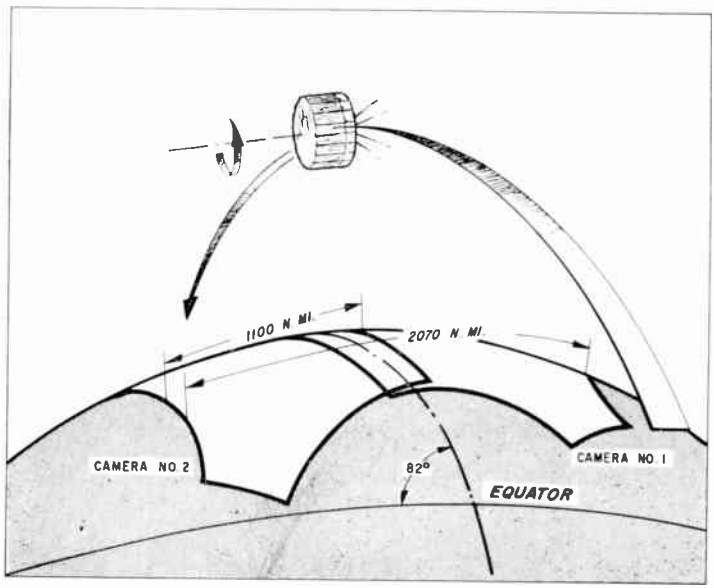

Fig. 9—Planned picture area for cameras 1 and 2.

take another sequence of remote pictures by transmitting a series of digital commands that are stored in the digital command programmers. These commands include such information as the starting time for the prescribed sequence for each camera, the interval (32, 64, or 128 seconds) between pictures, and the number of orbits (up to a maximum of four) on which the sequence is to be repeated. In addition, these commands specify whether both cameras are to be controlled by one command programmer, or individually by their associated command programmers.

While the satellite is under interrogation, it can also be commanded for various auxiliary functions (QOMAC and MASC operations, etc.) and to use either its primary or secondary camera-triggering system. Although both systems make use of the fixed geometric relationship between the horizon scanners and the cameras, the primary (or com-

puting-trigger) system actually computes the spin period and the time at which the camera will view the earth each time that a picture request is received. Because of this, the computing trigger can be used at any spin rate within the 8- to 12-rpm operational limits. The secondary, or spin-trigger, system utilizes the Dycon to synchronize the camera vertical drive pulses to the spin rate of the satellite, and requires that the spin period be maintained at 6.144 seconds ±100 milliseconds. This system will be the primary system for the forthcoming TOS satellites.

Regardless of which triggering system is employed, both cameras can be activated by a single picture request, so that pictures can be taken with both cameras within a one-half rotation of the satellite. This results in two television pictures from a single request—one looking eastward, the other westward—that, considering the orbital velocity and altitude, include essentially the same latitudes. Since the lens angle of the cameras is sufficiently large to include both the horizon and the satellite subpoint in the camera field-of-view, a composite picture can be derived that includes both east and west horizons and that overlaps at the satellite subpoint. As the satellite progresses northward in the orbit, successive picture requests are programmed at intervals chosen to produce overlap in the north-south direction, resulting in a picture mosaic covering the area about the orbital trace from terminator to terminator. Since the earth rotates only 24.89 degrees during the orbital period of the satellite, sufficient overlap is obtained in the east-west plane to provide television-picture coverage of the entire surface of the earth over a 24-hour period.

Telemetry and Power-Supply Systems

The beacon and telemetry subsystem includes two 50-milliwatt beacon transmitters (one operating at 136.23 mc, the other at 136.92 mc) to provide continuous signals to aid in the acquisition and tracking of the satellite by the TIROS ground stations and to provide a carrier for the transmission of telemetry data. Such data include satellite operating parameters, attitude data, camera-triggering data, and command verification data (whenever a command is received by the satellite, it is telemetered back to ground to provide an indication as to whether the correct command has been received). The data are applied to the beacon transmitters through four frequency-modulated subcarrier oscillators that amplitude modulate the beacon carriers. On the ground, the telemetered data are recorded on magnetic tape and displayed on paper chart recorders to enable rapid analysis and evaluation.

Operating power for all TIROS satellite equipment is supplied by

the power-supply subsystem. This subsystem consists of a solar-energy converter containing 9120 n-on-p solar cells, a group of sixty three nickel–cadmium storage batteries, and the necessary voltage-regulation and overload-protection circuits.

The solar-energy converter consists, basically, of an array of silicon solar cells mounted on the top and sides of the satellite structure. During the orbital day, when the solar cells are illuminated by the sun, the output of the array is used as a primary power source for the satellite's electrical system. Any excess power (i.e., power that is not needed by the satellite electronics) is used to charge the storage batteries. In cases where peak-power requirements exceed the power output of the solar cells, the batteries automatically supply the power difference. During orbital night the storage batteries, which have a total capacity of approximately 295 watt-hours, supply all the power required by the satellite.

The storage batteries are electrically connected in three independent groups, each of which is connected to the solar-cell supply through its own current regulator to prevent an excessive rate of charge. The excess power is diverted through a bypass regulator to the main battery output bus. During orbital night, when the solar cells are passive, silicon diodes in each series row of solar cells prevent the storage batteries from discharging into the solar cells.

Performance Summary

The TIROS IX satellite was launched from the Eastern Test Range at Cape Kennedy, Florida, at 0752 GMT on January 22, 1965. The orbital requirements for the mission were a circular, near-polar, sun-synchronous orbit, having an altitude of 400 miles, an inclination of 98.1 degrees and an anomalistic period of 99 minutes. However, because of a malfunction that precluded on-time cutoff of the second-stage engine of the Delta 3C launch vehicle, the satellite was placed in an elliptical orbit having an apogee of 1391 nautical miles, a perigee of 380 nautical miles, an inclination of 96.4 degrees and an anomalistic period of 119 minutes. These parameters, in turn, resulted in a non sun-synchronous orbit with an orbital-plane regression of 0.5 degrees-per-day.

Although the wide variations between the planned and actual orbits prevented optimum performance, the spacecraft has fulfilled its mission objectives, and both the quantity and quality of the data transmitted to date have met or surpassed system requirements. The primary effects of the orbital variations on system performance can be summarized as follows:

(1) The increased orbital period precluded true quarter-orbit phasing of the current through the QOMAC coil and thus necessitated abandonment of the prepared program for effecting the wheel-orientation maneuver. This increased period also precluded full utilization of the orbit-repeat capability that had been included in the camera subsystem.

(2) Approximately 92 percent of the 70,000 pictures returned to date (i.e., January 31, 1966) have been meteorologically useful, despite a slowly changing scene illumination (resulting from the non-sun-synchronous orbit) that has, at times, exceeded the dynamic brightness-response range of the television cameras.

(3) As depicted in Figure 10, the angular difference, β, between the location of a television camera and its associated horizon sensor was selected for system operation in the planned, 400-nautical mile orbit. Because of this fixed angular relationship, the differences between the planned and actual altitudes have resulted in the introduction of a pitch error (minus 1.3 degrees at perigee to plus 18.7 degrees at apogee) into the camera pointing system.

(4) Because of the non-sun-synchronous orbit, special attitude maneuvers were required to maintain satisfactory power and thermal profiles. One such maneuver is described later.

(5) The average radiation intensity in the orbit actually achieved for TIROS IX is 50 to 75 times greater than that which would have been experienced in the planned, 400-nautical mile, circular orbit. Since the spacecraft subsystems were not designed to operate in such a radiation environment, it is anticipated that, in time, several of the subsystems will experience radiation damage.

As noted previously, TIROS IX was launched by means of a three-stage, Delta 3C launch vehicle. Shortly before separation from the second stage of the vehicle, the combined third-stage and spacecraft was spun-up to 128.9 rpm to provide greater vehicle stability. Upon separation of the satellite from the third stage of the launch vehicle, the separation switches actuated firing squibs that activated the nutation dampers. These devices quickly damped the initial wobble of the satellite and, since that time, have remained active, limiting the nutation cone angle to 0.5 degree.

Approximately five minutes after separation, the despin timer fired a pair of squibs and thereby released the despin weights that were mounted on the periphery of the hat assembly and attached to steel cables that wrap around the hat. With the cables released, centrifugal force caused the weight/cable assemblies to unwrap from the satellite and be cast off into space. The momentary increase in the satellite's

moment-of-inertia due to the unwrapping of the weight/cable assemblies resulted in successful spin-down, reducing the spin rate from the orbit injection rate of 128.9 rpm to an operational rate of 9.95 rpm in approximately 0.5 second.

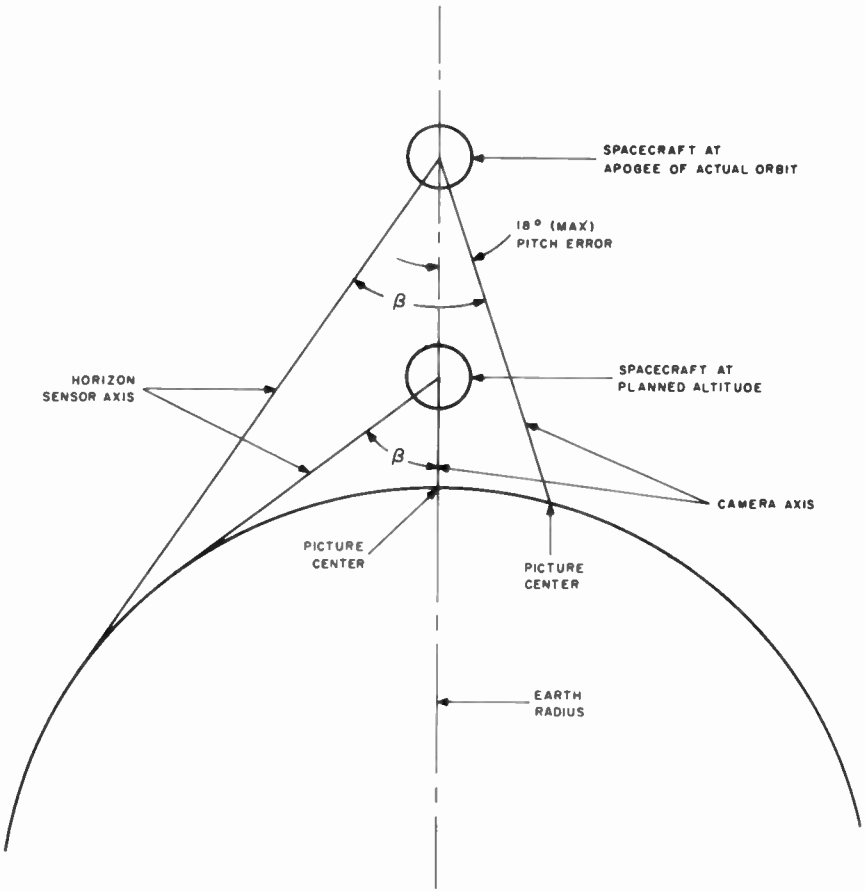

Fig. 10—Effect of altitude on camera pointing.

Because of the manner in which they are mounted on the launch vehicle, each TIROS satellite is injected into orbit with its spin axis in the orbital plane. In order to orient TIROS IX to the wheel attitude, the QOMAC device was used in its high-torque mode of operation to precess the spin axis from its injection attitude to a position normal to the orbital plane. Although this orientation maneuver was started on schedule, the planned program had to be altered to take into account

the variation in the strength of the earth's magnetic field over the range of altitudes (i.e., 380 to 1391 nautical miles) and the 19-minute increase in orbital period. Because the attitude control system had been optimized for the planned, 400-nautical mile, circular orbit, the effect of the elliptical orbit has been to reduce the torquing efficiency to approximately 75 percent of that predicted; thus, additional QOMAC programs had to be written and employed to effect timely completion of the wheel-orientation maneuver and ensure that the satellite's in-

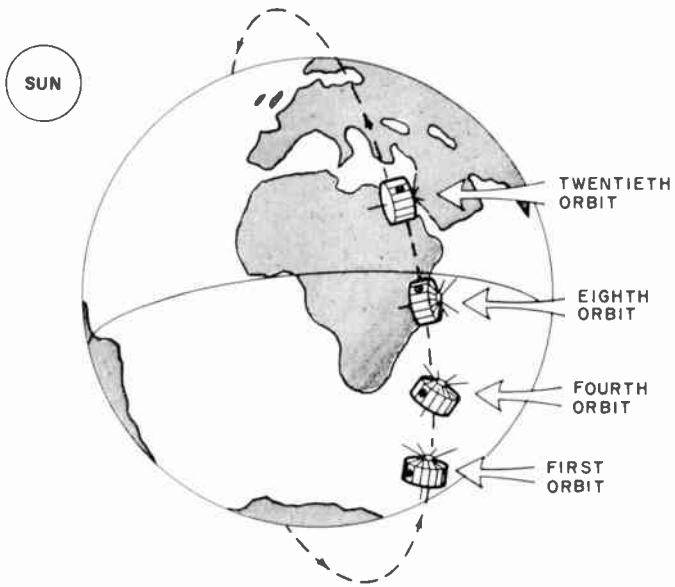

Fig. 11—Wheel-orientation maneuver of TIROS IX.

ternal temperature would remain within design limits. Despite the program changes necessitated by the orbital variations, the maneuver was performed in 20 orbits and, at the conclusion of the maneuver, the spin axis was within one degree of the orbit normal. (For the planned orbit, this maneuver was scheduled for completion in 14 orbits.) The success of the orientation maneuver and the subsequent maintenance of the desired spin-axis attitude demonstrates the capability of the satellite's attitude-sensing, dynamics control, and command and control equipment. Figure 11 depicts system performance in the actual wheel orientation maneuver.

After the maneuver was completed, a series of tests and checks were performed to verify the operational readiness of the satellite's

many subsystems and the capability for operating these subsystems in various cross-coupled modes (the use of one digital command programmer to control both cameras, etc.). By the third day after launch, all spacecraft subsystems and operating modes had been checked out with satisfactory results, and the spacecraft was deemed ready for use.

The first television pictures returned by TIROS IX were taken while the satellite was at apogee. These pictures demonstrated that

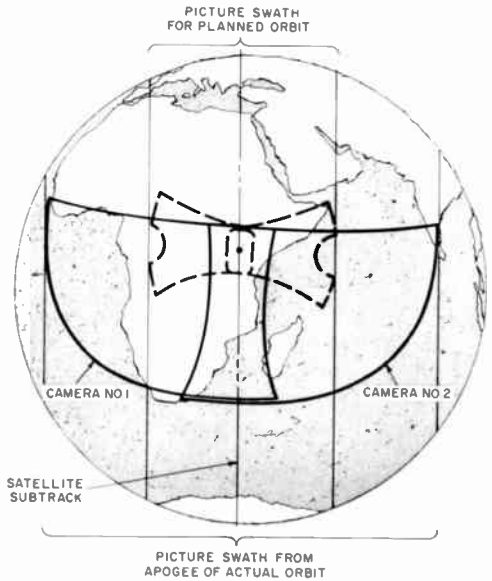

Fig. 12—Planned versus actual TIROS IX photocoverage.

significant weather information was readily discernible, despite the reduced resolution resulting from the high altitude (the resolution at apogee is approximately 8 nautical miles per television line as compared to 2 nautical miles per line at the planned altitude). Further, the pictures returned when routine programming was instituted demonstrated that the satellite was capable of providing daily contiguous photocoverage of the earth. Because of the high altitudes, the overlap in photocoverage from one orbit to the next was much greater than had been anticipated prior to launch. A comparison of the planned and actual photocoverage is shown in Figure 12.

During the initial two months of operation, the satellite was programmed to provide photocoverage on nearly every orbit and returned

an average of 450 pictures every day. Both television camera subsystems were used during this period and each provided good to excellent quality pictures of cloud cover and of ice and snow conditions in various parts of the world. The capability of taking essentially simultaneous pictures with both cameras was utilized extensively during these initial months of operation and composite pictures such as those shown in Figures 13 and 14 were obtained. In turn, these photographs were used to form composite views of the earth's entire cloud cover, such as that shown in Figure 15.

Television camera subsystem No. 2 continues to provide pictures of good-to-excellent quality after 13 months in orbit; however, the pictures returned by television camera No. 1 began to show signs of performance degradation after approximately 600 orbits. By early April 1965, after the satellite had completed 10 weeks of orbital operation, the amount of degradation had increased to the point where the low contrast in the pictures from camera No. 1 prevented them from being meterologically useful, and routine programming of that camera was suspended.

It is suspected that the loss of contrast resulted from the effects of radiation on the camera's beam-current regulator or degradation of the cathode of the vidicon, or a combination of both. Since the spacecraft was not designed to operate in the environment to which it was subjected, as a result of the deviation between the planned and actual orbits, it was anticipated that some subsystems would experience radiation damage. It is probable that, in time, the camera-triggering circuits, which include a critically adjusted amplifier, will also be affected by radiation exposure and that camera triggering will become erratic. However, such an anomaly has not yet been detected, even though an estimated radiation dosage of 10^5 rads has already been experienced by the satellite.

Since the cessation of picture-taking with camera subsystem No. 1, the photocoverage has not been contiguous in the vicinity of the equator. However, essentially contiguous coverage is being maintained by the concurrent use of TIROS IX with TIROS VII, VIII, and X. (TIROS X was launched and orbited on July 1, 1965. This satellite and TIROS VII and VIII were still in operation as of January 31, 1966.)

The two camera-triggering systems, which operate the camera shutter, have been used interchangeably since the launch and both have performed satisfactorily. Less than one percent of the 70,000 pictures taken were lost due to improper triggering. The remainder of the command and control equipment, including the new digital

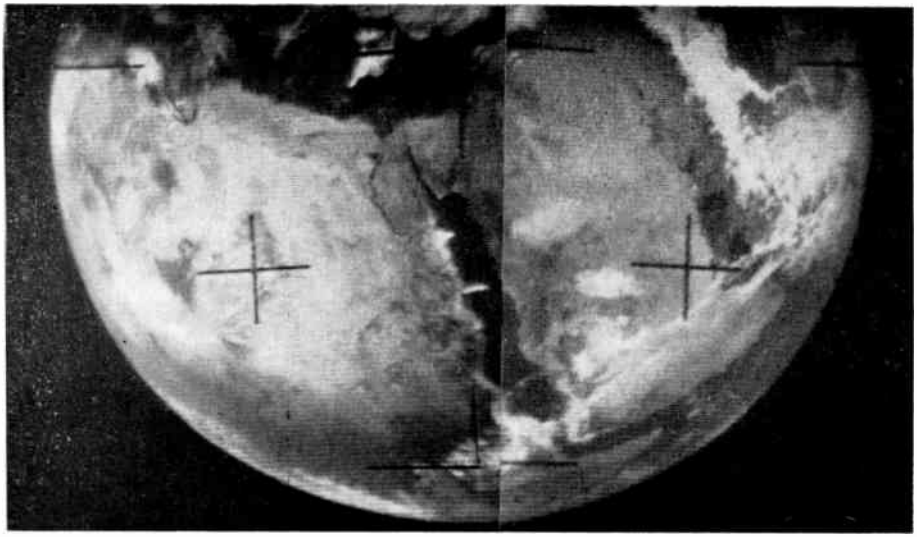

Orbit 135 (Apogee): Mediterranean Sea, North Africa, Asia Minor, and Red Sea

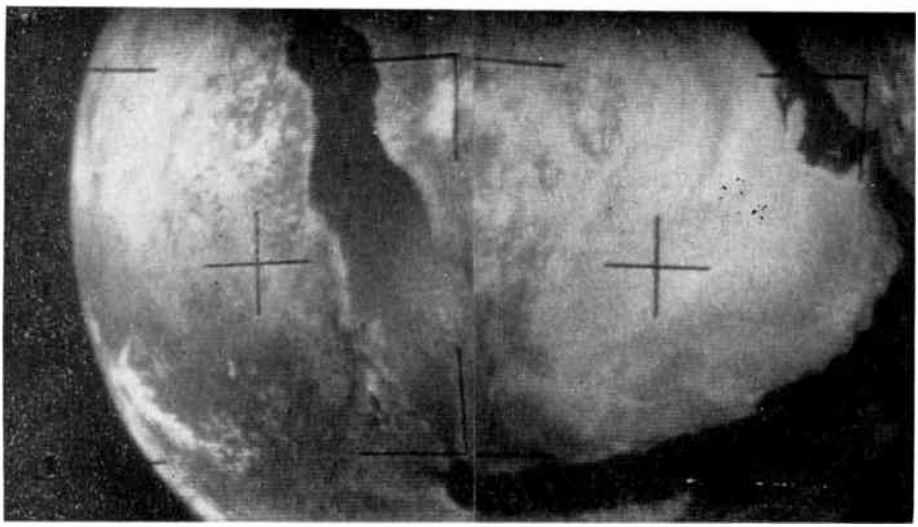

Orbit 557 (Perigee): Red Sea and Saudi Arabia at Higher Resolution Resulting from Lower Altitude

Fig. 13—Examples of composite television pictures from TIROS IX camera 1 pictures on left, camera 2 on right.

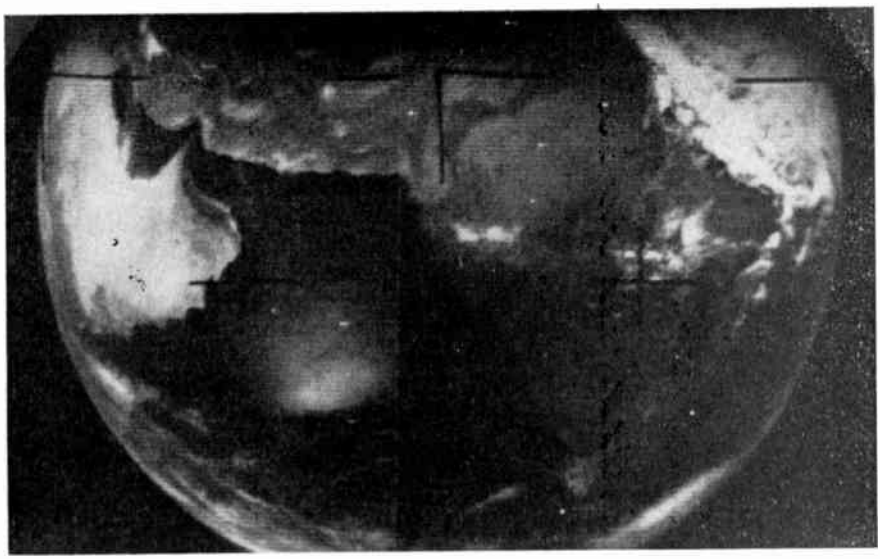

Orbit 340: Saudi Arabia, Iraq, Pakistan, India, Snow-Covered Himalayas, and Sun Glint off Arabian Sea

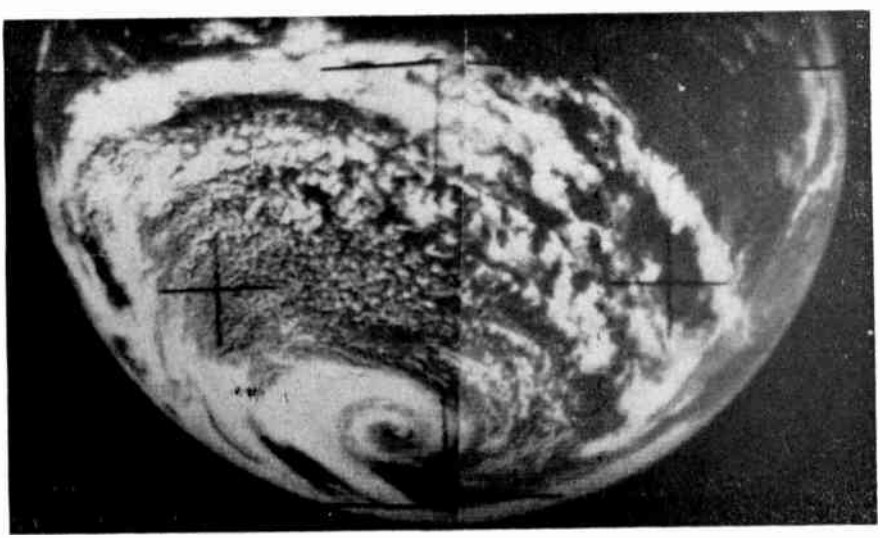

Orbit 436: Large Vortex and Frontal System in South Pacific Ocean

Fig. 13 (cont'd)—Examples of composite television pictures from TIROS IX: camera No. 1 pictures on left, camera No. 2 on right.

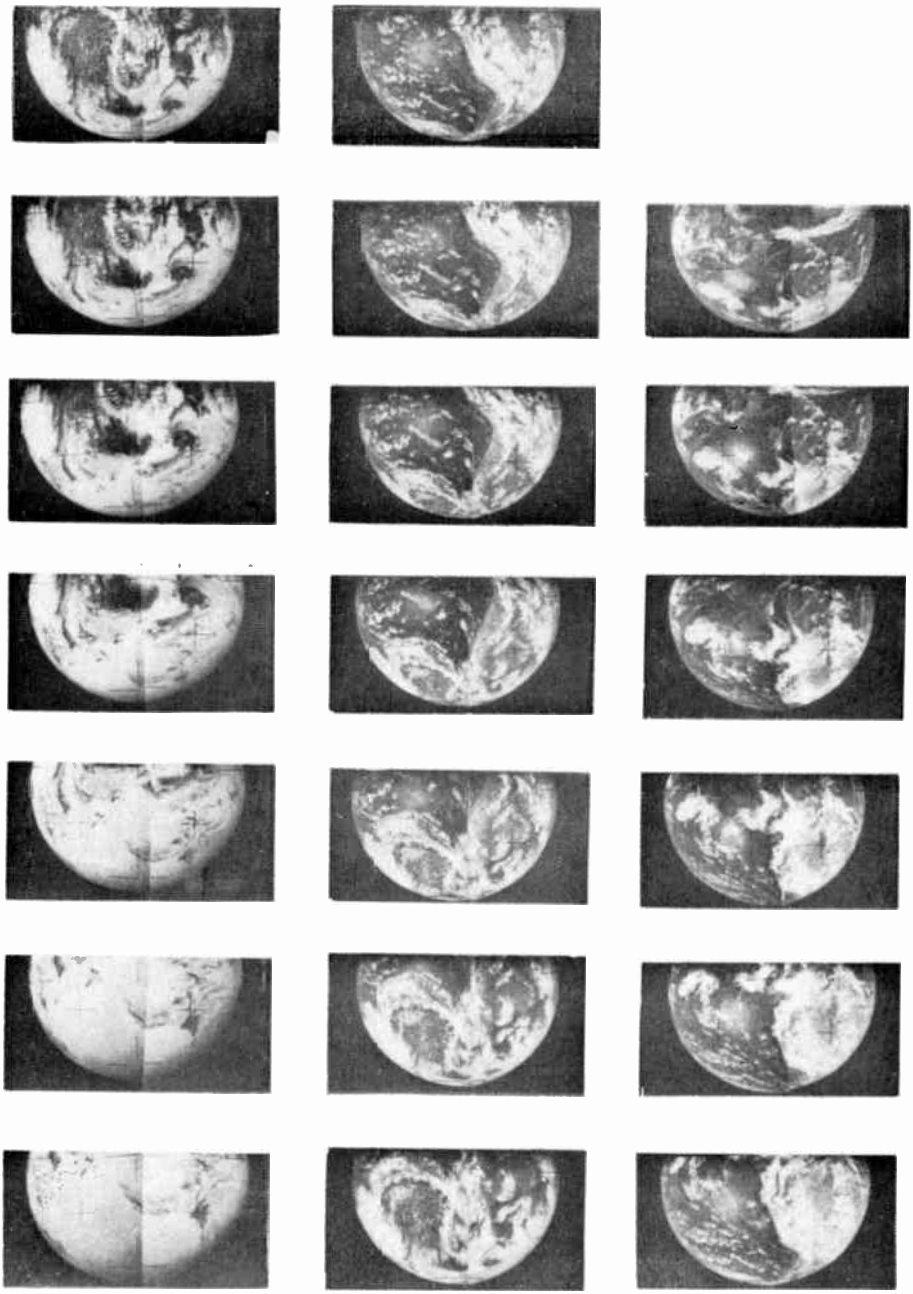

Fig. 14—Sequence of pictures taken by TIROS IX on orbit 115. Sequence starts at lower left with pictures of Antarctic ice cap and ends at upper right with pictures of Central America.

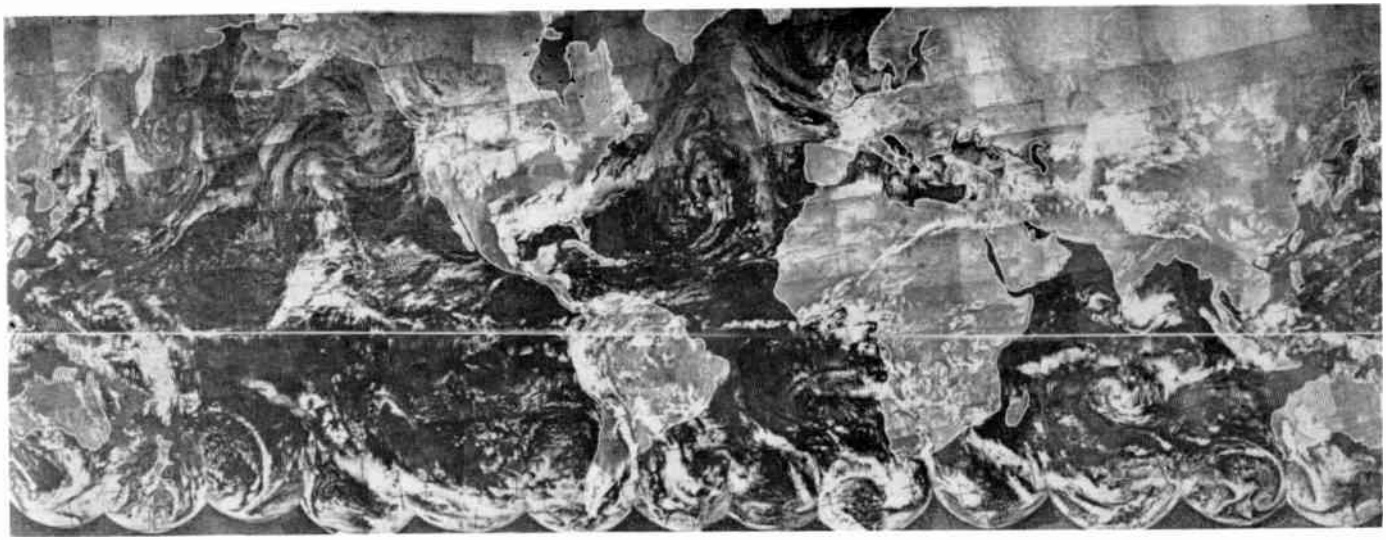

Fig. 15—First complete view of the world's weather. This photomosaic is composed of 450 photographs taken by TIROS IX during its 12 orbits on February 13, 1965. (Courtesy of U. S. Weather Bureau)

command programmers, has also performed well. All spacecraft commands have been correctly decoded and acted upon, the proper command-confirm data has been transmitted to the ground stations, and the timing information provided by the time-base generators has been very satisfactory. In addition, the cross-coupling circuits have been checked out and used with very good results.

That the attitude-sensing and dynamics control equipment has provided satisfactory operation is exemplified by the quality of the attitude data and by the successful performance of the attitude maneuvers necessitated by the 1/2 degree-per-day regression of the orbital plane, depicted in Figure 16. These special attitude maneuvers can be summarized as follows.

After the wheel orientation maneuver was completed, the MBC device was set to provide the desired average spin-axis precession and the low-torque QOMAC sequences were programmed once every 4 or 5 days to cause the spin axis to track the orbit normal until February 21, 1965 (Orbit 387). From then until March 27 (Orbit 768), these devices were used to move the spin axis from the orbit normal position and control the axis such that the sun angle was maintained at approximately 70 degrees in order to ensure favorable thermal and power profiles. On Orbit 768, QOMAC was used to reduce the sun angle to 65 degrees and, thus, to provide a greater thermal input to the satellite to compensate for the relatively long periods of orbital nighttime resulting from the regression of the orbital plane.

The attitude control devices were used to maintain this value of sun angle until April 7, when the orbital plane had regressed to a position in which the sun-earth vector was nearly coincident with the orbital plane. On this orbit a major attitude maneuver was initiated to maintain a nearly constant sun angle by essentially rotating the spin axis 180 degrees above a spatial cone. This maneuver was accomplished in 30 orbits, using 34 QOMAC cycles and, at the conclusion, camera No. 2, which had faced the western horizon, faced the eastern horizon. After the maneuver was completed, the attitude control devices were again used to maintain a 65-degree sun angle while, at the same time, allowing the spin axis to move closer and closer to the orbit normal.

On June 20, the satellite was finally returned to the true wheel orientation; i.e., the spin axis became co-linear with the negative orbit normal. This orientation was maintained during the next several months. When the sun angle again decreased below the minimum operational value, the satellite was maneuvered by a special attitude program to move the spin axis from the orbit normal and gain a more favorable sun angle. The over-all performance of the magnetic attitude

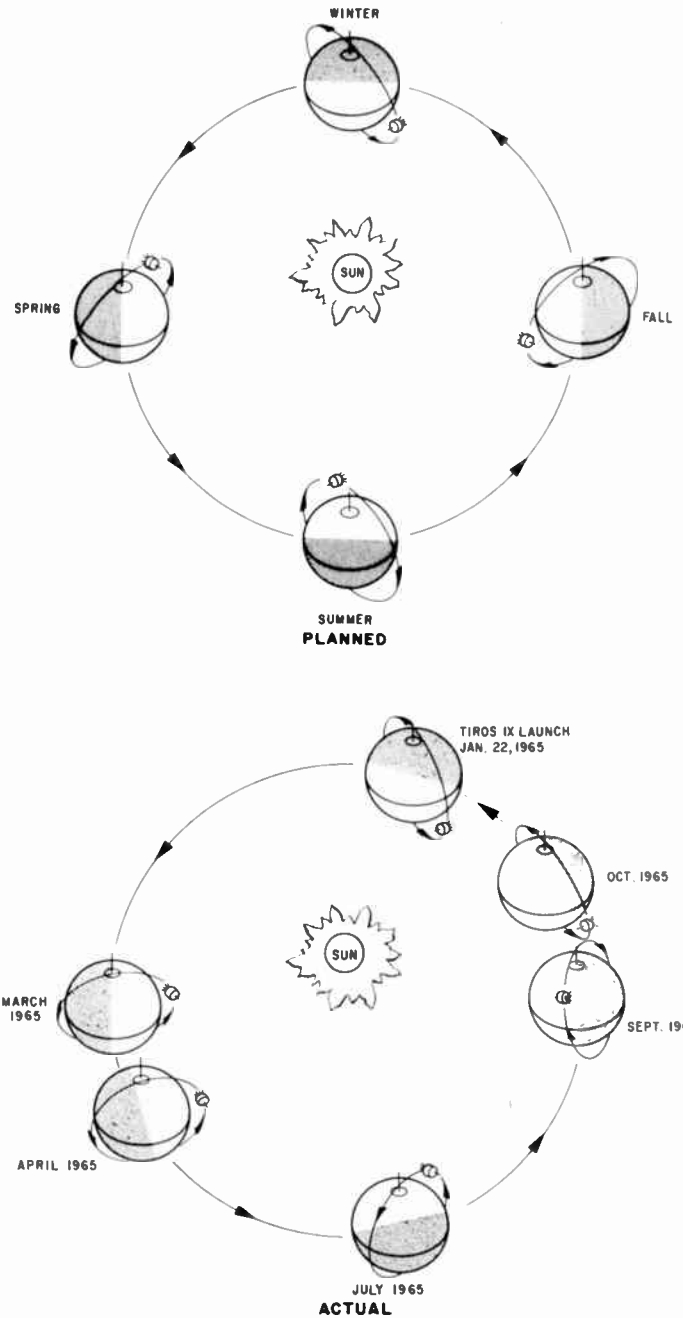

Fig. 16—Comparison of spacecraft orientation for planned sun-synchronous orbit and orientation in actual orbit (not sun-synchronous).

control device, both in the performance of these maneuvers and in normal station-keeping operations, has been excellent.

The operational capability of the MASC device has also been demonstrated by the TIROS IX satellite. Although the satellite's subsystems will operate over a relatively wide range of spin rates (8 to 12 rpm), one mode of camera triggering—a forerunner of that planned for the TOS system—requires the spin period to be maintained at 6.144 seconds ±100 milliseconds. Whenever this mode has been selected, the MASC system has allowed the required spin period to be maintained

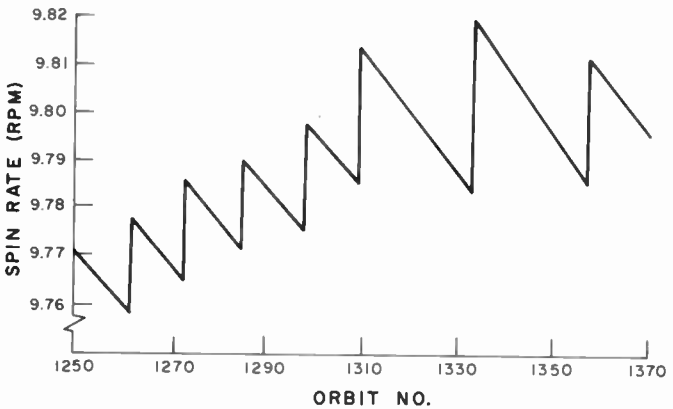

Fig. 17—Data plot of typical history of MASC utilization.

within the specified limits without difficulty. Further, several experiments have been conducted that have demonstrated the capability of the MASC system to maintain the spin period within ±15 milliseconds of the desired period. A data plot showing a typical history of MASC utilization is given in Figure 17. As can be seen from this plot, the spin-rate decay of TIROS IX is approximately 0.01 rpm per orbital day (12 orbits). During the first five days of the period encompassed by this plot, a short MASC sequence was programmed each day to overcome the spin rate decay and gradually raise the spin rate from 9.76 rpm to 9.80 rpm. Then, for the next five-day period, a slightly longer MASC sequence was programmed every other day to maintain the spin rate within ±0.02 rpm of the selected rate of 9.8 rpm. Such control will easily meet the requirements of the TOS system.

The over-all performance of the power-supply system has been very good. The rechargeable storage batteries and the voltage regulators have met all design requirements. The solar cells, which are directly

exposed to the radiation fields encountered in the unplanned orbit, have experienced approximately a 15% loss in power output, but ample reserve power is still being provided to operate the satellite electronics and maintain the nickel–cadmium storage batteries in a suitably charged condition.

The passive thermal-control system, which depends upon conduction and radiation between the various subsystems and the satellite's exterior shell, and the thermal radiation exchange between the satellite's outer structure and the space environment, has also performed well. Satisfactory temperatures have been maintained despite the prolonged initial orientation maneuver and the variations in sun angle resulting from the regression of the orbital plane.

The beacon and telemetry equipment, including the solid-state commutators, has provided accurate telemetry and attitude data. Additionally, adequate communication has been maintained in spite of the fact that the slant range to the satellite is much greater than that which had been considered in the design of the telemetry transmitters.

Meteorological Results

The estimated locations of many surface weather systems have been revised because of TIROS IX data. In addition, the data obtained from TIROS IX was used, in conjunction with that from TIROS VII and VIII, to provide weather observations in support of the Ranger 9 launch, and to provide world-wide weather data in the support of the Gemini GT-3 and GT-4 prelaunch, launch, orbital, and recovery operations.

As of January 31, 1966, the satellite had transmitted 70,000 television pictures, approximately 92 percent of which were considered meteorologically usable. Because of the stable and precise attitude control provided by the subsystems, picture orientation and rectification is easily accomplished, and storm systems can be readily located and tracked. In the first six months of operation, 5055 nephanalyses and 830 storm bulletins were prepared and issued based on data transmitted from TIROS IX. Table I shows the number of storm advisories issued on the basis of TIROS IX data during the first five months of orbital operations.

Summary of Performance of Tiros Satellites

As of January 31, 1966, ten TIROS satellites had been orbited and operated successfully, providing an aggregate total of 3,890 days of

Table III—TIROS Configuration Summary

Spacecraft	TIROS I	TIROS II	TIROS III	TIROS IV	TIROS V	TIROS VI	TIROS VII	TIROS VIII	TIROS IX	TIROS X	TIROS* XI
Weight (pounds)	263	278	285	286	287	281	299	260	300	290	290
Camera 1	NA	NA	WA	WA	WA	WA	WA	WA	WA[1]	WA	WA[1]
Camera 2	WA	WA	WA	MA	MA	MA	WA	APT	WA[1]	WA	WA[1]
Beacon Frequency (MC)	108	108	108	136	136	136	136	136	136	136	136
Magnetic Attitude Control		X	X	X	X	X	X	X	MBC QOMAC MASC	MBC QOMAC	MBC QOMAC MASC
Timers for Beacon Turn-Off						X	X	X			
Selective Address Unit							X	X	X	X	X
Additional Experiments											
Scanning IR	X	X	X				X				
Wide-Field IR	X	X	X								
Omni-Directional IR		X	X				X				
Electron Probe							X				

Camera Code (Picture Area—400-nautical miles altitude):
- NA = Narrow Angle (12.5° lens); 5,000 square miles
- MA = Medium Angle (78° lens); 250,000 square miles
- WA = Wide Angle (104° lens); 500,000 square miles
- WA[1] = Wide Angle (104° lens); Camera Tilted 26.5°; 1,000,000 square miles
- APT = Automatic Picture Transmission; 1,000,000 square miles

Magnetic Attitude Control Code:
- MBC = Magnetic Bias Control
- QOMAC = Quarter Orbit Magnetic Attitude Control
- MASC = Magnetic Spin Control

* Designated ESSA-1.

TIROS X, a modified standard-configuration satellite was launched from Cape Kennedy, Florida, at 11:07 p.m. EST, July 1, 1965, and injected into an essentially circular, near-polar, sun-synchronous orbit. As of February 15, 1966, it had transmitted more than 70,000 pictures to the TIROS ground stations.

It was originally planned to use TIROS X to provide weather observations during the 1964 hurricane season; however, the extreme longevity of TIROS VII and VIII resulted in a decision to postpone the launch. In the interim, TIROS IX was launched to demonstrate performance capabilities of the wheel mode of operation in order that

Table IV—Tropical Storms Observed by TIROS Satellites July 1961 through May 1965

Year	Atlantic Ocean	Eastern Pacific Ocean	Western Pacific Ocean	Indian Ocean	Total
1961	7	4	9	—	20
1962	3	3	17	—	23
1963	8	4	14	3	29
1964	8	5	31	4	48
1965	—	—	6	2	8
Total	26	16	77	9	128

the optimum system design for the planned TIROS Operational System (TOS) could be determined, and to provide daily global photocoverage. Because of the regression of the TIROS IX orbital plane, however, the satellite's cameras would be viewing twilight zones during the peak of the hurricane season in August and September 1965. Because of this, and because TIROS VII and VIII had been in operation for a considerable period of time, the U. S. Weather Bureau and NASA directed that TIROS X be launched to ensure the full and necessary coverage for the 1965 hurricane season. Table V summarizes the orbital elements of all TIROS satellites in orbit.

A number of subsystems that had been proven by TIROS IX were incorporated in TIROS X to enhance its operational capabilities. The added subsystems, including the QOMAC system, the digital solar-aspect sensor, and the V-head attitude sensor, will enable the maintenance of long-term photocoverage in the Northern Hemisphere, as well

Table V—TIROS Orbital Elements

Spacecraft	TIROS I	TIROS II	TIROS III	TIROS IV	TIROS V	TIROS VI	TIROS VII	TIROS VIII	TIROS IX	TIROS X	TIROS* XI
Designation	Beta 2	Pi 1	Rho 1	Beta 1	A-Alpha-1	A-Psi-1	24-A-1	54-A-1	65-4-A	65-51-A	66
Launch Date	4-1-60	11-23-60	7-12-61	2-8-62	6-19-62	9-18-62	6-19-63	12-21-63	1-22-65	7-1-65	2-3-66
Orbital Period (min)	99.19	98.27	100.42	100.40	100.47	98.73	97.42	99.35	119.1	100.78	100.22
Inclination (degrees)	48.36	48.53	47.53	48.30	58.10	58.32	58.23	58.50	96.4	98.64	97.89
Apogee											
miles	465.9	453.0	506.4	524.8	603.9	442.1	403.5	468	1602	521	522.6
km	749.6	728.9	814.8	844.4	971.7	711.3	649.2	754.8	2579	839.2	841.1
Perigee											
miles	428.7	387.0	461.0	441.2	366.4	425.3	386.1	435	435.0	467	432.9
km	689.8	622.7	741.7	709.9	589.5	684.3	621.2	701.6	701.0	752.1	696.7
Eccentricity	0.0042	0.0074	0.0050	0.0094	0.0267	0.0019	0.0020	0.0038	0.117	0.0061	0.0101

* Designated ESSA-1.

as a 60-percent photocoverage of the earth, twice that provided by TIROS I through VIII.

On February 3, 1966, a second TIROS wheel satellite, TIROS XI (designated ESSA-1) was launched from Cape Kennedy into a 400-nautical mile, near-polar, sun-synchronous orbit to provide daily global photocoverage. This satellite is the first TIROS satellite to be used on a fully operational basis and, as of March 20, had transmitted more than 20,000 television pictures.

TIROS OPERATIONAL SYSTEM (TOS)

To be considered operational, a meteorological satellite system must provide contiguous global photocoverage on a daily basis without interruption. The TIROS Operational Satellite System (TOS) will provide such regular and continuous photocoverage and, in addition, will provide meteorologists with infrared observations of the earth and its environs.

Operational satellites in this system are scheduled to be placed in operation in the first quarter of 1966,* beginning with the launching of wheel-type TIROS satellites into near-polar orbits 750 nautical miles above the earth. The orbits will be sun-synchronous, so that the cameras will photograph a given latitude at the same sun time on every orbit.

The complete system will include satellites of two configurations: one configuration, the direct local readout system, will utilize two fully redundant Automatic-Picture-Transmission (APT) camera systems for direct local readout to a world-wide network of APT ground stations equipped with facsimile printers; the second will utilize two fully redundant Advanced Vidicon Camera Systems (AVCS) that are capable of remote picture storage and readout. When the AVCS configuration is used, two primary Command and Data Acquisition (CDA) stations will be used to gather daily global observations of the earth's cloud cover for world-wide weather forecasts. This operational concept for the basic TOS system is depicted in Figure 19. When the TOS system is in operation, two satellites—one with APT cameras and one with AVCS cameras—will be available at all times to provide both local and world-wide cloud-cover pictures on a daily basis.

---

* *Note added in proof: The first TOS satellite, ESSA-2, was successfully launched and orbited on February 28, 1966. This satellite, which is equipped with two APT camera systems, is currently being used in conjunction with the ESSA-1 satellite to provide both local and direct world-wide photocoverage of the earth's atmosphere. As of March 20, ESSA-2 had transmitted more than 2,500 direct-readout television pictures to local APT receiving stations.*

The CDA station equipment is shown in Figure 20; the APT station equipment is shown in Figure 21. The antennas employed by the two types of stations are not shown in the figures. (The CDA stations employ 85-foot parabolic-type antennas, while the APT stations employ helix-type antennas approximately 15 feet long.)

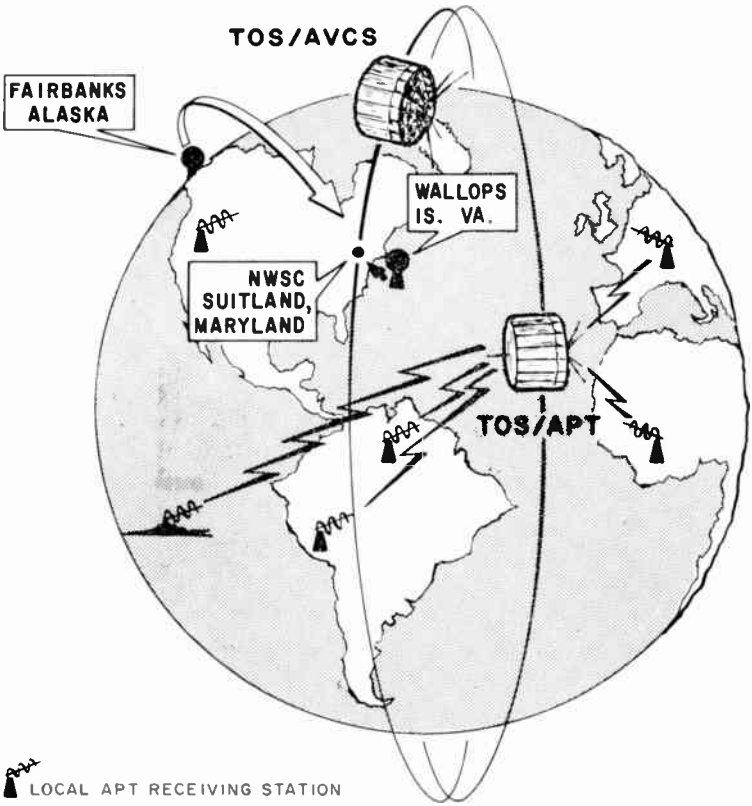

Fig. 19—The basic TOS system.

Both of the camera systems to be used on TOS have been tested successfully on previous spacecraft—the APT system on TIROS VIII and on the Nimbus I spacecraft, and the AVCS system on the Nimbus I spacecraft. The camera for each system utilizes a 1-inch vidicon with an 800-line resolution and a wide-angle lens assembly. Thus, at the 750-nautical mile altitude, each television picture will cover an area of 1736 × 1736 nautical miles, as shown in Figure 22. Regardless of which of the two camera systems is employed, one camera will be capable of providing contiguous photocoverage of the earth; the only

Fig. 20—Command and Data Acquisition (CDA) station equipment.

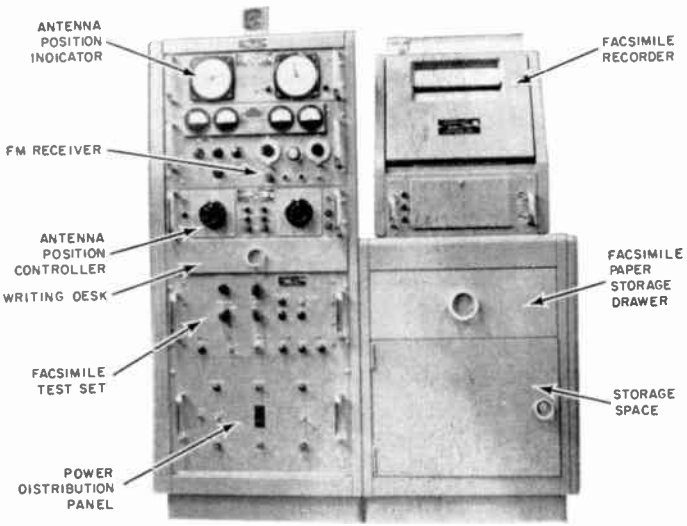

Fig. 21—APT station equipment.

difference being that the AVCS cameras will be programmed to take 12 pictures per orbit and, therefore, will provide a greater in-track overlap than the APT cameras, which will take only 8 pictures per orbit. Since only one camera is required to provide contiguous coverage, the second camera aboard each spacecraft is a redundant system that will ensure a longer operating life for the spacecraft. Figure 23 shows the in-track overlap for the TOS/APT system.

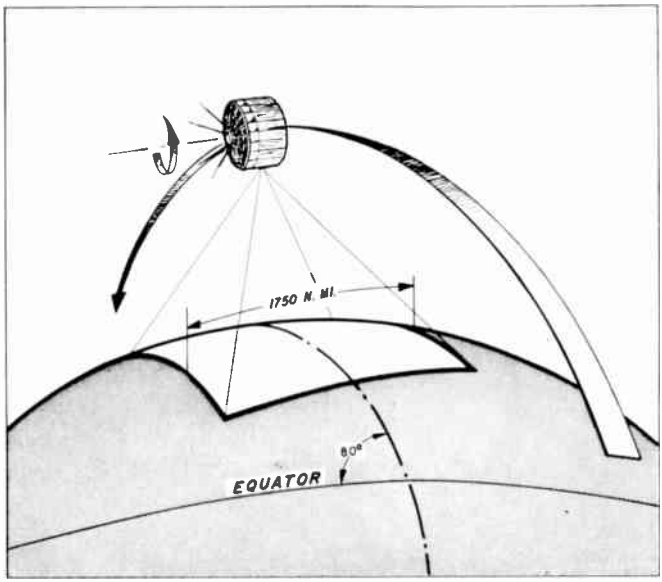

Fig. 22—TOS satellite planned picture area.

The vidicons employed in APT cameras utilize special, long-persistency photosensitive material for image storage. This material allows the pictures taken by the APT cameras to be stored, without degradation, for the 200-second period required for line-by-line transmission of data to the facsimile type receiving stations. As noted previously, satellites equipped with APT cameras will take 8 pictures on each orbit, or one picture every 352 seconds while the satellite is over illuminated areas of the earth.

The AVCS cameras operate in essentially the same manner as the present TIROS cameras. That is, pictures taken by these cameras are normally stored on magnetic tape for rapid readout to centrally located command and data acquisition stations. Satellites equipped with these cameras will take 12 pictures on each orbit, or one picture every 260

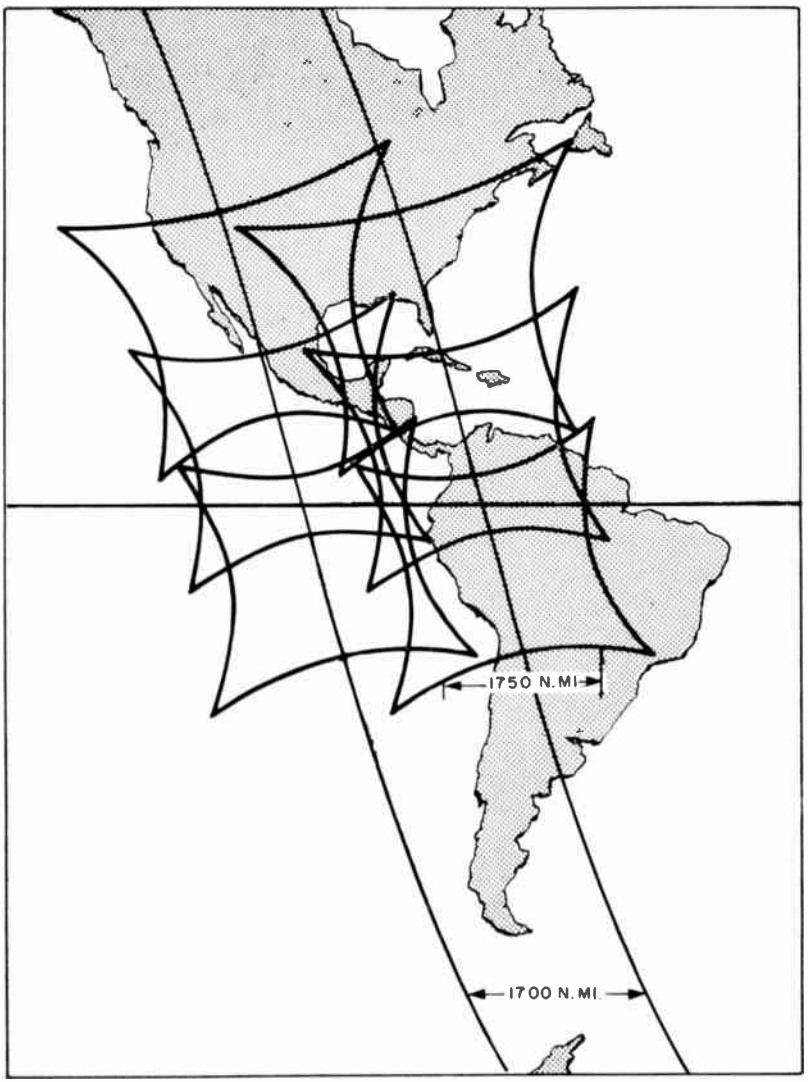

Fig. 23—In-track overlap of TOS/APT television photographs.

seconds while they orbit over the sunlit portions of the earth. Thus, in a single orbital day, one TV camera will return 144 pictures, providing contiguous coverage of the entire earth.

The operation of both TOS/APT and TOS/AVCS satellites will be controlled by commands transmitted from the Command and Data Acquisition (CDA) stations at Gilmore Creek, Alaska, and at Wallops Island, Virginia. However, while the TOS/APT satellites will transmit

data directly to local APT stations, meteorological data from the TOS/AVCS satellites will be transmitted only to the CDA stations, where it will be recorded on magnetic tape. Shortly after its receipt, the data will be played back from the magnetic tape and transmitted to the Weather Bureau's Data Processing and Analysis Facility at the National Weather Satellite Center in Suitland, Maryland. Information received from the satellites of the TOS system will be integrated with that obtained from conventional observations and used in daily Weather Bureau forecasts and analyses. In turn, these analyses will be relayed to field stations in the United States and to weather bureaus in countries throughout the world.

Current planning calls for TOS satellites to be launched from Cape Kennedy, Florida, using improved, three-stage, thrust-augmented Delta rockets. To attain the 750-nautical mile altitude required for the TOS System, the thrust of the launch vehicle will be supplemented by strapping three solid-propellant rockets to the Thor stage of the vehicle and by using an improved Delta rocket.

Future TIROS/TOS Systems

Future developments on TIROS/TOS will provide a single spacecraft configuration capable of providing both local readout to small receiving stations located throughout the world, and global readout, on a daily basis, to a central station at the National Weather Satellite Center. A special version of the APT camera employed on TIROS VIII and Nimbus I and a modified OGO (Orbiting Geophysical Observatory) recorder are currently undergoing development at RCA for NASA and are expected to comprise the primary system for this mission in the second TOS series.

A study is currently being made by RCA for NASA to develop a system design for utilizing a modified, Nimbus High Resolution Infrared (HRIR) sensing device on a TIROS wheel-configuration satellite. The spacecraft design will be such that nighttime cloud-cover observations can be transmitted directly to local receiving stations and recorded for subsequent global-coverage readout to central receiving stations.

A study has also been underway at RCA, for NASA, to determine the feasibility of placing a TIROS satellite into a highly elliptical orbit so as to provide continuous, 2-hour observation of a local area of interest from an altitude of 22,000 statute miles (apogee). Two AVCS cameras, one equipped with a wide-angle lens and the second with a narrow-angle lens, are being considered for this application.

CAMERA TUBES FOR RECORDING STRATOSCOPE II TELESCOPE IMAGES

By

A. D. Cope and E. Luedicke

RCA Astro-Electronics Division
David Sarnoff Research Center
Princeton, N. J.

Summary—Camera tubes for use in a television camera that will be used to record images obtained with the 36-inch Stratoscope telescope operating at 80,000 feet above sea level must be capable of integrating the input for exposures lasting more than 30 minutes. The fundamental limitations and special problems encountered where photometric fidelity of a single readout scan is required are discussed for both the image-orthicon and image-isocon tubes. Advantages of the image isocon are discussed. Results of laboratory tests with point-image patterns along with preliminary results in recording stellar spectra are included.

Introduction

TELEVISION, the name adopted many years ago to refer to viewing from a distance, has been presented with a new area of application in astrophysical scientific exploration. Instrument satellites that perform meteorological and geophysical studies of the earth and lunar and planetary mapping are a reality. As an active guidance system on a balloon-borne astronomical telescope (Stratoscope), television has provided the ground-based astronomer with the means for controlling his observation program with almost the same convenience that is enjoyed in the observatory.

The potential capabilities of photoelectric imaging systems outside the broadcast field are substantial. It is evident, however, that before this potential can be fully realized several areas of performance must be more completely controlled, new operating criteria must be established, and extensions in sensor capability must be achieved.

This paper summarizes earlier reports[1,2] of a camera-tube study extending over several years that seeks to develop and assess the performance of a unique television camera, intended for recording the

[1] A. D. Cope, E. Luedicke, and L. E. Flory, "Astronomical Image-Integration System Using a Television Camera Tube," *Appl. Optics*, Vol. 3, p. 677, June 1964.

[2] L. E. Flory, W. S. Pike, J. M. Morgan, and L. A. Boyer, "A Programmable Integrating Television Camera for Astronomical Applications," *Jour. S.M.P.T.E.*, Vol. 74, p. 760, 1965.

images obtained with the Stratoscope telescope. Laboratory evaluation indicates that a significant sensitivity improvement over photographic recording should be achieved. The results of recent work and the directions being taken for continuing development are also included.

Television camera systems used to record scientific information useful in the fields of astronomy, meteorology, and geodesy, operate in a different mode from that of broadcast television. A permanent copy recording is made of each individual transmitted picture so that it can be subjected to prolonged examination. Optimum quality in single-picture exposure and readout required for such a system requires a full understanding of the camera behavior under these conditions.

The quantitative information to be derived from a recorded image in a scientific experiment requires that (1) the position coordinates of a particular point relative to other points in the image be obtainable with high accuracy, and (2) a reliable photometric calibration be available so that the brightness of a particular object in the scene can be derived from the recorded signal intensity.

Fundamental Limits to Camera-Tube Performance

The video output from a camera tube may be pictured as consisting of a sequence of amplitude-modulated signals from elemental areas of uniform size. The signal amplitude is derived by counting at each element the number of electronic charges accumulated during an exposure interval. Because of the limit set by the normal statistical fluctuation in counting N events, the minimum theoretically detectable signal increment is $N^{1/2}$. This limit is not fully achieved in any real device, however, because of inefficiencies in making the count and because of limitations arising from such causes as incomplete collection of the charges, internally generated noise, and variations in the efficiency with which the stored charge is read out as a video signal.

A. Rose[3] has shown that this event-counting process provides a constant interrelationship between average scene brightness, resolution, and object-contrast detection limits. The performance limit of any real sensor in response to a single brightness level was shown to be equivalent to the result from a perfect device with its photoconversion element having an appropriate quantum yield less than unity. This concept provides a ready means for first-order comparison of relative performance between competing sensors and imaging systems.

[3] A. Rose, "Television Pickup Tubes and the Problem of Vision," *Advances in Electronics*, Vol. 1, p. 131, Academic Press, Inc., New York, 1948.

Because different camera tubes vary in their handling of the range of brightness levels found in any real scene, this basic comparison is subject to further modifications.

Available Camera Tubes

The image orthicon represents a well-known camera tube design that, over a limited operating range, comes very close to the ideal performance established by the photoelectron flux. The addition of intensifier stages that provide increased gain between the photocathode and storage target emphasize sensitivity at the expense of maximum resolution. A further trade-off between sensitivity and resolution is possible through variations in the storage-target capacitance.

When either transient phenomena or a faint input is to be recorded by prolonged integration, it becomes necessary to establish the performance capability of a camera tube for greatly varying exposure times. The particulars of such operation has been a major concern of our investigation.

Because the magnitude of the stored charge pattern is proportional only to the total quantity of radiant energy incident during the exposure interval, the most significant difference between open-shutter continuous scan and single-exposure operation comes during the readout. The scanning beam does not reproduce in the first scan the charge pattern stored by the target; instead it senses the potential at the scanned surface. Since the potential pattern of an elementary area of charge is more diffuse than the charge pattern itself, the resolution in the first scan is limited to a value that is significantly less than is observed when a fixed scene is scanned repeatedly. With repeated scanning, a balance is established between input and readout charge that effectively sharpens the potential pattern. Five or six scans of a fixed scene are required before the maximum resolution is obtained if the target–mesh spacing is small. A wide-spaced target assembly that is initially more degraded in resolution requires from twelve to fifteen scans to reach its resolution limit.

Although tubes with wide-spaced target assemblies are capable of detecting the lowest brightness objects, they do so at the expense of resolution. The present program has evaluated several different image-orthicon target spacings to determine the best compromise for the particular application.

Before reproducible experimental results could be obtained with independent exposures, it was necessary to analyze the detailed behavior of the tube in an operating procedure that consists of (1) a

prepare cycle (to eliminate effects from previous operation), (2) the optical exposure, and (3) the recording of a single readout scan.

The interval of time over which the target will integrate and store charge increases with increasing resistivity. The resistivity can be increased by lowering the operating temperature. A number of tubes containing a multi-alkali photocathode (S20) and a magnesium oxide target were operated in a camera that is housed in a thermally insulated enclosure. The entire tube is cooled by circulating air passed over dry ice. This arrangement ensures that moisture will not create leakage problems as the water vapor is condensed on the dry ice. At a temperature of —25°C on the tube face, integration and storage of a charge pattern for a period as long as 3 hours has been achieved.

The unmodulated fraction of current in the return beam developed by orthicon scan establishes a noise level and restricts the dynamic range within a single scene. A significant improvement in these characteristics can be achieved by using the isocon readout mode. The image isocon,[4] a variation of the image orthicon, utilizes those electrons scattered from the charge-storage surface during the readout scan to provide a video signal with large modulation. Special electron optics designed to separate the reflected-beam electrons from the scattered electrons are required. The use of isocon scan[5] in place of orthicon scan has resulted in an increase by a factor of three in signal-to-noise ratio and expansion by a factor of ten in the brightness range within a single scene that can be accommodated without readjustment of the scanning beam.

Isocon Scanning

A camera-tube storage target with its scanned surface at the equilibrium potential established by a low-energy scanning beam totally reflects the beam when there is no illumination present. Stored signal information adds a positive modulation to this surface permitting beam electrons to be accepted. A fraction of the electrons incident on the scanned surface will experience a nonspecular elastic scattering and will return to the gun end of the tube along with that portion of the beam that has insufficient axial energy to reach the target. The spread in initial energy of scattered electrons is broad, whereas energy variations among the specularly reflected electrons is restricted to a

[4] P. K. Weimer, "The Image Isocon—An Experimental Television Pickup Tube Based on the Scattering of Low-Velocity Electrons," *RCA Review*, Vol. 10, p. 366, Sept. 1949.

[5] A. D. Cope and H. Borkan, "Isocon Scan—A Low-Noise, Wide-Dynamic-Range Camera Tube Scanning Technique," *Appl. Optics*, Vol. 2, p. 253, March 1963.

small range, particularly in that component directed normal to the tube axis. Electron optics employed at the entrance to the electron multiplier allow only the scattered electrons to enter, with the result that when there is no stored signal at the target there is no output signal other than a small spurious d-c current.

The electron optics for separating the scattered electrons from the reflected portion of the scanning beam are shown in Figure 1. The

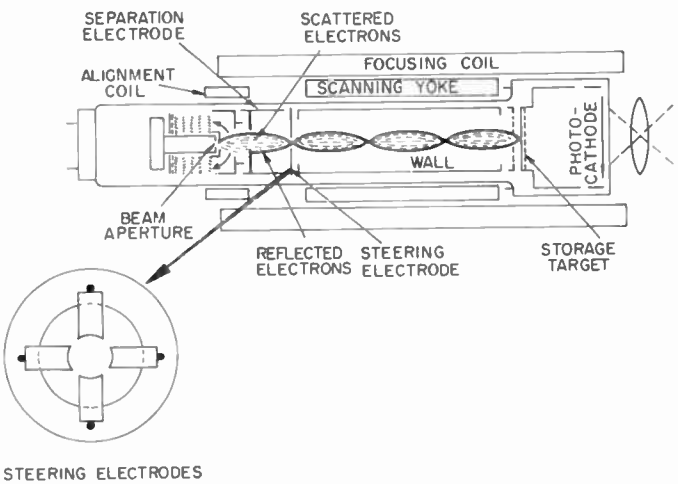

Fig. 1—Schematic diagram of image isocon tube.

collimated and focused beam is directed to the target with a combination of axial and radial velocity components that cause the reflected beam to be sufficiently off-axis to be intercepted by the separation electrode. If the decelerating region between the mesh and the target is small and if the equipotentials are flat surfaces parallel to the target plane, the reflected portion of an axially aligned scanning beam returning from any part of the target area retraces its path through the deflection region. The reflected beam occupies a small region of the tube at the plane of the separation aperture. In isocon operation, the addition of transverse energy to shift the reflected electrons off-axis where they are intercepted by the separation electrode does not materially increase their energy spread.

The higher energy beam electrons that strike the target and are elastically scattered have a variety of initial velocity directions. This process is nonspecular and these scattered electrons reach the separator plane at different radial positions, depending upon their initial radial

velocity component. Only those electrons with radial velocities matching the radial velocity of the reflected-beam electrons are trapped by the separator; the rest of the scattered electrons pass through the separator aperture and enter the electron multiplier.

The necessary radial component of velocity is added to the collimated scanning beam by a combination of the alignment field (an adjustable magnetic field directed at right angles to the tube axis) and the steering electrodes (which deflect the beam normal to the tube axis).

This particular isocon design also permits operation in the orthicon scanning mode, because the return current from an axially aligned beam will pass through the separation aperture unimpeded. Thus, an accurate comparison can be made of orthicon and isocon scan in the same tube using identical target modulation.

Isocon scan requires a uniform decelerating field with a high potential gradient in the region near the scanned surface of the target; this is provided by the mesh on the scanned side of the target. Orthicon tubes with a field mesh are available; their advantages have been demonstrated to be a more uniform center-to-edge performance in the output and better resolution. For either method of scan, there are inherent disadvantages in having the mesh in the path of the scanning beam. Electron transmission is only 60%, and the mesh contributes scattered electrons that do not represent signal modulation.

Camera-Tube Noise

The literature contains several derivations of a signal-to-noise expression for the image orthicon. That by Ramberg[6] uses the beam current necessary to achieve optimum signal-to-noise from a particular scene highlight as the reference parameter. The derivations by Vine[7] and Cope and Borkan[5] use the photocathode current as the reference parameter. The terminology and the equations derived in the appendix of Reference (5) are used in the discussion that follows.

Figure 2 indicates schematically the current flow at the target of the image orthicon and the noise associated with each current when the tube is operating below the target saturation level. The expression for the ratio peak-to-peak signal/rms noise derived in Reference (5) is

---

[6] E. G. Ramberg, "A Theoretical Analysis of the Operation of Flying Spot and Camera Tube Microscopes in the Ultraviolet," *IRE Trans. on Medical Electronics*, Vol. PGME-12, p. 58, Dec. 1958.

[7] B. H. Vine, "Analysis of Noise in the Image Orthicon," *Jour. S.M.P.T.E.*, Vol. 70, p. 432, June 1961.

$$\left(\frac{S}{N}\right)_{IO} = \sqrt{\frac{I}{2ef}}\sqrt{\frac{T(\delta-1)}{\delta + \dfrac{1}{\delta-1} + \dfrac{1}{m}}} = F_1(I)F_2(T,\delta,m)$$

The first factor, F_1, is the S/N for the photoelectron current I when operating in a video system with bandwidth f (e is the charge of the electron in coulombs). The second factor, F_2, contains parameters that pertain to the storage and readout of the video signal. The fraction of incident current transmitted by the target mesh is designated

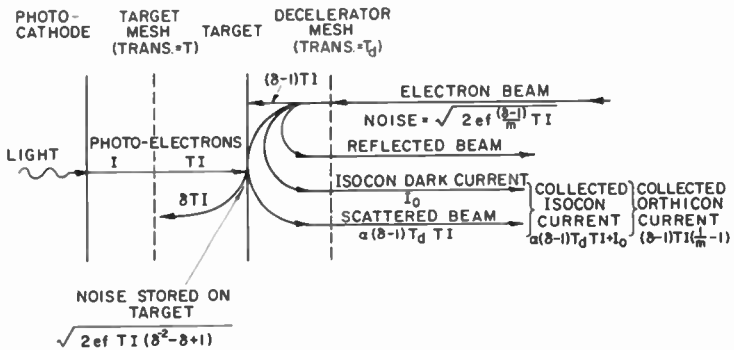

Fig. 2—Current flow in image orthicon and image isocon tubes.

by T, δ is the effective secondary emission of the target, and m is the fraction of the total beam current that is retained at the target. Figure 3a shows that for $\delta = 4$, the value of F_2 will not exceed 0.55 if m is unity. This ideal readout is not achieved in practice; typical values of m range between 0.3 at the highlight end of the photometric range and a vanishingly small value at the threshold signal limit. In a typical scene with large brightness variations, the beam modulation can be made optimum only for the highlight. At all other signal levels, a markedly reduced beam modulation is obtained and the dynamic range that can be reproduced is restricted to less than 50 to 1.

The ratio of the noise current associated with the stored charge at the target I_{nt} and the beam shot noise I_{nb} for the image orthicon is

$$\frac{I_{nt}}{I_{nb}} = \frac{\sqrt{m(\delta^2-\delta+1)}}{\delta-1},$$

which for $\delta = 4$ becomes

$$\frac{I_{nt}}{I_{nb}} = \sqrt{4.3m}.$$

The ratio is plotted in Figure 4 as a function of signal modulation,

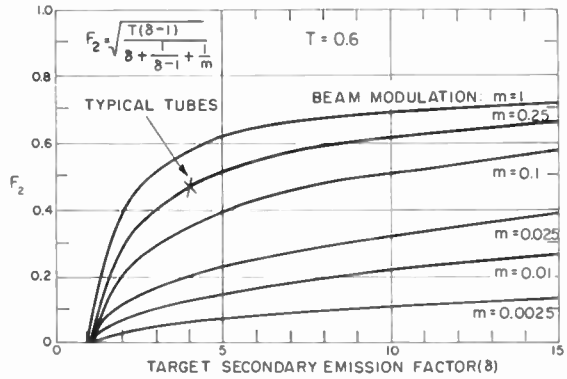

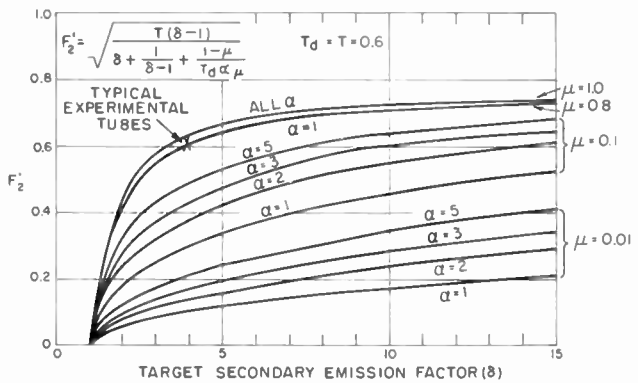

Fig. 3—Signal-to-noise modifying factor· (a) for image orthicon (F_2) and (b) for image isocon (F_2').

which is the same as the beam modulation. Because the value of m is less than 0.3 for most operations in the photometric range, the beam noise dominates. However, it is evident that the contribution of the fluctuations (noise) in the signal stored at the target cannot be ignored.

The signal-to-noise expression for the image isocon derived from the photocurrent and associated noise currents shown in Figure 2 is

$$\left(\frac{S}{N}\right)_{II} = \sqrt{\frac{I}{2ef}}\sqrt{\frac{T(\delta-1)}{\delta+\dfrac{1}{\delta-1}+\dfrac{1-\mu}{\alpha\mu T_d}}} = F_1(I)F_2'(\delta,\alpha,\mu,T,T_d),$$

where α is the scatter gain and μ is the output current modulation,

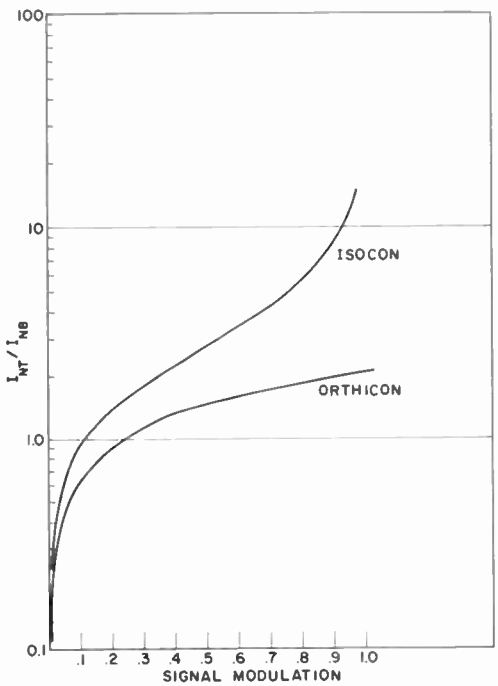

Fig. 4—Ratio of target noise to readout noise for orthicon and isocon scan.

given by

$$\frac{I_s'}{I_0 + I_s'}.$$

I_s' is the isocon signal current, I_0 is the isocon dark current, and T_d is the transmission of the decelerating mesh.

The term F_2' contains the operating parameters of the isocon tube. As shown in Figure 3b, for an effective target gain of $\delta = 4$, F_2' can reach a value of 0.65 when the output-current modulation is 100%. This value is a marked improvement over the image orthicon limit. What is of more significance in comparing Figures 3a and 3b is the

low values of F_2 and F_2' for low-light portions of a scene with wide dynamic range. Values of signal modulation for the image orthicon drop to less than 0.1 whereas those of the image isocon remain greater than 0.7. Typically, the signal-to-noise ratio of isocon scan is 3 times that achieved with orthicon scan of the same target signal.

For the image isocon,

$$\frac{I_{nt}}{I_{nb}} = \sqrt{\frac{T_d(\delta^2 - \delta + 1)}{(\delta - 1)\left(\frac{1}{\mu} - 1\right)}},$$

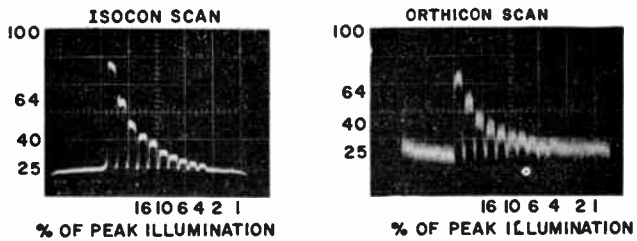

Fig. 5—Oscilloscope display showing the dynamic range produced by isocon and orthicon scan of a multi-tone scale. Continuous illumination and continuous readout was used, with the identical image stored at the target. Beam was optimum for highlight illumination of 5×10^{-8} phot second.

which for $\alpha = 3$, $\delta = 4$, $T_d = 0.6$ becomes

$$\frac{I_{nt}}{I_{nb}} = \sqrt{\frac{7.8}{\left(\frac{1}{\mu} - 1\right)}}.$$

This ratio as a function of signal modulation is shown in Figure 4.

For values of μ greater than 0.5, which is typical of the isocon operating range, the target noise dominates. The large dynamic range of the isocon is the result of retaining high modulation in the output current.

Figure 5 shows the oscilloscope display from a multilevel grey scale having the highlight at the top of the photometric range of the target. The brightness indicated for each successive step is in percent of the highlight value. One desirable feature of the isocon signal is the low noise in the dark portion of the scene. This is particularly attractive

for astronomical scenes consisting of a few point images of varying brightness in a dark background.

Figure 6 shows the noise current in the oscilloscope display for both orthicon and isocon readout when the signals are of equal amplitude.

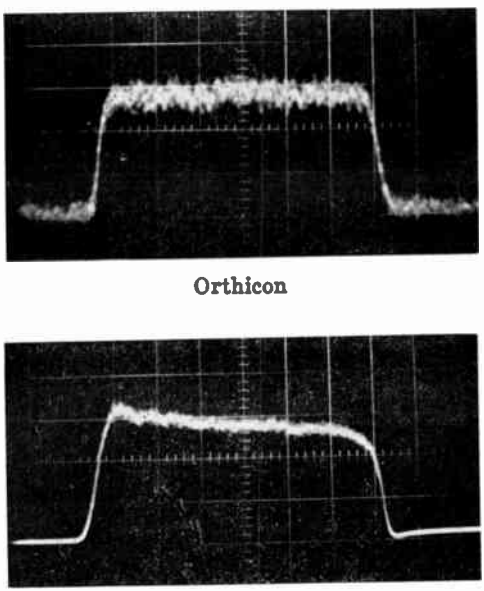

Orthicon

Isocon

Fig. 6—Oscilloscope display of the noise from the identical image for isocon and orthicon readout.

Integrated-Exposure Operation

The operating cycle adopted for the camera setup used in the experiments permits the use of exposures lasting 30 minutes or longer in order to integrate the energy collected from a low-level input. Figure 7 indicates the linear relationship between the input light flux and the exposure time to give the identical output signal. A stored charge of approximately 10^3 electrons in a 75-micrometer point image is characteristic of tubes with an S20 photocathode and a magnesium oxide target. No loss in resolution has been detected in properly processed tubes when long integration has been employed.

There is a reduction in the high-frequency response of the first readout scan as compared with the signal obtained after continuous

readout of a constant input pattern for a time sufficient to optimize performance. The number of scans required to reach this equilibrium is dependent upon the (1) target geometry, i.e., the spacing between the target and the secondary-electron collecting mesh, (2) the quality of the reading beam, and (3) the magnitude of the charge image stored on the target. Wider target–mesh spacings and small values of stored charge yield larger differences between first scan and steady-state results.

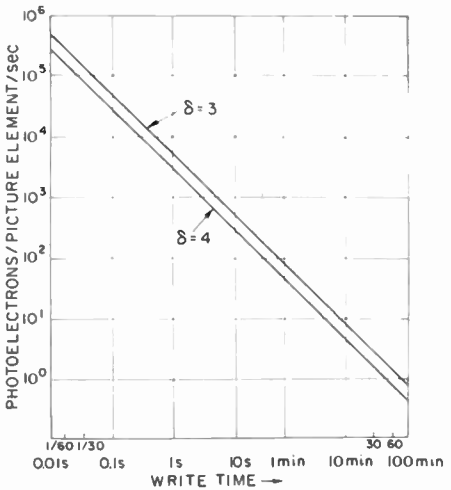

Fig. 7—Illumination versus exposure time to obtain the same readout signal.

Several characteristics of image-orthicon performance have required special attention in the operating cycle adopted for the Stratoscope integrating camera. To conserve transmission bandwidth, a one-second vertical scan rate with 500 noninterlaced lines is being used. During extended exposures the electron gun and heater are not operated; during the readout cycle the image section of the tube is not operated and a gun warm-up interval is introduced prior to the readout scan.[8]

Reducing the horizontal sweep rate by a factor of 15.6 favors the tube performance in several ways. (1) The reduced reading-beam current gives a smaller beam spot on the target. (2) A larger fraction of the stored signal is removed by the first scan, which increases both

[8] L. E. Flory, W. S. Pike, J. M. Morgan, and L. A. Boyer, "A Programmable Integrating Television System for Use with the Stratoscope," 3rd Symposium on Photoelectronic Image Devices, Academic Press, in print, 1965.

the first scan signal amplitude and the signal-to-noise ratio. As a result, slow scan provides a reduction of one stellar magnitude in the threshold detectable illumination. (3) The reduced scanning-spot size permits more scan lines per unit area to be used while maintaining optimum spacing between adjacent lines. Isolated point images in a dark field are not so readily detected as extended areas of the same brightness. A greater difference in the minimum detectable intensity is observed when the size of a test object in the image is reduced from 4×4 mm^2 on the photocathode to the 75-micrometer-diameter star image than can be ascribed to the frequency-response characteristic of the particular image orthicon. Investigation has shown that the beam removes a smaller fraction of the charge in the point image during the first scan than is removed for extended images, but that this discrepancy can be overcome by either the addition of background light or, preferably, applying a 1-volt increase to the target voltage immediately before readout. The signal-generating capability of the scanning beam increases as the average target potential rises by several volts. Under constant illumination and continuous scan, the target potential adjusts itself to optimum conditions of charge exchange. The biasing employed for increasing the first scan readout of point images accomplishes by external means that which is usually an auto-adjustment.

A comparison of isocon scan and orthicon scan using continuous illumination and continuous readout is given in Figure 8. These pictures were obtained by readout of the same target in a tube capable of operating in either mode. Measurements using integrated exposures followed by a single readout with isocon scan are in progress.

Stellar Spectroscopy

A difficult astrometric problem for which an integrating image-recording system should be helpful is that of measuring the spectra from faint sources. Preliminary results have been obtained using a spectrometer having a dispersion of one angstrom per millimeter attached to the 23-inch refracting telescope in the Princeton University Observatory. The spectrum was imaged on the face of the image isocon tube with the dispersion axis at right angles to the scanning lines of the television raster. Because the spectrum illuminated only 1/50 of the horizontal width of the raster, a gating circuit was employed to select the signal from only that portion of the line that contained the input.[8] Figure 9 shows the oscilloscope display from the 500 active scan lines when the spectrum from Arcturus (magnitude 0.2) was recorded using an 8-second exposure followed by one isocon

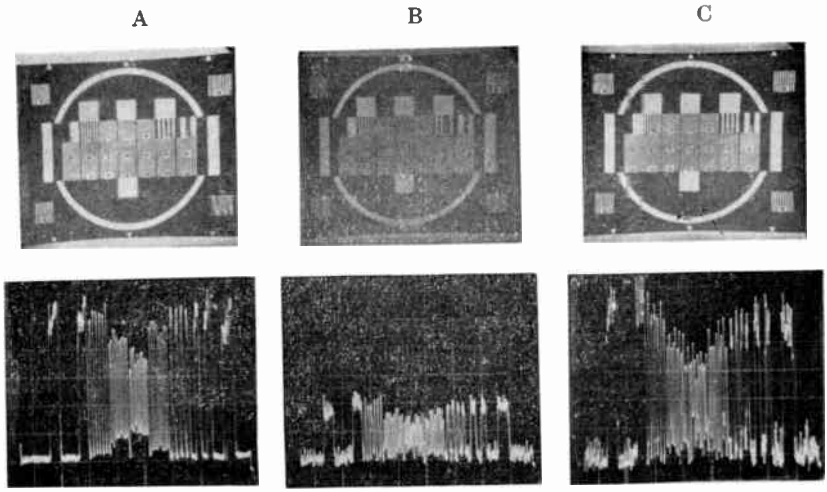

Fig. 8—Continuous illumination and continuous readout of a test pattern read by isocon and orthicon scan. The column A photos show the kinescope and oscillograph displays for isocon readout of the identical stored charge image shown in the column B photos for which orthicon readout was used (note the amplitude difference). The column C photos show the orthicon readout results when the video gain had been increased to provide signal amplitudes equivalent to the isocon signal (note the difference in noise, particularly in the black portions of the scene).

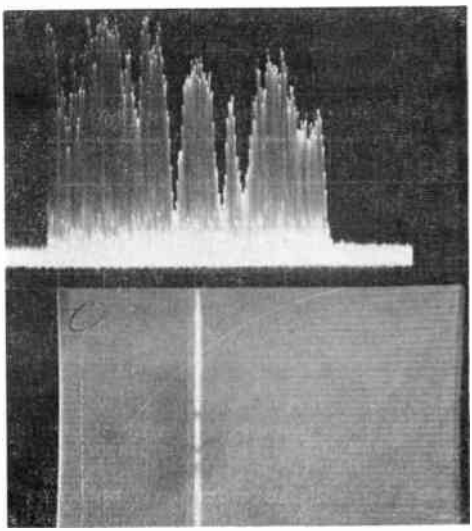

Fig. 9—Image isocon record of a 70-angstrom portion of spectrum in the region of 5180Å using an 8-second exposure to Arcturus. The lower image is the kinescope display of the spectrum.

readout scan. In the video display shown in the lower section of the figure there are 8 resolution elements in each of four lines per angstrom of the spectral input.

The display shown in Figure 10 was obtained from a 176-second exposure of a third-magnitude star by accumulating in an integrator the output from each scan line that passed the gate. In each instance the continuum charged the target to about 70% of full capacity. The seeing conditions were different for the observation of Figures 9 and 10, so that exposures do not correlate with the known differences in stellar magnitude.

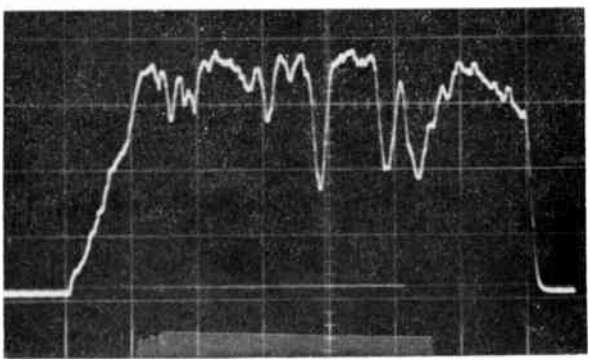

Fig. 10—Image isocon record of a 70-angstrom portion of the spectrum in the region of 5180Å using a 176-second exposure of the 3rd magnitude star F. Virginius. The total output of each scan line was integrated and recorded as a single point in the display.

The conventional spectral-recording technique for this spectrometer employs pulse-height discrimination of the output from a photomultiplier and counting for an interval of from 10 to 15 seconds at points an angstrom apart. The total time required for recording the spectrum is equivalent to the camera-tube exposure time. The S/N of the camera tube is within a factor of three of that obtained from counting approximately 10^3 pulses per point. With the camera tube and operating cycle adjusted for optimum results, a further reduction in noise and improved sensitivity appears to be possible. The unlimited increase in counting time that is available for the photomultiplier is not available to the camera tube because of its finite charge-storage capacity.

Future Plans

Distortion in the stored charge pattern at the target when the highlight illumination excites more charge than can be stored seriously affects image quality. The high flux of secondaries from a bright

portion of the image is not completely collected by the target mesh and rains upon surrounding areas of the target, producing a black halo surrounding the highlight. Closer spacing between the insulator membrane and the mesh reduces but does not eliminate this problem. Means for overcoming this distortion must be achieved before either the image orthicon or image isocon will be able to provide a predictable relationship between signal amplitude and the absolute brightness of all possible intensities in the scene.

Image orthicon and image isocon tubes with close-spaced target–mesh assemblies and highly insulating targets appear to provide the best expectation for (a) high resolution on first scan readout, (b) high signal-to-noise ratio, and (c) minimum distortion of the stored charge image through redistribution of secondaries in the image section when the input contains a broad range of illumination intensities.

The great range of useful output signal from the isocon requires modification of the conventional means for display of the video. The present kinescopes for either direct observation or photographic recording cannot reproduce the entire range of available video information.

Acknowledgments

This work has largely been supported by the Stratoscope II project of the Department of Astrophysical Sciences, Princeton University under the direction of Prof. Martin Schwartzchild. Project Stratoscope is jointly sponsored by the National Science Foundation, the Office of Naval Research, and NASA.

VIDICON PERFORMANCE CHARACTERISTICS AT SLOW SCAN RATES

By

R. E. Johnson

RCA Electronic Components and Devices
Lancaster, Pa.

Summary—This paper presents performance data for vidicon camera tubes using a "standard" photoconductor and for tubes using a new photoconductor especially developed and processed for slow-scan applications. The data presented demonstrate the advantages of the slow-scan photoconductor over the standard type for application in space-vehicle camera systems.

UNTIL THE present decade, television camera tubes were operated under the conditions specified for standard broadcast service except for a very few specialized applications. Consequently, they were designed for optimum performance in this operating mode and almost all published data were expressed in terms of standard broadcast scan rates and light exposures.

The advent of serious space explorations has, however, imposed new operating requirements on camera-tube performance. In such applications, video signals must be generated at very slow rates of scan to conform to narrow bandwidth requirements and conserve transmitter power. In addition, basic tube construction must be compatible with extreme environmental parameters such as heat, shock, vibration, and nuclear radiation.

Over the past few years, several reliable camera-tube designs for space applications have been developed and performance data of special value to the designers of space-vehicle camera systems have been accumulated. This paper presents a detailed analysis and summary of this information.

The Photoconductor Material

The primary capabilities (or basic limitations) of a vidicon for either conventional or slow-scan applications are generally defined by the photoconductive material used to form the light-conversion element. Although the light-sensitive surface is completely separate from the electrical readout element in some other camera tubes, in the vidicon the photoconductor alone provides both the photoconversion and the storage functions.

The standard photoconductor used in tubes designed for live-pickup broadcast service (such as the 7735B) is also useful to some degree in slow-scan applications. However, maximum performance in such applications is obtained by use of a new photoconductor especially developed and processed for slow-scan applications.

The key performance characteristics of both standard and special "slow-scan" photoconductors are presented in this paper, and the relative advantages and disadvantages of each type are discussed. All the data were measured in the same electro-optical configuration, i.e., a one-inch-diameter all-magnetic structure similar to that of the 7263A vidicon. A similar tube configuration has been used in most space explorations to date. It is assumed that relative performance of 1-inch hybrid and 1-inch all-electrostatic tubes can reasonably be extrapolated from the data presented here together with the published scan data for the particular type being considered.

Test Procedure and Recorded Data

It was anticipated that the following vidicon characteristics would probably be most critically affected by a change in scanning speed:

(1) reciprocity of light-exposure parameters,
(2) dark current,
(3) signal current,
(4) signal storage,
(5) residual signal or lag, and
(6) resolution or response to image detail.

Consequently, these parameters were selected for measurement in a test setup in which frame scan rates could be continuously varied from a fraction of a second to as much as 30 seconds. Although horizontal scan rates could also be varied independently over a wide range, it seemed advisable to set horizontal rates to maintain a 500-line, non-interlaced raster for each test run. In this way, other scanning factors that might have a coincidental effect on these characteristics would tend to remain constant.

After the reciprocal nature of light-energy exposure was definitely established, the desired illumination levels were arbitrarily obtained by a convenient combination of shutter speed, lens speed, and neutral density filters (where required). Color temperature of the incandescent light source was maintained close to 2870°K. In addition, because the characteristics of the photoconductors are greatly affected by thermal environment, the temperature of the vidicon faceplates was carefully maintained at 30°C. Size of the optical image on the faceplate was always set at 0.44 by 0.44 inch.

Reciprocity of Light-Energy Parameters

Conventional television-camera systems are normally operated with an open shutter and with the optical lens speed (f number) adjusted to provide optimum light exposure of the scene on the faceplate of the camera tube. Because broadcast standards are selected to match the viewing characteristics of the human eye, very little objectionable smearing of moving objects or similar bad effects are detectable in these systems. At the same time, the use of a frame-scan interval of 1/30 second capitalizes on the storage characteristics of the camera tube to improve the sensitivity of the system. A frame time of 1/30 second is therefore often regarded as the equivalent shutter speed of the optical elements.

In slow-scan pickup, the repetition rate permits substantial movement of the televised subject during the frame-scan interval; this could cause intolerable blurring of the image. Consequently, almost all slow-scan systems use a controlled optical shutter speed to determine exposure. It is important, therefore, to determine whether a reciprocal relationship exists between various shutter speeds relative to total light exposure. In other words, if a vidicon is exposed to an illumination of 0.1 footcandle with a 100-millisecond shutter, will it provide essentially the same signal as if it were exposed to one footcandle with a 10-millisecond shutter?

The results of tests conducted to determine whether this reciprocity relationship exists for the photoconductors under consideration are shown in Figure 1 for the "slow-scan" surface and in Figure 2 for the "standard" surface. Each figure includes individual signal-output points corresponding to certain total light-energy levels (or exposures) expressed in footcandle-seconds (fcs).

However, the total light-energy levels were obtained with different absolute light-intensity levels in combination with a variety of shutter speeds. The measurements were then repeated to include all scan rates of interest to form the composite curves.

In Figures 1 and 2, some departure of the individual points from exact superposition is evident in almost every instance. However, the departure is well within the anticipated errors of practical measurement. It is established, therefore, that a reciprocal relationship prevails for both surfaces, at least within the shutter-speed range investigated (one millisecond to one second).

As a result of these tests, all subsequent data were normally measured with an intermediate shutter speed of 100 milliseconds, because this particular speed provided maximum reliability and convenience in exposure settings.

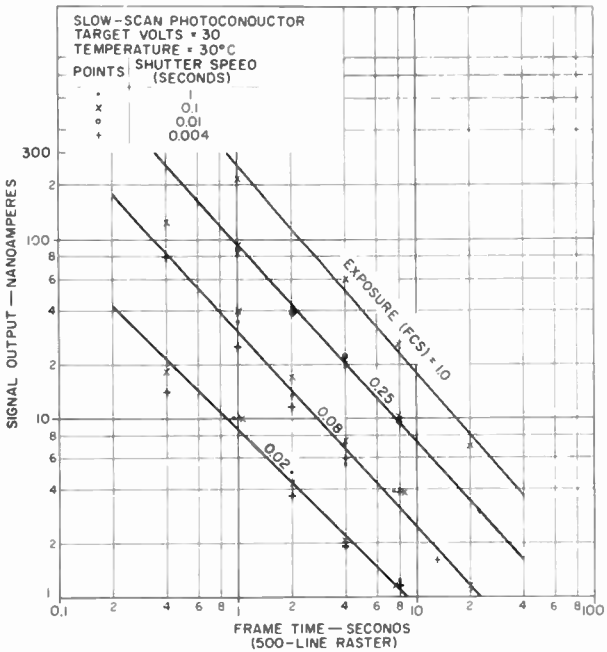

Fig. 1—Light-energy reciprocity curves for slow-scan photoconductor.

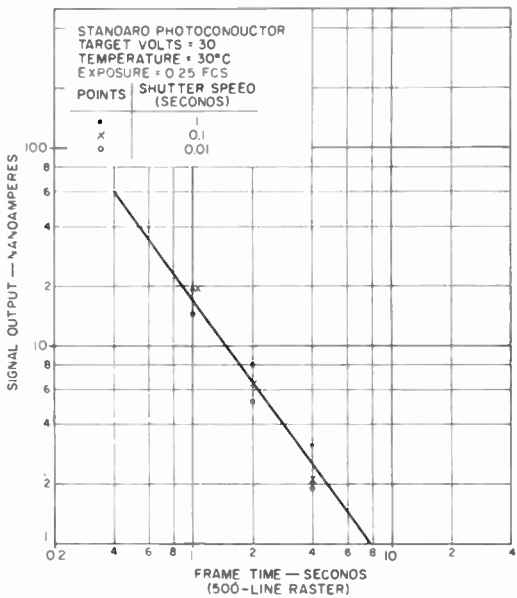

Fig. 2—Light-energy reciprocity curve for standard photoconductor.

Signal Output at Slow Scan Rates (Light-Transfer Curves)

The data presented in Figures 1 and 2 established that higher signal currents result from any of the following basic factors:

(1) higher total energy levels of illumination (footcandle-seconds),
(2) higher vidicon target voltages,
(3) faster scan speeds (due to more rapid target discharge).

In addition, signal output is dependent on the faceplate temperature even if the dark current is held constant by adjustment of target voltage.

Figures 3 to 9 demonstrate the dependence of signal current on the parameters listed above* with temperature held at some constant value (arbitrarily selected as 30°C for convenience and coincidence with typical applications). As before, shutter speed was standardized at 100 milliseconds and image size at 0.44 by 0.44 inch on the faceplate of the vidicon tube. Data were measured under these conditions to obtain the typical signal-output curves presented.

Figure 3 shows the rate of change of signal-output current as a function of scan speed for a typical slow-scan photoconductor exposed to a number of light-energy values within the limits of its normal operating range at a constant typical target voltage of 30 volts.

Figure 4 shows the variation of signal-output current with target voltage at a typical optimum light exposure of 0.25 footcandle-second. Typical light-transfer curves for this surface for all useful scan rates are shown in Figure 5. Expanded curves for selected scan rates and a full range of target voltages are shown in Figures 6 and 7. The data for these particular curves (which were taken with greater than normal care) show that gamma remains fairly constant in the range of 0.70 to 0.75 for all scan speeds, target voltages, and light values within the optimum operating ranges.

Similar curves for the standard photoconductor at typical operating voltages are shown in Figures 8 and 9.

The following general conclusions may be drawn from the data shown in Figures 3 to 9:

(1) As anticipated, signal output of all surfaces drops off pro-

* It should be noted that absolute values of signal current may not be identical for ostensibly identical conditions on all curves, because different tubes may have been used for various test runs. These slight differences reflect, to some degree, the variable performance characteristics inherent in individual tubes of a particular design.

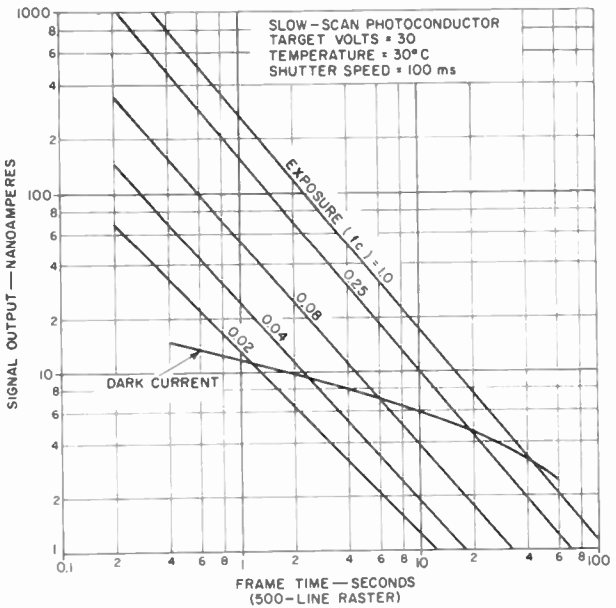

Fig. 3—Signal output as a function of scan speed for the slow-scan photoconductor for several values of illumination.

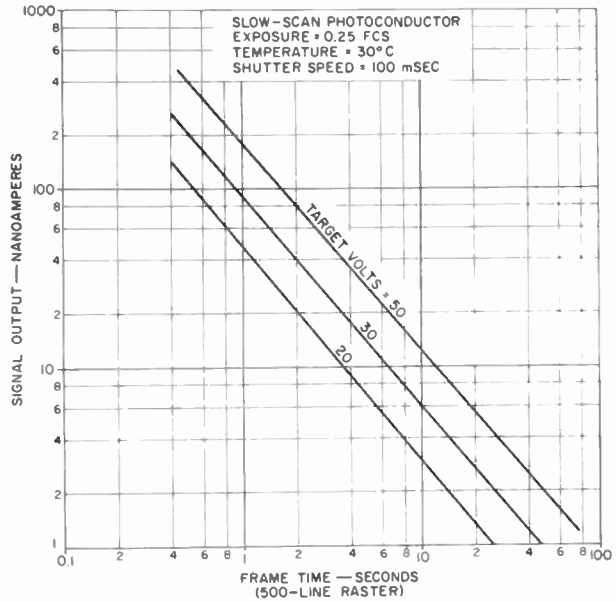

Fig. 4—Signal output as a function of scan speed for the slow-scan photoconductor for several values of target voltage.

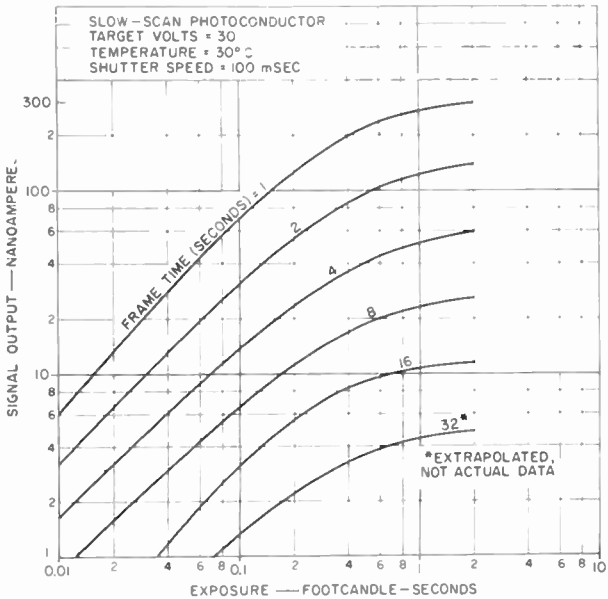

Fig. 5—Light-transfer curves for the slow-scan photoconductor for several values of scan speed.

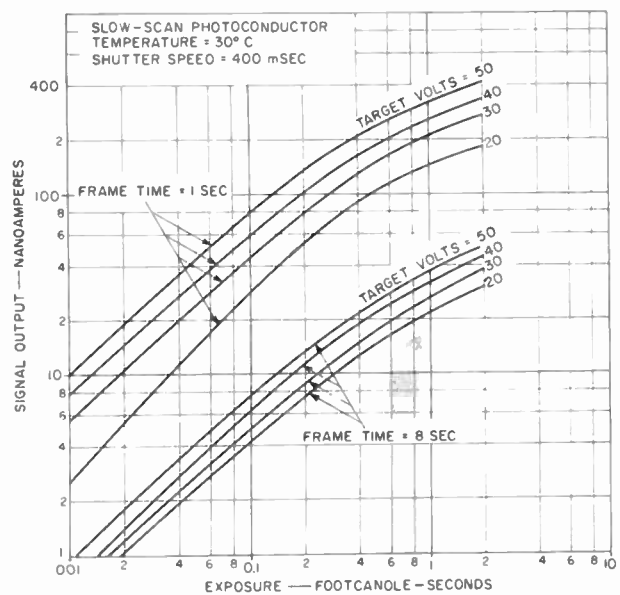

Fig. 6—Light-transfer curves for the slow-scan photoconductor for various target voltages at two different scan speeds.

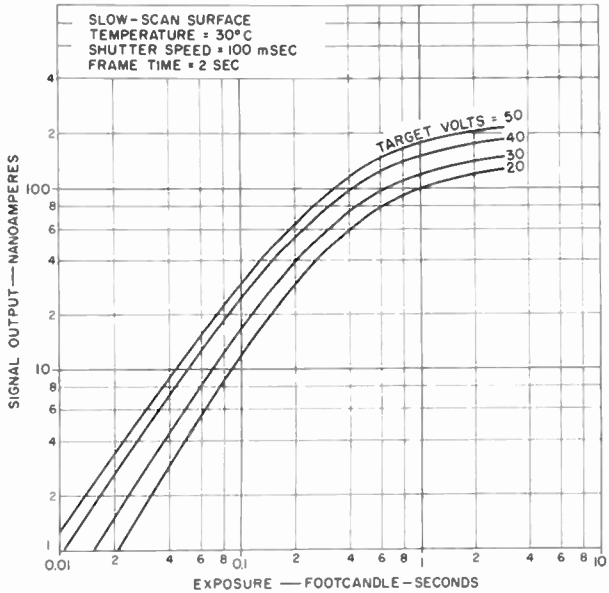

Fig. 7—Light-transfer curves for the slow-scan photoconductor for several values of target voltage.

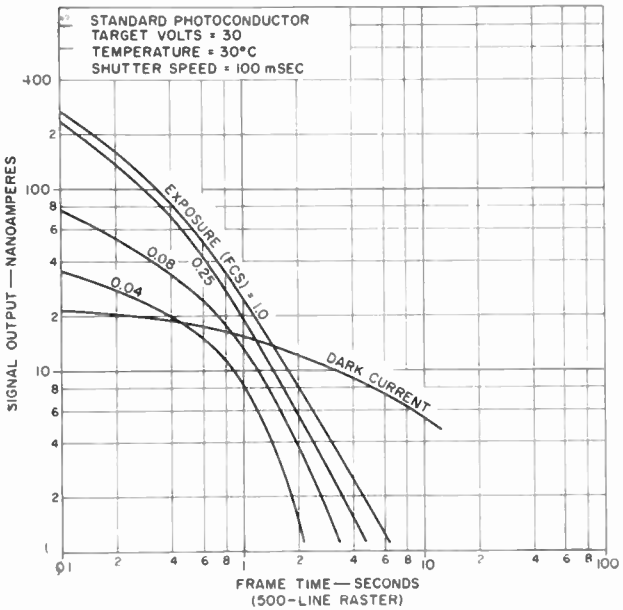

Fig. 8—Signal output as a function of scan speed for the standard photoconductor for several values of illumination.

portionately as scan speed is reduced. The special slow-scan photoconductor with high sensitivity and excellent storage provides best performance range. The standard photoconductor with good sensitivity and good storage is also useful at slow scan rates, but is limited at a much earlier stage than the special surface.

(2) The special slow-scan photoconductor may be considered useful at frame times as long as 30 seconds when illumination equal to

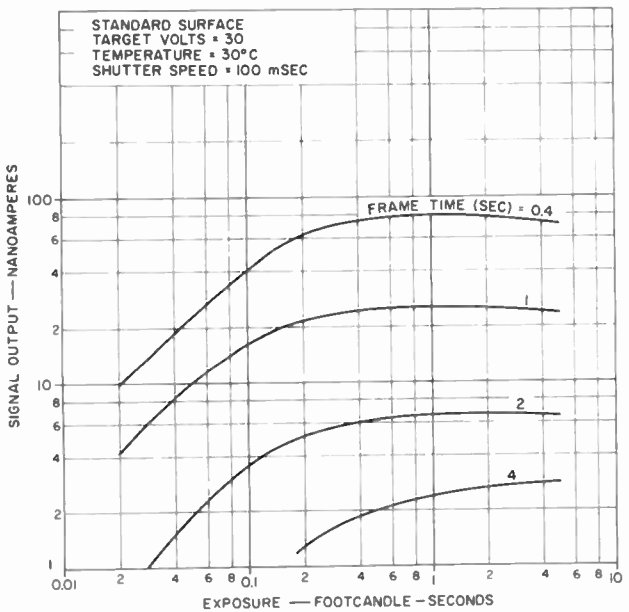

Fig. 9—Light-transfer curves for the standard photoconductor for several values of scan speed.

at least 0.2 footcandle-second is available. At a frame time of one second, this surface may be useful at illumination levels of 0.003 footcandle-second or less.

(3) The usefulness of the standard television surface is limited to frame-scan intervals that do not exceed 5 seconds. Beyond this point, signal output is generally prohibitively low for all practical illumination levels.

Dark Current at Slow Scan Speeds

Dark-current characteristics for the special slow-scan photoconductor and the standard surface are shown in Figures 10 and 11, respectively. Although there is some drop-off in absolute current levels

for longer scan periods, the dark current read out as part of the signal tends to remain fairly constant when the extreme range represented by the scan speed itself is considered. It can generally be assumed, therefore, that a linear increase in dark-current charge corresponding to the frame-scan interval is normally compensated by an equivalent reduction in dark-current signal level caused by the slower rate of scan. The apparent reduction in dark-current level is, therefore, probably related to the storage characteristics of the particular photoconductive material. This assumption is supported by the fact that the

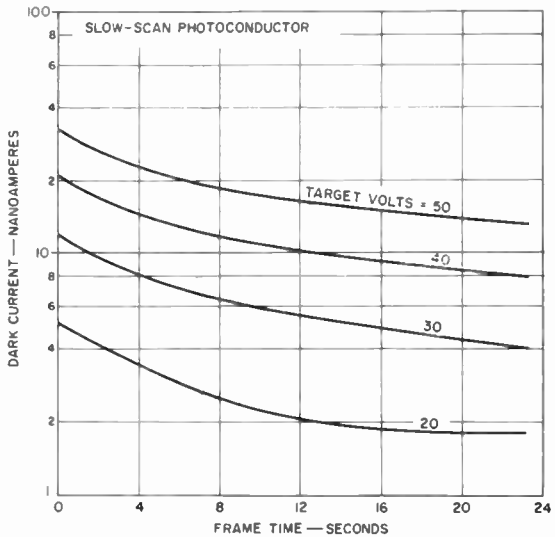

Fig. 10—Dark current as a function of scan speed for the slow-scan photoconductor for several values of target voltage.

dark current falls off at a noticeably slower rate in the slow-scan surface than in the standard surface, which has poorer signal-storage characteristics.

Although no actual measurements were made, it is probably safe to assume that the same behavior pattern would be observed in signal-output curves when vidicons are operated "open-shutter". That is, the longer effective light-exposure time would be almost exactly counterbalanced by the slower read-out rate so that signal currents would remain essentially constant. As in the case of dark currents, however, a gradual decrease in signal level would be expected at slower scan rates consistent with the storage characteristics of the particular photoconductor.

The dark-current curves shown in Figures 10 and 11 may be superimposed on the signal curves shown in Figures 3 to 9 to obtain a graphic presentation of the relationship of signal current to dark current at any frame scan rate of interest for a particular vidicon target-voltage mode. This relationship is sometimes of particular interest in determining what conditions of light exposure and scan rate will cause the signal current to deteriorate to the typical dark-current levels for a particular device. Figures 3 and 8 show both the

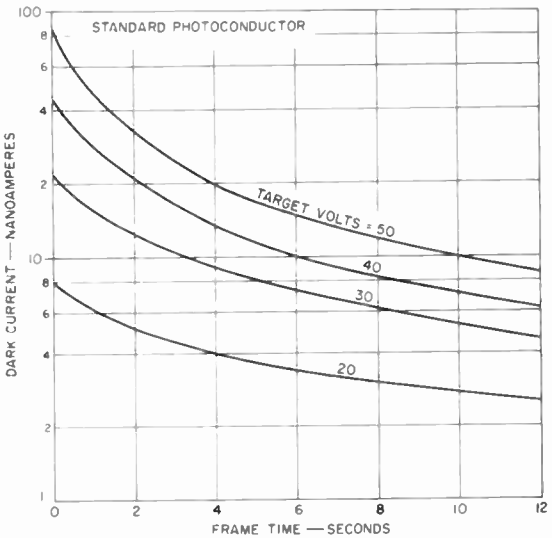

Fig. 11—Dark current as a function of scan speed for the standard photoconductor for several values of target voltage.

dark current and the signal current for certain typical conditions for the two photoconductors under consideration.

Response to Image Detail at Slow Scan Rates

There is some deterioration in image sharpness as scan rates become slower, primarily because of the storage characteristics of individual tubes or individual tube types, although certain other secondary effects could also be involved. Figures 12 and 13 show the amplitude response of the typical slow-scan photoconductor to selected fine picture detail of 250 and 400 lines, respectively, as the frame scan rate is varied. The four curves in each group represent four typical light levels within the normal operating range of the device. Similar curves for a standard surface, shown in Figures 14 and 15, indicate

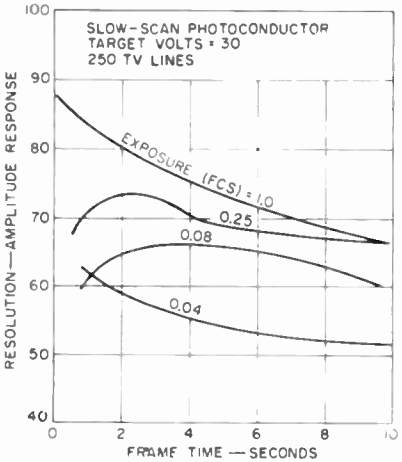

Fig. 12—250 television-line response of the slow-scan photoconductor.

a much steeper rate of decline in resolution; in addition, the useful scan rates are much more limited, as indicated previously.

The very definite peak in the response characteristic in the one-to-two-second scan-rate interval is very interesting. Similar data taken at broadcast scan rates on a large number of standard tubes show that the amplitude response (effective resolution) is generally below that normally observed with slow scan. It is speculated that the higher beam currents required by television scan rates have a

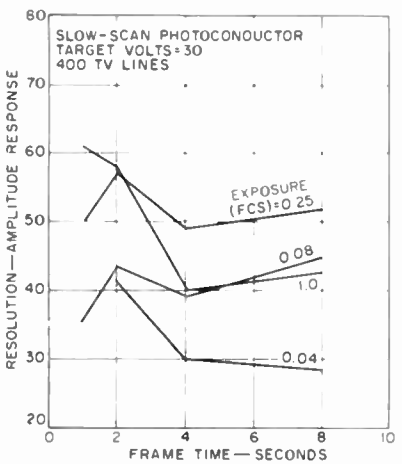

Fig. 13—400 television-line response of the slow-scan photoconductor.

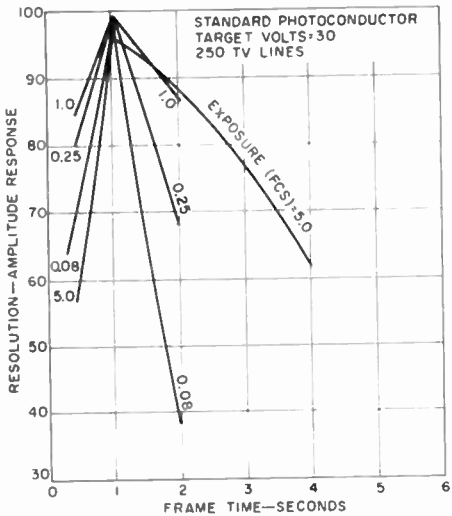

Fig. 14—250 television-line response of the standard photoconductor.

pronounced effect on beam size and shape that acts to limit the resolution performance attainable. The fall-off in response as scan rates become even slower than one or two seconds is undoubtedly associated with the storage characteristics of the photoconductor.

In general, it can be concluded that each photoconductor retains a very high degree of picture sharpness over its complete range of usefulness. In other words, the range of usefulness in all slow-scan applications will normally be limited by the signal-output level attainable rather than by any extreme changes in resolution experienced within this established range.

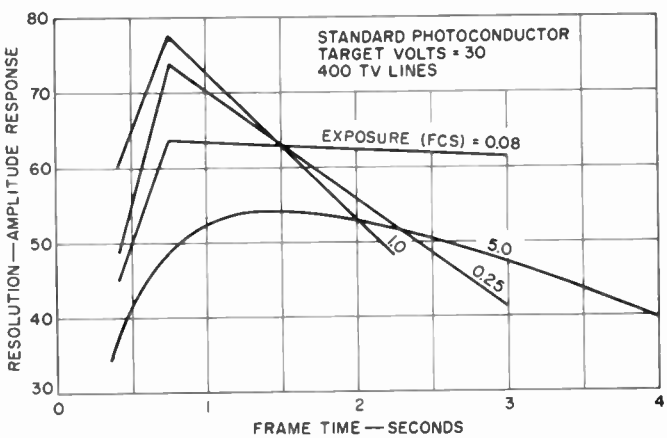

Fig. 15—400 television-line response of the standard photoconductor.

Residual Signal at Slow Scan Rates

The typical lag, or residual-signal, characteristics for the slow-scan and the standard surfaces are shown in Figure 16. It has been found that decay of signal or, more properly, rate of erasure is uniquely dependent on the number of scans as opposed to any absolute elapsed-

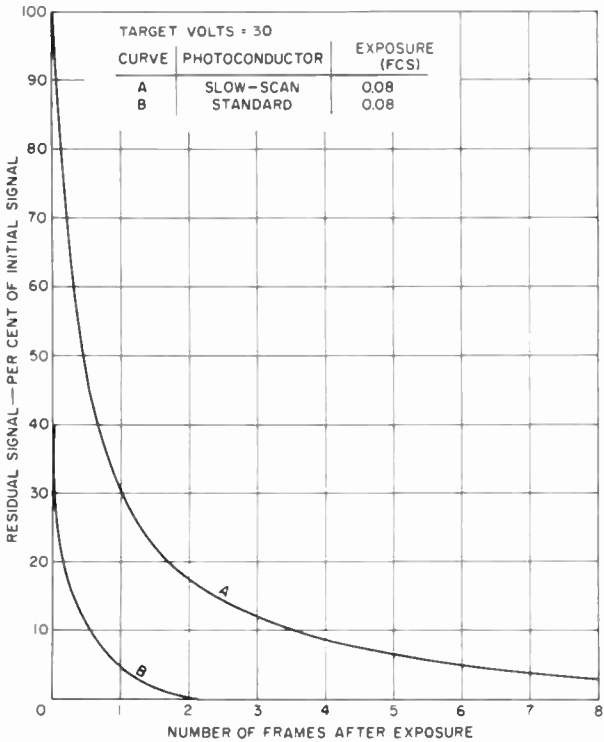

Fig. 16—Lag characteristics of slow-scan and standard photoconductors.

time base. The slow-scan photoconductor, for example, typically requires 5 to 10 frame scans to reduce the signal to less than 5 percent, and this requirement is essentially independent of frame scan rate. Thus, if the scan rate is 1 frame per second, it will take at least 5 seconds to reach the 5-percent level. Similarly, if the scan rate is 5 frames per second, it will take only about one second; if a 5-second frame rate is employed, it will require 25 seconds or more to reach the same level.

Because both surfaces have this same natural characteristic, the signal-decay curves under continuous scan and read-out conditions can

be plotted on the same axes with the number of frame scans after exposure as the independent reference. As noted above, the slow-scan surface exhibits the most persistent lag characteristic, requiring 5 to 10 scans for reasonable extinction. The standard surface is very fast by comparison, completing the same degree of erasure in 1 to 3 scans.

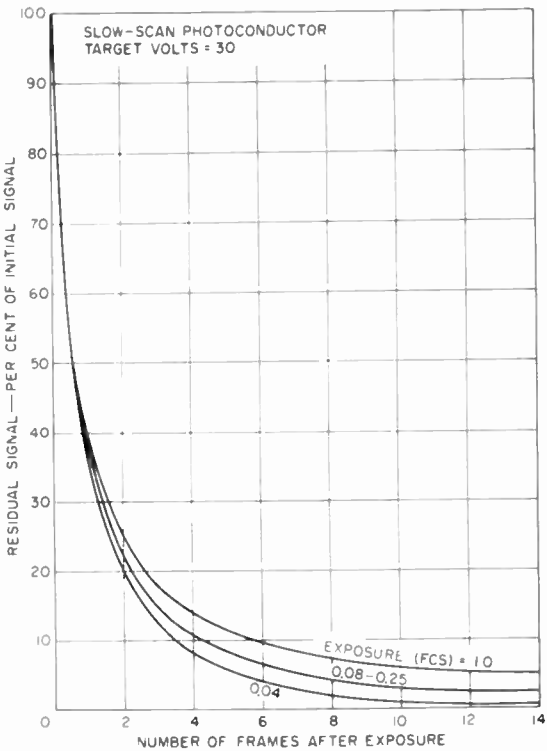

Fig. 17—Lag characteristics of the slow-scan photoconductor for several values of illumination.

The residual signal characteristic is not critically affected by light intensity, but is moderately dependent on this parameter, as shown for the slow-scan surface in Figure 17.

The same general degree of dependence is apparent with respect to operating target voltage; as shown by the curves in Figure 18, higher target voltages result in significantly more rapid erasure.

Signal Storage as a Function of Scan Speed

No specific relationship between frame scan speed and relative storage capabilities of the various photoconductors was anticipated.

On some individual tubes under certain conditions of operation, none was evident, as shown in Figure 19. This curve represents a typical slow-scan tube measured under the optimum operating conditions indicated.

On most test runs for the slow-scan surface, however, a very definite variation of storage characteristics with scan speed was evi-

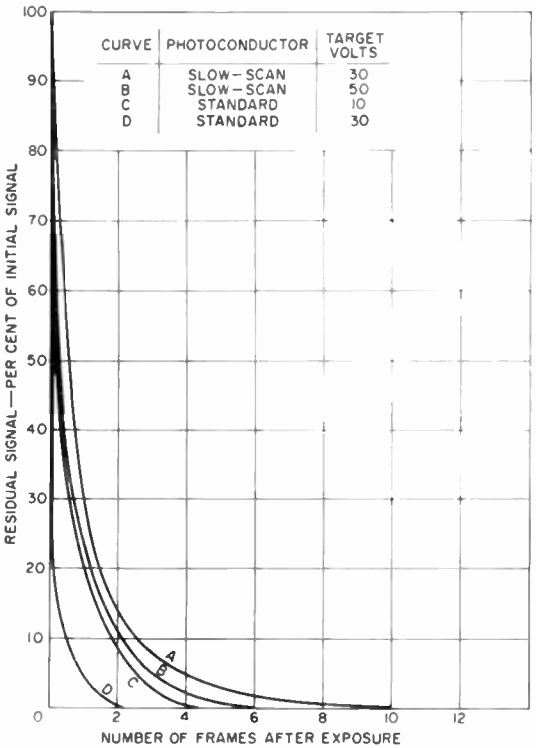

Fig. 18—Effect of target voltage on lag characteristics of the slow-scan and standard photoconductors.

dent, as shown in Figure 20. Slower scan speeds appear to generate improved, very long storage characteristics, while faster scans generally are subject to more rapid decay. A rigorous explanation for this phenomenon has not been developed to date, but this effect was not observed in any of the standard photoconductors evaluated. High target voltages also result in poorer storage characteristics in the slow-scan photoconductor as shown by comparison of the curves in Figures 20 and 21. The typical effect of target voltage over the useful operating range is shown in Figure 22.

The effect of illumination level and or signal level has not been

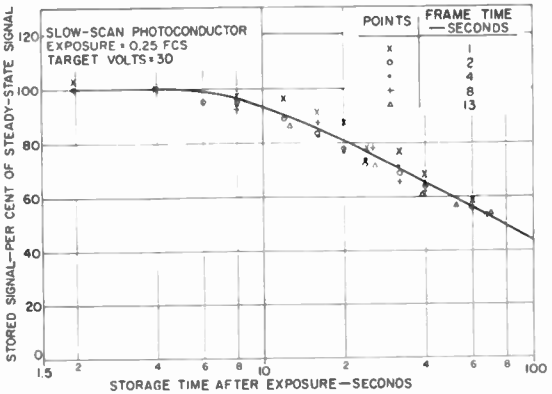

Fig. 19—Signal storage of the slow-scan photoconductor at various scan speeds with an illumination of 0.25 footcandle-second and a target voltage of 30 volts.

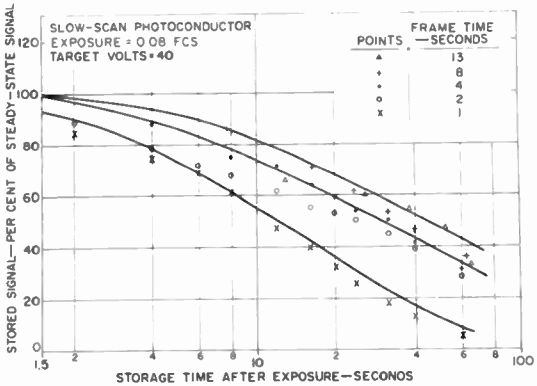

Fig. 20—Signal storage of the slow-scan photoconductor at various scan speeds with an illumination of 0.08 footcandle-second and a target voltage of 40 volts.

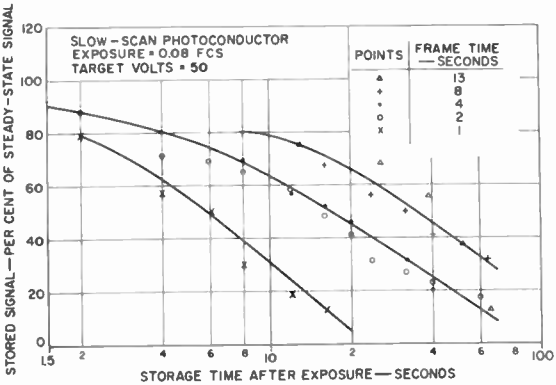

Fig. 21—Signal storage of the slow-scan photoconductor at various scan speeds with an illumination of 0.08 footcandle-second and a target voltage of 50 volts.

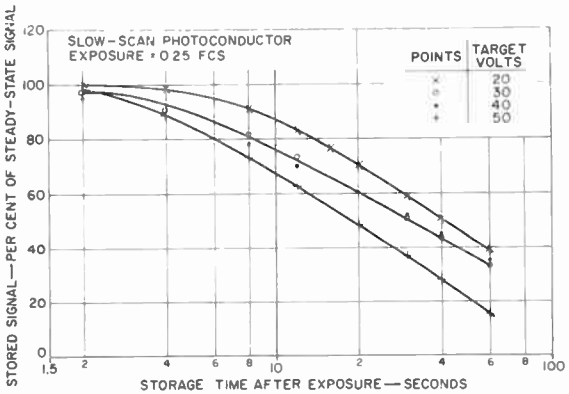

Fig. 22—Effect of target voltage on signal storage of the slow-scan photoconductor.

thoroughly investigated to date. However, it appears that the higher signal levels resulting from higher illumination levels tend to persist the longest and thus result in a slower rate of decay, or higher rate of storage, as noted in the normalized family of curves shown in Figure 23.

All of the data on signal storage presented thus far are applicable only to the slow-scan photoconductor, which has clearly demonstrated exceptional capability in this respect. Similar curves for the standard photoconductor demonstrate the relatively poorer storage characteristics of this surface.

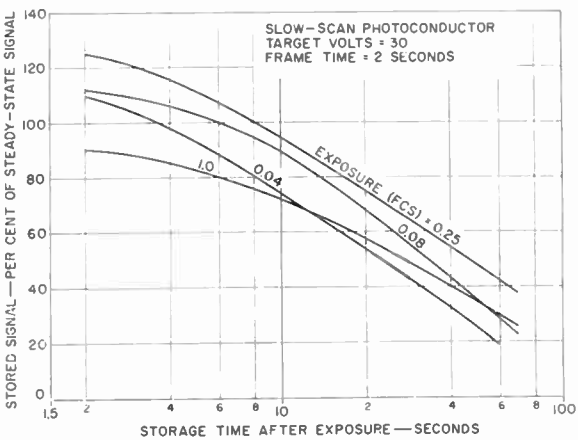

Fig. 23—Effect of light level on signal storage of the slow-scan photoconductor.

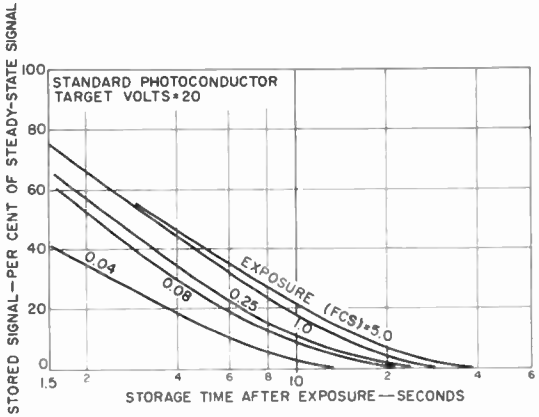

Fig. 24—Effect of light level on signal storage of the standard photoconductor.

Figure 24 shows a complete family of curves that demonstrate the variation typically experienced with changes in light level.

As with the slow-scan surface, higher light levels and/or higher signal currents apparently provide best storage. Data recorded at a target voltage of 30 volts show a virtually identical characteristic. No actual data have yet been recorded to determine the effect of very high target voltages. With the storage characteristic relatively poor at normal target voltages, however, any further deterioration due to high-target-voltage operation might prove to be intolerable. The fact that variation of frame scan speeds within the useful operating range has literally no effect on storage is clearly shown in Figure 25.

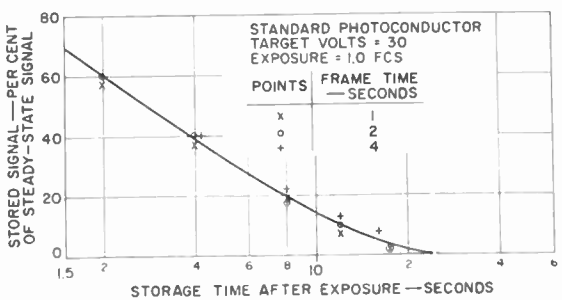

Fig. 25—Effect of scan speed on signal storage of the standard photoconductor.

Conclusions

The data presented demonstrate the advantages of the special slow-scan photoconductor over the standard photoconductor for slow-scan applications. Table I summarizes some of the important characteristics of both types of surfaces. The special slow-scan photoconductor surfaces have the very best slow-scan characteristics, except for residual

Table I

Photoconductor Material	Standard	Slow-Scan	
Tube Prototype	7263A	C-74072	
Typical Target Voltage	30	30	volts
Typical Dark Current	10×10^{-9}	6×10^{-9}	ampere
Typical Light Exposure	0.25	0.25	fcs
Typical Signal Output at frame time of			
1 second	20×10^{-9}	90×10^{-9}	ampere
2 seconds	8×10^{-9}	40×10^{-9}	ampere
4 seconds	2.5×10^{-9}	18×10^{-9}	ampere
8 seconds	—	8×10^{-9}	ampere
16 seconds	—	3.5×10^{-9}	ampere
Residual Signal (time to 5-percent level)	1-2	5-10	frames
Response (400 television lines)	65	50	per cent
Stored Signal (time to 50-percent level)	3	80	seconds

signal, of all materials currently available. Moreover, the lag is not excessively long or prohibitive for practical slow-scan systems. There are many methods for erasing the signal within the picture cycle in slow-scan systems that may not be feasible at the more rapid rates typical of television. The standard photoconductor layer has only about 1/5 the sensitivity of the slow-scan surface and is limited, by relatively poor storage characteristics, to slow-scan periods not exceeding 5 seconds maximum. However, superior residual signal characteristics have made it very useful at moderately slow scan rates (relative to television) where basic sensitivity is not of primary consideration. Tubes of this general type are also more readily available, and their cost is generally substantially less than that of the custom built slow-scan devices.

MONOLITHIC FERRITE MEMORIES*

By

I. Abeyta,† M. M. Kaufman,† and P. Lawrence‡

Summary—Monolithic arrays of ferrite memory elements are being used to produce low-cost, high-speed memory stacks. These elements are made by the simple batch-fabrication technique of laminating ferrite sheets with embedded conductors. This paper describes the construction, characteristics, and system tests for a basic monolithic memory stack. The system operates in the word-select mode and employs several types of selection matrices. Storage-diode and conventional-diode systems are described.

Fabrication

THE FERRITE wafer is constructed by sandwiching two sets of conductors between very thin sheets of ferrite to form closed-flux-path storage elements. The wafer is just over 1 inch square and less than 6 mils thick. Each set of conductors consists of

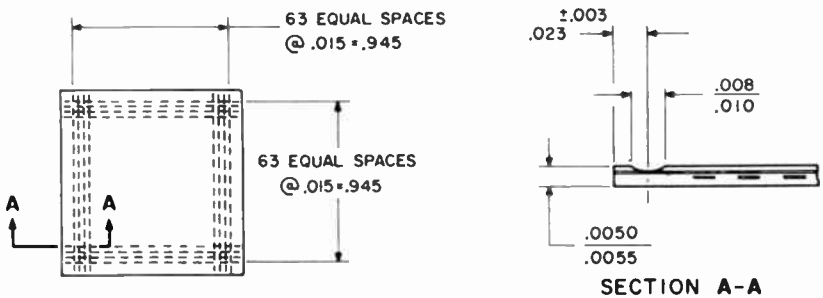

Fig. 1—Monolithic wafer.

64 straight parallel lines in a planar array, with center-to-center separations of 15 mils, as shown in Figure 1. The conductors of one set are placed at right angles to those of the other set. Their vertical separation is less than one mil.

The ferrite sheets are prepared by a technique known as "doctor-blading." In this process, a mixture of ferrite powder (an Fe-Mg-Mn-Zn

* This paper appeared in the *Proceedings of the 1965 Fall Joint Computer Conference*, American Federation of Information Processing Societies, Vol. 27, Part 1.

† RCA Defense Electronic Products, Camden, N.J.

‡ RCA Electronic Components and Devices, Needham, Mass.

composition), vinyl plastic, and plasticizer dispersed in methyl-ethyl-ketone (MEK) is prepared in a ball mill. This slurry is poured onto a glass substrate and drawn to the appropriate thickness by passing a metal blade, called a doctor blade, over the mixture. When the MEK evaporates, a sheet remains in which the ferrite particles are suspended and bound. The density of the sheet is related to the extent of dispersion of the ferrite powder in the slurry, and the binder system plays a very important role in stabilizing the dispersions. The doctor-blading technique enables the forming of ferrite sheets of approximately 50 percent of the maximum possible density, with thicknesses ranging from 0.1 to 20 mils.

The laminated wafer is made using three ferrite sheets. Two of the ferrite sheets have a pattern of 64 lines of metallic powder on one surface. These lines are formed by squeegeeing palladium in paste form through a metal mask onto a glass substrate. The metal mask is removed and the ferrite is then doctor-bladed over the line patterns. The conductor lines obtained are 6 to 7 mils wide, 1 mil thick, and 1.2 inches long.

On the unfired doctor-bladed sheet, the resistance of a line is 225 ohms $\pm$ 10 percent. Measurement of their resistance is used as a quality control check on the metallic paste batches.

In the unfired state, the three ferrite sheets form a wafer 1.2 inches square. The sheets are laminated at an elevated temperature and a pressure of about 10,000 pounds per square inch to form a monolithic body. The firing of these ferrite bodies is divided into two cycles: (1) a binder-burnoff stage and (2) a sinter or densification stage. The binder burnoff cycle is extremely important, since it is here that such mechanical problems as cracking and warping occur. The heating rate must be very slow and the proper atmosphere must be maintained to facilitate binder removal. After completion of this cycle, the laminates can be brought directly to sintering temperature and fired to yield the desired magnetic properties. The proper atmosphere must be maintained during sintering, not only for magnetic considerations, but also to keep the electrical resistivity of the ferrite high so that the ferrite layer between the palladium conductors can function effectively as an insulator.

After sintering, the ends of the palladium conductors are exposed for electrical connection. This is accomplished by using an airbrasive to erode away the ferrite above the conductors. The electrical resistance of the embedded palladium conductors is now 2.5 ohms.

Operation

Integrated ferrite wafers have been developed for linear select

operation. Each wafer has 64 word windings and 64 bit windings. Each bit is composed of the crossover between the word winding and two adjacent digit windings, so that a wafer has 32 bits per word. By connecting bit lines of several wafers in series, a memory with some multiple of 64 words is formed. Similarly, word lengths in multiples of 32 bits are made by adding wafers on the other axis.

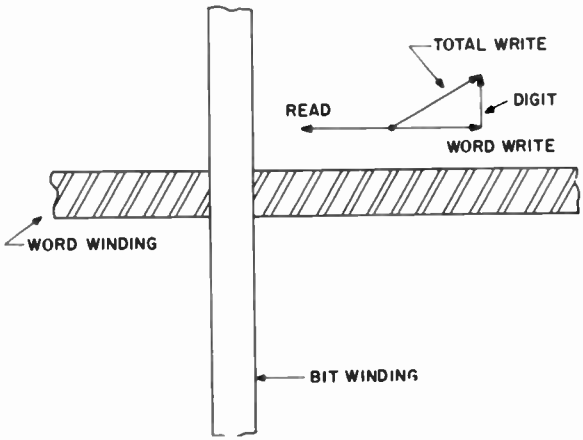

Fig. 2—Memory operation.

Figure 2 illustrates the nature of magnetic flux switching at one crossover point with the application of word and digit pulses. As long as pulses are applied to the word winding only, there is no flux change around the bit windings, so no signal is coupled magnetically from the word to the bit windings. The vector diagram in Figure 2 shows the addition of word write and digit driving fields. The respective components are drawn parallel to the driving currents, thus normal to the planes of their respective driving fields. With coincidence of word and digit currents, flux is switched to the plane to which the vector sum is normal. Upon application of a word read pulse, which is opposite in polarity to the word write pulse, all of the flux is switched to the planes normal to the word winding, with a direction consistent with the vector marked READ. Elimination of the component of flux that had linked the bit winding causes a magnetically coupled signal to appear on the bit winding. Analysis will show that the polarity of this signal depends only upon the polarity of the digit current. For the situation shown, the upper end of the bit winding has a positive voltage with respect to the lower end at read time.

As shown in Figure 3, each pair of bit windings has its own set of digit drivers and a sense amplifier. For those bits of the addressed word that are to store ones, a positive digit current is applied to winding "A" and a negative current to winding "B." At the addressed word, flux switches in accordance with the vector diagram of Figure 2. For those bits that are to store zeros, a positive digit current is applied to winding "B" and a negative current to winding "A." When that

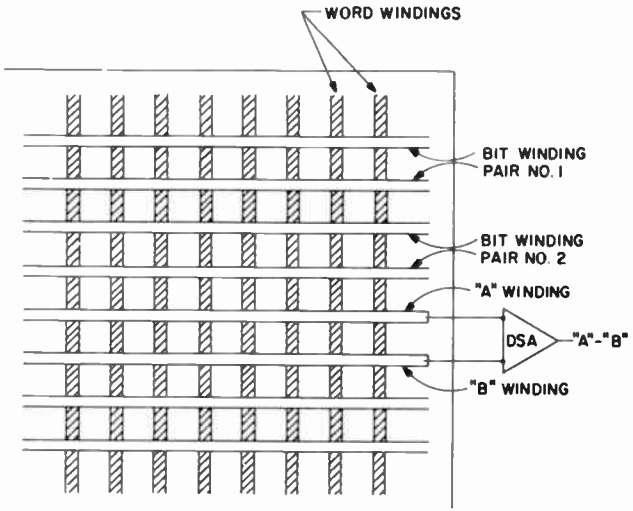

Fig. 3—Laminate winding arrangement.

same word is next addressed with a word read pulse (opposite in polarity to a word write pulse), the vector diagram of Figure 2 shows that the "A" lines of bits storing ones and the "B" lines of bits storing zeros have negative output voltages; conversely, the "B" lines of bits storing ones and "A" lines of bits storing zeros have positive output voltages. Hence, if the difference sense amplifiers yield A-B, the one output signals from the sense amplifiers are negative and the zero outputs are positive. Note that the total signal output of the sense amplifier is proportional to the sum of the absolute values of signals magnetically coupled at the contributing crossover points.

TESTING

Extensive testing of ferrite wafers has been conducted under worst-case disturb conditions. The test pulse pattern applied to the ferrite wafers is shown in Figure 4. Seven pre-disturb pulses and 8 post-disturb pulses are applied to the wafer. Tests made with a greater

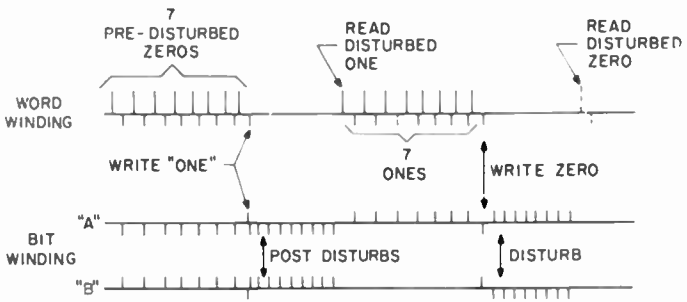

Fig. 4—Disturb test pattern.

number of disturb pulses indicate that 7 pre-disturbs and 8 post-disturbs produce approximately the maximum disturb condition. From this test, a set of curves were plotted (Figures 5 and 6) showing differential sensed peak output voltage as a function of digit current. A desirable range of operating current values has been chosen on the basis of these curves. Disturbed signal output versus digit current, with write current magnitude as a parameter and read current magnitude fixed at 400 milliamperes, is shown in Figure 5. The same curves are plotted in Figure 6, except the read current magnitude is fixed at 550 milliamperes. The typical disturbed output of the ferrite wafer is 45 millivolts. Figures 5 and 6 indicate that increasing the magnitude of the 60-nanosecond-wide read and write current pulses above 400 milliamperes for read and above 100 for write will not increase the disturbed output signals.

The digit current indicated in Figures 5 and 6 has an optimum amplitude of between 30 and 40 milliamperes. It is apparent that the optimum word write and read pulse amplitudes are a function of the pulse widths chosen. A number of operating pulse values are shown in Table I. The bit back-voltage (BBV), which is the word read voltage divided by the number of bits in the word, is also a function of the pulse values and is listed in the table.

Table I—Operating Pulse Values.

Read Current			Write Current		Digits		Typical	
I *ma*	T_r(50%) *nsec*	T_rT_f *nsec*	I *ma*	T_d(50%) *nsec*	I *ma*	T_d(50%) *nsec*	Outputs *mv*	BBV *mv*
400	110	45	100	120	30	200	45	250
400	60	30	150	80	30	100	25	320

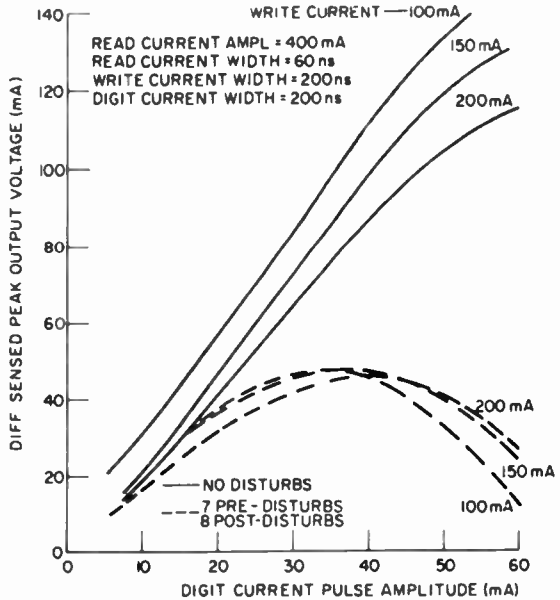

Fig. 5—Signal output versus digit current (read current = 400 milliamperes).

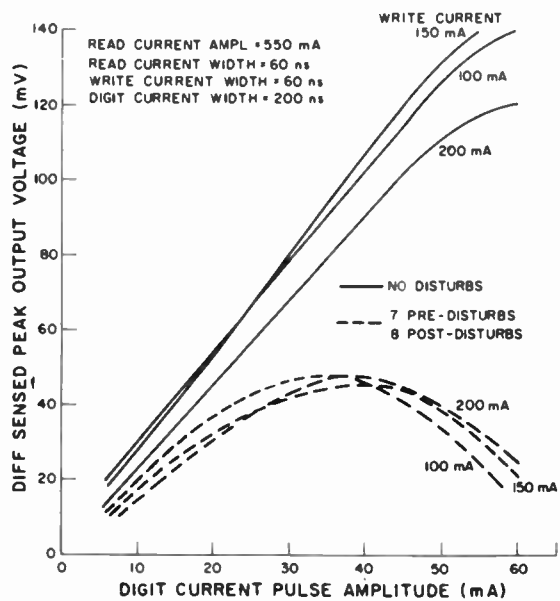

Fig. 6—Signal output versus digit current (read current = 550 milliamperes).

Word	DISTURBED/UNDISTURBED SIGNAL OUT AT DIGIT PAIRS (mv)														
	Pair 1	Pair 2	Pair 3	Pair 4	Pair 5	Pair 6	Pair 7	Pair 8	Pair 9	Pair 10	Pair 11	Pair 12	Pair 13	Pair 14	Pair 15
6	50/68	40/107	45/75	40/72	37/67	36/67	37/67	33/63	33/67	42/65	28/58	25/43	28/60	25/58	32/55
10	60/80	43/107	50/75	43/67	40/70	38/65	33/63	37/65	32/63	47/70	25/58	23/60	27/63	25/62	33/60
14	57/67	53/100	53/67	45/57	40/60	37/52	35/54	37/58	33/57	48/60	27/50	27/54	27/57	32/57	37/58
18	53/75	48/50	52/64	43/60	37/43	33/54	23/55	35/57	28/57	43/62	20/46	25/50	28/54	27/55	33/60
22	55/70	50/92	50/64	42/58	37/53	32/50	30/63	33/57	25/40	42/60	20/50	23/45	27/50	30/53	33/57
26	58/73	50/57	57/63	43/60	35/53	30/48	30/54	35/57	25/57	38/60	23/48	23/47	23/50	30/50	37/42
31	55/67	45/90	47/58	30/60	33/57	27/50	30/54	33/57	27/57	43/63	23/65	30/47	27/50	25/47	33/50
35	53/70	53/90	43/60	33/53	25/50	25/50	22/47	17/50	23/53	33/57	23/48	23/47	27/50	23/47	37/57
39	58/68	50/92	47/65	38/53	32/50	33/50	27/50	28/55	23/50	37/57	23/48	25/45	28/52	30/53	30/52
48	35/80	50/92	47/64	33/55	24/50	22/47	22/50	33/57	28/55	40/57	22/40	23/47	23/37	22/38	17/37
52	42/75	50/92	45/65	35/58	25/50	22/47	22/47	27/53	27/53	47/57	25/50	20/47	28/50	25/42	24/45
55	58/60	40/83	37/55	32/52	27/55	22/50	25/50	30/53	27/57	40/57	28/47	23/50	30/50	33/53	37/57
58	58/75	40/80	40/60	42/67	30/53	20/48	27/52	32/57	32/60	48/63	30/50	28/53	30/50	33/38	27/62
59	57/73	40/77	30/47	42/50	33/57	20/47	30/53	33/55	37/63	50/70	38/60	40/63	37/57	38/57	40/58

Note: Read current = 400 ma, 70 nsec; write current = 120 ma, 70 nsec; digits = 30 ma, 80 nsec.

Fig. 7—Map of signals for a typical wafer. (This map shows typical and extreme signals.)

As an indication of the spread of signal values on a ferrite wafer, a map of disturbed and undisturbed signal values across the wafer is given in Figure 7. All locations of the wafer have been checked and the map in Figure 7 indicates worst-case extremes.

Extensive testing of the transmission-line properties of the wafers using nanosecond-pulse techniques has also been conducted. A summary of the data obtained is shown in Table II. The characteristic

Table II—Digit Transmission Line Properties.

Characteristic Impedance *Best termination*	Pulse Delay *Midpoint to midpoint for 1,024 words*	Pulse Rise Time *256 words*	Attenuation *for pulses wider than rise time, 512 words*
150 ohms	35 nsec	15 nsec	1.1 db

impedance of the transmission line is a function of frequency and coupling to the ground plane; however, the best terminating impedance is given. The attenuation shown in the table for pulses wider than the rise time is essential d-c attenuation, and is associated with the 2.5-ohm line resistance through each wafer.

Stack Construction

Monolithic ferrite stacks are assemblies of modular building blocks. The basic modules are assemblies of two ferrite wafers with diodes and bussing for word selection. There are two kinds of selection diodes available: conventional high-speed and storage types. The module using conventional diodes requires two diodes per word, while the

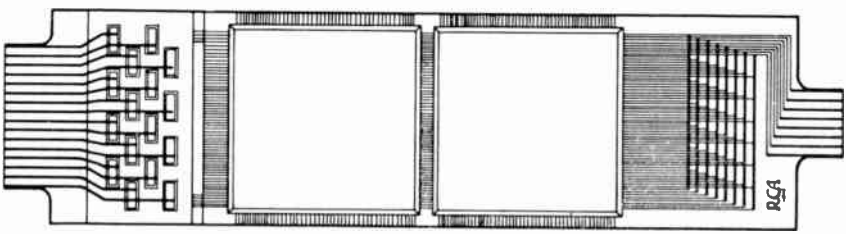

Fig. 8—Construction of the basic integrated ferrite module.

module using storage diodes requires one diode per word. The fabrication of a 1024-word 64-bit stack using 16 modules with conventional diodes is described. A 256-word 64-bit stack was also assembled using 4 modules with storage diodes. Operation and testing of both stacks is also described.

Figure 8 is an illustration of an integrated ferrite module with conventional diodes and Figure 9 is a schematic of this module. For convenience, a 16-word array is shown. The modules actually have 64. One end of each word winding is connected to the anode of one diode and the cathode of another. In the case of diodes whose anodes are connected to word windings, the cathode connections are ganged in groups of eight; where the cathode is connected to a word winding, the anode connections are ganged in groups of eight.

The diode chips have 2 rows of 4 diodes, each on 30-mil centers. Notice that the number of connections required on the diode end of the words has been reduced from 64 to 16. The ends of the word windings on the other side of the module are connected directly together in eight groups of eight words each. Each of these groups has

one word from each of the diode groups. The number of connections to this end of the module is reduced from 64 to 8.

Expansion of the diode selection matrix to arrays of more than 64 words merely requires expanding the sizes and numbers of the groups by connecting corresponding points of different modules together. For example, a 1024-word matrix would have 32 groups of 32 words each, as viewed from either end.

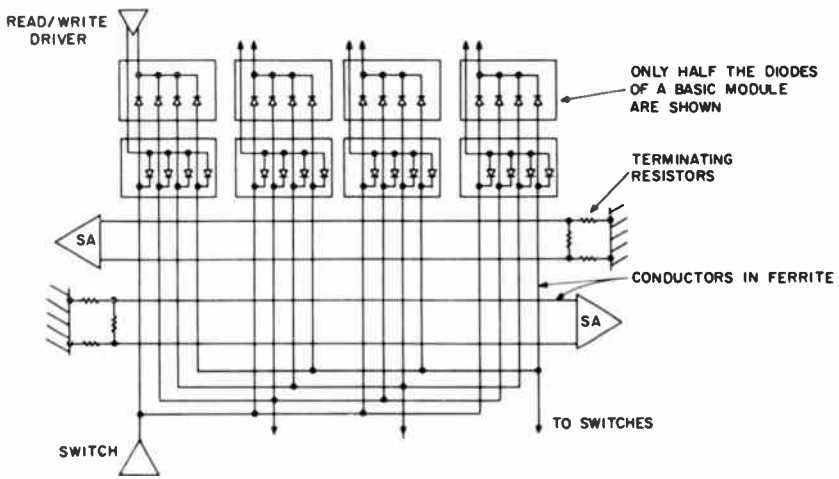

Fig. 9—Schematic of the basic integrated ferrite module.

Line connections on the modules are "fingers" of etched combs leading to the winding ends on the four sides of a wafer. This assembly is soldered to a printed circuit pattern on the module board. After connection, the solid edge of the comb is sheared off. Tabs are left at the edges of the module for connection to the bit windings of another module.

The diode array is assembled as a separate unit and cemented onto the module tabs of previously mounted combs. Connection to the switch buses (bottom of Figure 8) is accomplished with combs appropriately etched from one-ounce beryllium copper. They are raised above the module surfaces as they cross lines that they must not contact. The wafer interconnection combs are etched from one-ounce copper sheets, subsequently plated with an electroless tin coating to facilitate soldering. The module substrate is constructed from 1/16-inch G-10 laminated glass epoxy board. The diode assembly comprises a baseboard with a printed circuit pattern and a spacer board of G-10 material with

the common connections etched. Word drive connections are made with printed circuit plugs having contacts on 50-mil centers.

The conventional diode stack consisting of 1024 words of 64 bits is formed from 2 planes, each containing 512 words (Figure 10). Overall dimensions for the unit, including the sense digit connector boards with terminating resistors, are 14 × 4.5 inches with 0.5-inch spacing between the planes. The sense digit connections are fanned

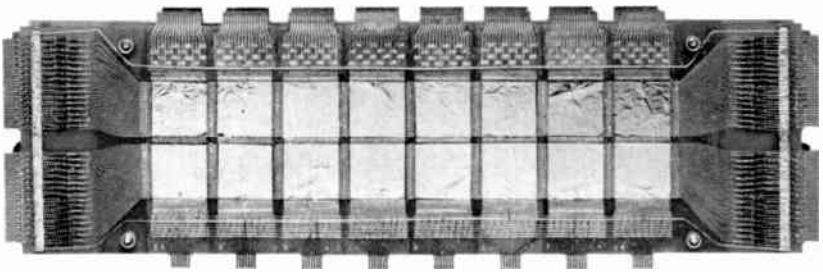

Fig. 10—Typical arrangement of monolithic memory stack.

out from the 15-mil centers to suitable plug connections on 50-mil centers. Module boards are cemented onto a backboard and interconnections between the modules are made by soldering. Bussing between planes is accomplished by soldering #30 wire between corresponding bit windings of the two planes.

Memory System Using Conventional Diodes

Selection Matrix and Digit Drive

This section describes the system design and operational details of the 1024-word, 64-bit memory. The word driving scheme is illustrated by the 4 × 4 diode matrix of Figure 11. The physical dimensions and geometry of the matrix diodes have already been given.

These diodes have the following typical characteristics:

C_0 (function capacitance at zero bias) = 4 picofarads

V (at I = 400 ma) = 1.3-1.8 volts

V_R (at 10μa) = 60 volts

T_r (reverse recovery time) = 15 nanoseconds

Under quiescent conditions, the matrix diodes are back-biased by a positive voltage applied at the write driver, a negative voltage at

the read driver, and ground at the read/write switch. The read/write selection sequence is executed in the following manner:

1. A read command pulse turns on the selected read switch, driving the 32 words selected by the switch to a positive voltage, thus removing the back bias from 32 read diodes.
2. Sometime later, the read driver is turned on, forward-biasing one read diode on the selected word, while the drive line moves toward

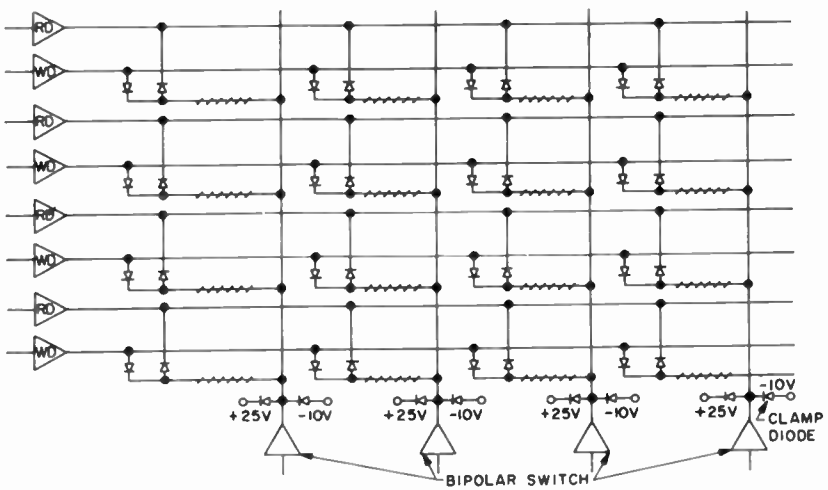

Fig. 11—Schematic of the driving and matrix scheme for the two-diode-per-word laminated ferrite memory.

ground potential from a current source to complete the read operation.

3. Similarly, during the write part of the cycle a write command pulse turns on the write switch, driving the selected set of words negative.
4. The write driver is then turned on, driving the write diode on the selected word toward ground from a current source and thus enabling write current to flow.

All the drivers and switches of the word system are compatible at their inputs with the logic levels of the current steering integrated logic gates used throughout the system.

The parallel capacitance of the 32 word lines connected to each switch is about 1600 picofarads. The read channel of the switch supplies 1 ampere of current so that it can charge this capacitance to +25 volts in about 40 nanoseconds. The write channel of the switch

supplies about 500 milliamperes to complete the transition from +25 volts for read to −10 volts for write in about 100 nanoseconds.

As seen in Figure 11, there are two clamp diodes at the output of each switch, one to +25 volts and the other to −10 volts. Physically located at the stack, their purpose is to provide a sink for the switch current and thus to maintain a low impedance at the memory stack during the read and write pulses despite the cables needed to interconnect the switch lines in the stack with the circuit boards. This action helps to clean up waveforms and to reduce noise.

The digit drivers are bipolar. They store a one by delivering a positive pulse into one line of a digit pair and a negative pulse into the other. A zero is stored by reversing these two pulse polarities. The digit driver outputs are voltage sources during the digit pulse, the amplitude of the digit current being controlled by the voltage and the termination resistors. The driver inputs have logic gates that are primed by the information register and activated by the digit timing pulse.

The sense amplifiers are constructed by cascading two current-steering logic gates and a-c coupling at the output of the second gate to the memory register. Strobing is accomplished at the input to the second gate. Power-supply levels for the gates are raised to prevent gate saturation during the digit pulse. A positive pulse can appear at the sense output only during the strobe, and only if a one is sensed.

Performance Tests

The test vehicle used to check the performance of the conventional diode memory consists of (1) the timing and control generator, (2) a word system, and (3) a digit system. The timing and control generator supplies all timing and control pulses. The word system supplies the proper switch voltages and read/write currents at the command of the timing generator. The digit sense system performs the dual function of sensing stored information and writing back into the memory.

The test vehicle has four different types of logic components, providing address scan, disturb patterns, and error checks. These are:

1. Integrated current-steering gates of the emitter-coupled current-steered logic (ECCSL) type.
2. Integrated current-steering flip-flops.
3. One-shots with variable delay, made by adding a few external components to integrated current-steering gates.
4. A free-running multivibrator with variable frequency, also made from an integrated current-steering gate.

These four devices have proven to be very stable and reliable and have made the test unit highly flexible and permit high packing density.

The test system can be set to pre-disturb a word up to 35 times when running at 2 megacycles per second. The pre-disturbs end when the timing generator causes the digit drivers to change write information for one write time. The timing generation then causes up to 70 digit disturbs to be generated. At the end of the digit disturb period,

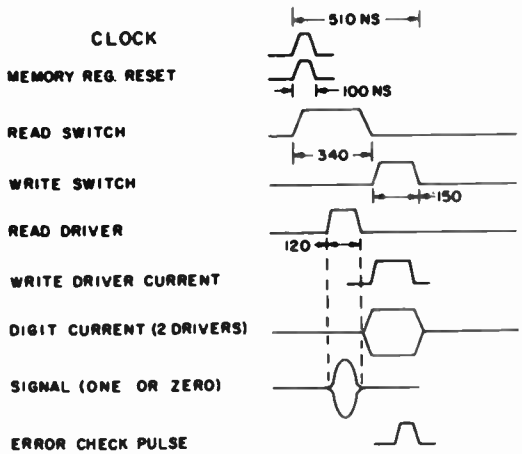

Fig. 12—Timing diagram for conventional diode test vehicle.

the last written information is read out. Then this entire pattern is complemented. Finally, the address is changed to a new word. The disturb pattern is then repeated at the new word, etc. Information from one bit to the next along a word can be complemented by a mechanical switch in the information register. The timing diagram for the test vehicle is shown in Figure 12.

The read switch is turned on approximately 150 nanoseconds ahead of the read driver to allow the noise transient coupled into the digit lines to decay to a level much less than the signal.

The noise is coupled into the stack through all of the words common to the selected switch. The magnitude of this noise depends on the number of words in the stack. For a switch driving 32 lines, the common-mode noise injected into the digit lines is approximately 1 volt. However, as has already been pointed out, sensing is performed differentially; therefore, large common-mode noise will not be a problem provided the digit pair balance in the stack is sufficient. This balance minimizes conversion of common-mode noise to difference mode.

The conversion to difference mode for this stack was approximately 1.5 percent, or 15 millivolts. With ideally terminated digit lines, a read operation could immediately follow the end of the digit pulse. However, it has been found that a waiting period 6 to 9 times the delay on the digit line is required.

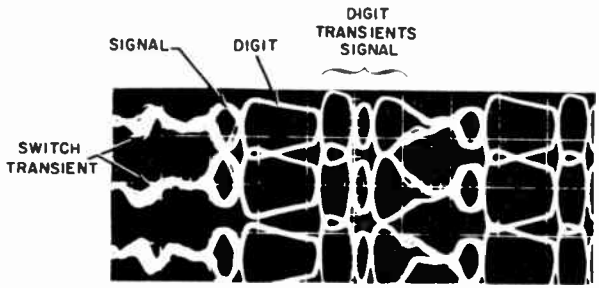

(a)

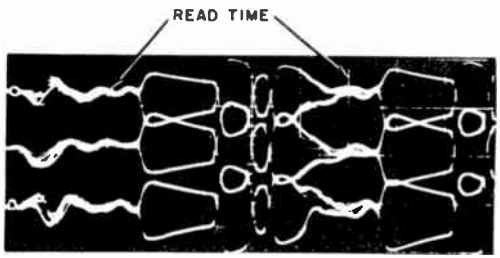

(b)

Fig. 13—Comparison of the signal and total noise present at read time: (a) 64 signals superimposed at each of 3 digit locations; (b) same as above, except that write drivers are disconnected to show the noise present at read time.

In addition to the switch and digit noise, which are not time-coincident with the signal, there are sources of noise that are coincident with the signal. One of these sources is associated with the fact that the impedance between the stack and the matrix switch ground cannot be made negligibly small. The problem is minimized by adding clamps at each switch line. Reference to Figure 11 shows the location of these diodes on the stack. The second source of time-coincident noise is associated with the removal of back bias on the matrix diodes connected to the selected driver. Other things being equal, this noise can only be eliminated by the inherent common-mode rejection characteristics of the stack.

Waveforms of the tests on this 1024-word 64-bit stack operating at a 500-nanosecond cycle time are shown in Figures 13 and 14.

Figure 13(a) shows fully disturbed stack output signals with digit transients. Each of the three traces represents the outputs of a bit from 64 words superimposed. The first transient at the left is caused by read switch turn-on which lasts 150 nanoseconds. Following this are signal outputs. The positive signals are ones and the negative signals are zeros. These last for about 70 nanoseconds. The remaining time in the cycle is occupied by the digit transient.

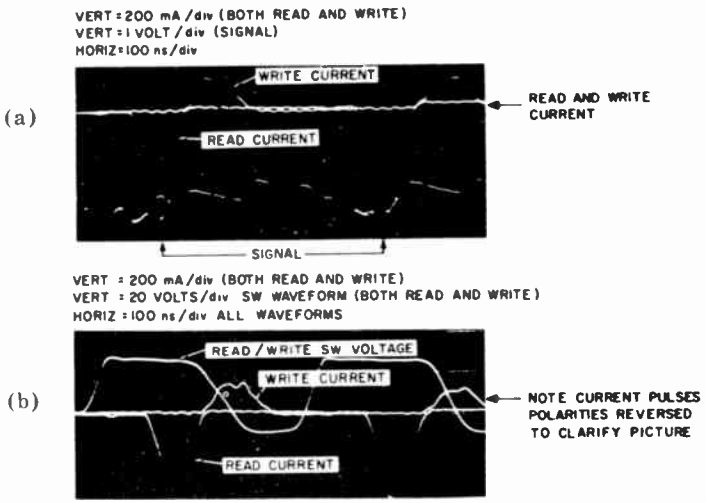

Fig. 14—Typical time relationships: (a) time relationships between read/write current and signal; (b) time relationships between read/write driver circuits and read/write switch voltages.

Figure 13(b) shows the stack output with the drive conditions the same as those above except for removal of word write current. The low noise level at signal time indicates good sense pair balance.

In Figure 14(a), typical read and write currents are shown at a point between the diode matrix and the drivers. In addition, typical signals are shown in coincidence with the read current. Again, these are disturbed signals. In Figure 14(b), read and write currents as well as switch voltages are shown.

Memory System Using Storage Diode

Selection Matrix

The storage-diode selection matrix uses one diode per word. The storage diode, because of its resistivity profile, has long-term minority

carrier storage and allows construction of a one-diode selection switch that delivers bipolar currents. Storage diodes also exhibit the desirable property that in the absence of minority-carrier storage, a high-resistance (megohms), low-capacitance (a few picofarads) characteristic is maintained in the reverse direction. This ensures that below the half-select matrix voltage, the properties of a storage diode will be identical to those of a high-speed diode.

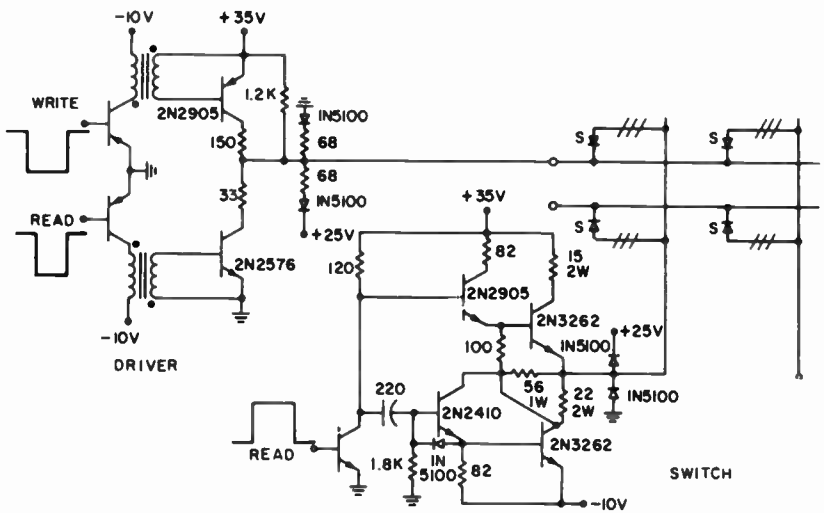

Fig. 15—Storage-diode selection matrix.

A schematic diagram of a 4-word portion of the 256-word matrix that was built and tested is shown in Figure 15. Half-select operation of the matrix is identical to the half-select operation of a conventional diode matrix, all diodes appearing as approximately 2-picofarad capacitors. Activation of a driver alone or a switch alone does not forward-bias any diode in the matrix.

Activation of a switch followed by a driver drives the selected diode sufficiently beyond its voltage gap to permit the flow of the required read current. The storage diodes in the matrix have minority-carrier lifetimes of approximately 170 nanoseconds. Storage-diode lifetime is the parameter that defines the diode's stored-charge recombination rate[2] and, therefore, is directly proportional to the maximum charge the diode can store. The 170-nanosecond lifetime allows the diode to return 20 percent of the charge flowing into it during the read pulse as a write pulse. The write pulse is generated when the read channel of both the switch and the driver are deactivated and the write channel

is activated. The write channel of the switch is activated during the fall time of the read clock pulse. The previously selected storage diode is then forced by the voltage that eventually reverse-biases the diode to give up its stored minority carriers as write current. The write current terminates when the charge in the diode is depleted and the fall time of the write current is approximately equal to the snap-off time of the diode.

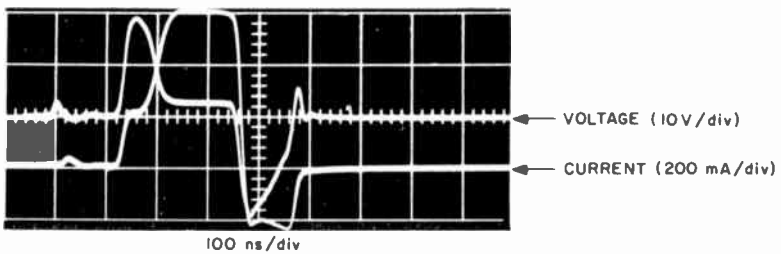

Fig. 16—Read/write current and word back-voltage generated for 170-nanosecond lifetime diode.

The diodes used in this matrix are fabricated in integrated strips of eight diodes each. They have the following typical characteristics:

$C_0 = 2$ picofarads

$V +$ (at $I_f = 400$ ma) $= 1.2$ volts

I_R (at $V = 100$ v) $= 1$ microampere

B_v (breakdown $I_R = 10$ μa) $= 150$ volts

Transition time (snap-off time) $= 4$ nanoseconds

Lifetime $= 170$ nanoseconds

The read write current and the word back voltage generated in the matrix for the 170-nanosecond lifetime diode are shown in Figure 16. The read-current peak magnitude is 600 milliamperes with a 300-nanosecond base width; write-current peak magnitude is 200 milliamperes with a 100-nanosecond base width. The word current has a "front porch" caused by the voltage associated with switching the ferrite. Comparison of the back voltage waveform across the word when all the ferrite is switched with the back voltage under the above condition indicates that 80 percent of the ferrite is switching. The percentage of the ferrite that switches is a function of the write-current pulse width and amplitude; therefore the duration of the read-current front porch is also a function of the write-current pulse width. The front porch limits the amount of read charge going into the diode

and reduces the percentage change of write-current pulse width as a function of storage-diode lifetime. A 30 percent change in storage-diode lifetime produces only a 20 percent change in write-current pulse width.

Operation

A block diagram of the 256-word 64-bit test vehicle is shown in Figure 17. The memory was addressed by scanning the 256 words

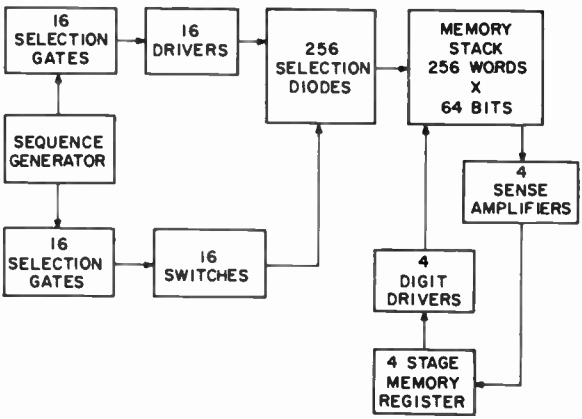

Fig. 17—Block diagram of test vehicle for storage-diode matrix.

sequentially. There were 16 switches and 16 drivers in the system and all 256 words were addressed. However, there were only 4 sense amplifiers and 4 digit drivers in the system, operating only 4 out of 64 digit locations at one time. The circuits were built on plug-ins and placed in a rack, as shown in Figure 18.

A timing diagram is shown in Figure 19. The switch is initiated 100 nanoseconds before the driver to isolate the switch noise coupled into the matrix when the half-selected word lines are driven to 25 volts. The switch rise time is 50 nanoseconds for driving the 256-word stack. When driving a stack of 4096 words (2000-picofarad line capacitance) the rise time is 100 nanoseconds. The word-driver rise time is only 25 nanoseconds. The maximum selection-line capacitance it drives, considering a 4096-word stack, is 128 picofarads. The digit current is initiated at the end of the read current and has a 30-milliampere peak magnitude. It is 200 nanoseconds wide at the base. The digit lines are driven in a push-pull mode, as shown in Figure 20. The lines are terminated in their characteristic impedances of approximately 120 ohms.

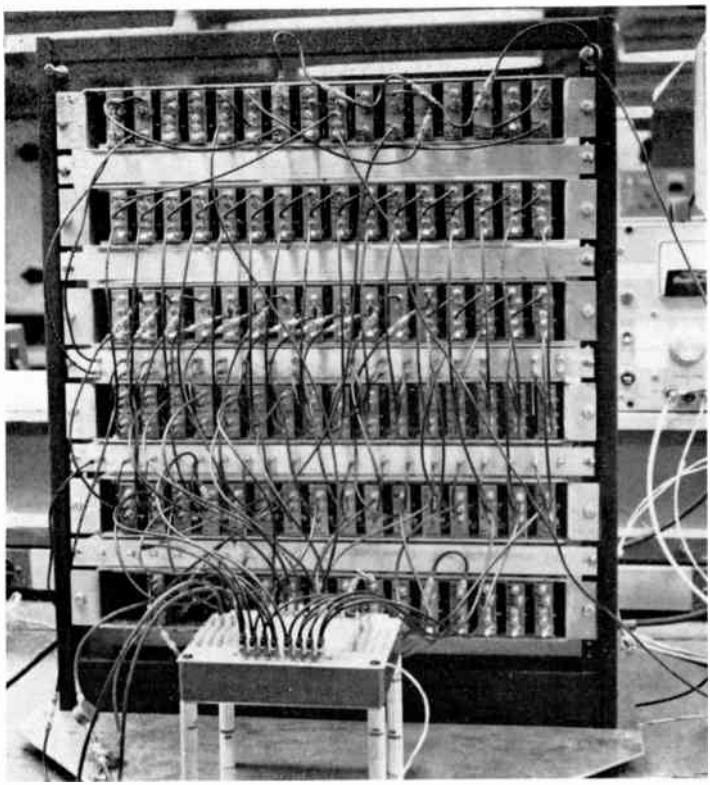

Fig. 18—Construction of test vehicle for storage-diode matrix.

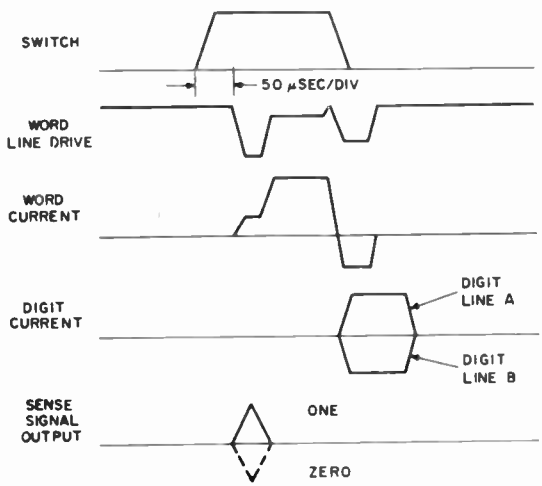

Fig. 19—Timing diagram for storage-diode test vehicle.

THE ACOUSTOELECTRIC EFFECTS AND THE ENERGY LOSSES BY HOT ELECTRONS—PART I*

By

Albert Rose

RCA Laboratories
Princeton, N. J.

Editor's Note: This is the first part of a several part paper. Subsequent parts will appear in future issues of RCA Review.

In Part I the acoustoelectric effects for the several types of sound waves are obtained. The formalism used is the rate of exchange of energy between two coupled systems in relative motion. This formalism is shown to be consistent with an energy-well type of argument. The characteristic parameter in the final expressions is the ratio of electrical to total energy for the several types of sound waves.

In Part II the rates of loss of energy by free carriers is computed for loss to phonons, plasmons, electronic excitations and Cerenkov radiation. The formalism used is a classical energy-well argument upon which the quantum conditions are imposed as constraints. The characteristic parameter for loss to phonons is the ratio of electrical to total energy for the various forms of radiation.

In subsequent parts, the rates of energy loss of Part II are used to compute the mobilities of carriers in thermal equilibrium with the lattice, the mobilities of carriers whose mean energy is in excess of the temperature of the lattice, and the dependence of this mean energy on applied field. Finally, the conditions for dielectric breakdown via impact ionization by hot carriers are analyzed.

PREFACE

The content of this discussion emerged from an attempt to get a physical understanding of two areas of electron–phonon interactions — the low-field acoustoelectric current–voltage saturation first observed

* This work was supported in part by the U.S. Army Research Office–Durham, Durham, North Carolina under Contract No. DA-31-124-ARO (D)-84.

by R. W. Smith,[1] and the energy-loss mechanisms for hot electrons. The latter was actually to be a first step in interpreting the events leading to dielectric breakdown. It rapidly became clear that there was a closer connection between these two sets of phenomena than I had anticipated. In fact, this discussion argues that one can interpret a variety of phenomena, that are normally treated separately in the literature, by a single concept — that of an energy well — and by a single parameter — the ratio of electrical to total energy of an acoustic wave.

Throughout the course of this work I have had the generous guidance of a number of my colleagues in the extensive literature on electron–phonon interactions, and the concepts of polarons and plasmons. I have had, in particular, a steady exchange of ideas with M. A. Lampert, G. D. Whitfield (Pennsylvania State University), and R. H. Parmenter. Their contributions to the content of this work have been both substantial and substantive. In addition, I have profited on numerous occasions from discussions with L. R. Friedman, D. O. North, J. J. Quinn, and A. Rothwarf.

1. Introduction

AN ELECTRON in vacuum has a coulomb field extending from a radius at least as small as 10^{-12} cm to infinity. The energy density in the field is $\mathcal{E}_r^2/(8\pi)$, where $\mathcal{E}_r = e/r^2$. When the electron is plunged into a material medium, its electric field is reduced by the polarization of the medium to a value $\mathcal{E}_r/K$, where K is the relative dielectric constant of the medium. The polarization extends from some radius not smaller than one angstrom, owing to the atomic nature of any medium, toward infinity. The energy density in the reduced coulomb field in the medium is now $\mathcal{E}_r^2/(8\pi K)$. In brief, most of the coulomb energy of the electron* beyond some small radius has been polarized out. The potential energy of the electron has been reduced by the difference between $\mathcal{E}_r^2/(8\pi)$ and $\mathcal{E}_r^2/(8\pi K)$ integrated over the appropriate volume. The reduction in potential energy can be represented as an energy-well that the electron "digs" for itself in the medium.

If we now move the electron slowly through the medium, the polar-

[1] R. W. Smith, "Current Saturation in Piezoelectric Semiconductors," *Phys. Rev. Letters*, Vol. 9, p. 87, Aug. 1, 1962.

* The term "electron" is used for definiteness. The arguments apply equally to holes.

ization will follow the electron with negligible dissipation. As we speed up the motion of the electron, various components of the polarization will progressively be left behind as a "polarization wake" of the electron. The polarization arising from displacement of the atoms or ions will be the first to be abandoned owing to the relatively sluggish motion of atoms. The polarization arising from displacement of the electron clouds of the atoms will continue to follow the moving electron without significant dissipation until the electron has a velocity of several volts, at which time it too will tend to be left behind in the polarization wake of the moving electron. The polarization wake of the moving electron constitutes energy radiated by the electron in the form of phonons (i.e., lattice vibrations), plasmons (i.e., vibrations of the electron clouds), and finally, at velocities exceeding the velocity of light in the medium, photons (i.e., the electromagnetic radiation known as Cerenkov radiation). The energy-well that the "stationary" electron digs for itself by atomic displacements in the medium is the polaron well or polaron energy. For a medium with a single fixed frequency ω, the polaron well is a measure of the maximum rate of loss of energy by a moving electron. At sufficiently high velocities, the energy of the well left behind in unit *path length* by the moving electron decreases as the reciprocal of the square of the electron velocity. Hence the time rate of energy loss decreases as v^{-1}.

There is, of course, an extensive literature dealing with the excitation of phonons, plasmons, and photons by moving electrons. The treatments are, for the most part, quantum mechanical computations of the probability that an electron will make a transition between two states (of the electron) under the perturbing influence of thermal phonons, plasmons, or photons and their zero-point vibrations. The treatments, by their nature, must depart from elementary or pictorial concepts once the problem is formulated in terms of an integral over all of the possible quantum transitions.

Our purpose in this discussion is to try to match the formal and rigorous results of the quantum mechanical treatments by classical arguments upon which the constraints of the quantum nature of radiation and the wave nature of the electron are imposed in a way that retains the pictorial virtues of the classical concepts. It need scarcely be argued that such concepts are the working tools of most applied physicists. These concepts are especially helpful when one is faced with the results of a particular experiment, and sets about to inquire which of the manifold electron interactions is playing a significant role.

We will not be concerned in this discussion with numerical rigor and will be content in the interests of simplicity to match the more formal developments within a numerical factor of order unity. We *will* be concerned with *conceptual* rigor. Whether or not this is achieved, we hope that the examination of a collection of related phenomena in physical terms may facilitate the posing of conceptual questions by the non-theorist as well as by the theorist.

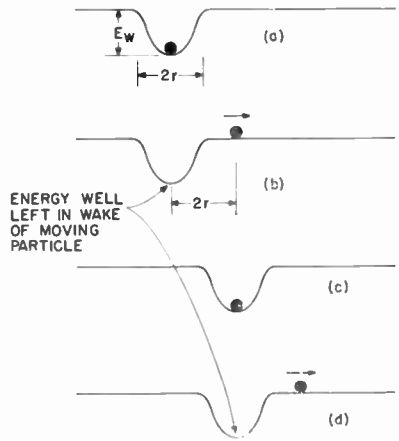

Fig. 1—Schematic steps showing maximum time rate of energy loss $(1/2)E_w\omega$ for a particle in an energy well.

2. Central Concept

The concept that underlies most of our discussion has already been referred to in the introduction. It is the idea that an electron digs an energy well by polarizing the surrounding material. When the electron moves, it tends to leave its well behind as a wake of radiated energy. We can make this concept more quantitative by a relatively simple estimate of an upper limit to the rate of loss of energy by a moving electron.

Let a "stationary" electron dig a well whose depth is E_w (see Figure 1). We put quotes on the term stationary because this classical concept must be reconciled with the uncertainty relation that sets limits on how precisely the position and momentum of an electron can be simultaneously specified. This comes up in later discussion. For the present we can imagine the electron sinking energetically into the medium much as a metal ball sinks into a rubber membrane. We specify the energy depth of the well by E_w, its physical extent by r, and the relaxation time of the medium by ω^{-1}. The relaxation time

is derived, for example, from the ability of the medium to support a wave motion of angular frequency ω, or from the time required by a conductive medium to relax an electric field. It is the time required by the electron to dig its well by displacing the medium or by provoking currents that relax its electric field.

If we suddenly extract the electron from its well, we will leave behind an energy of polarization equal to the energy of the well. This operation has a familiar parallel in the physics of capacitors. Consider a pair of capacitor plates having a fixed charge. The charge on the capacitor plates is the analog of the electron in vacuum. We insert a material of high dielectric constant between the plates so that the energy of the capacitor is reduced from $(\mathcal{E}^2/8\pi)(Ad)$ to $(\mathcal{E}^2/8\pi K)(Ad)$. The product Ad is the volume of space between the capacitor plates. The insertion of the dielectric corresponds to plunging the electron from vacuum into a solid dielectric. Finally, we suddenly remove the dielectric from between the plates in a time short compared with any relaxation of charge in the dielectric. At the moment of removing the dielectric the increase of electrical energy of the dielectric owing to its polarization-induced surface charges will be $[\mathcal{E}^2/8\pi - \mathcal{E}^2/8\pi K]\,Ad$, or just the amount of energy by which the energy of the capacitor had been initially reduced by insertion of the dielectric. This last operation—removal of the dielectric—corresponds to suddenly separating the electron from its potential well.

Having suddenly extracted the electron from its well, we can locate it a distance $2r$, or one well-diameter removed, where it can proceed to dig a new well. The time required will, by our definitions, be ω^{-1}. After this time, we again displace the electron suddenly to a distance $2r$ removed. We make ω such displacements per second and at each displacement we leave behind (or radiate) an energy E_w. Hence, by this step-wise motion, we obtain an upper limit to the rate of loss of energy

$$\left.\frac{dE}{dt}\right|_{\max} = E_w\omega. \tag{1}$$

This step-wise motion can obviously be replaced by a continuous motion such that the electron traverses the well diameter $2r$ in the relaxation time ω^{-1}. The effect on Equation (1) will be to multiply it by a factor of order 1/2, since the continuous as opposed to the step-wise motion will tend to leave perhaps half, but not all, of the energy of the well behind.

We anticipate parts of our later discussion by writing down here

the maximum rate of loss of energy by an electron to polar optical phonons, and the maximum rate of loss of energy (per unit volume) by a sound wave* in a conducting medium.

Emission of polar optical phonons:

$$\left.\frac{dE}{dt}\right|_{\max} = (\alpha_p \hbar\omega)\,\omega \tag{2}$$

where $\alpha_p \hbar\omega$ is the energy of a polaron, that is, the energy well† dug by a "stationary" electron in the polar optical modes of a crystal, and ω is the frequency of the optical modes—taken here to be a constant. α_p is the coupling constant in polaron theory. The use of the energy well is consistent with the operation, previously referred to, of integrating $\mathcal{E}_r^2 - (\mathcal{E}_r^2/K)$ over the appropriate volume.

Attenuation of sound waves:

$$\left.\frac{dE}{dt}\right|_{\max} = \frac{1}{2} E_e \omega \tag{3}$$

where E_e is the density of electrical energy in the sound wave and ω is its frequency.

We note that Equation (2) for emission of polar optical phonons immediately matches Equation (1). In the case of Equation (3), we must recognize that E_e is physically or conceptually the energy well to be associated with an acoustic wave. That is to say, if we begin with an electrical energy density E_e in the sound wave we can reduce this energy to near zero by choosing the conductivity of the medium to have a dielectric relaxation time

$$\tau_r = \frac{K}{4\pi\sigma} = \omega^{-1}. \tag{4}$$

The electric field is then substantially polarized out everywhere. This operation is comparable to letting the electric field energy of an electron beyond a certain radius be polarized out by the medium. Hence, Equation (3) also matches Equation (1). Since Equation (3) is couched in

* The term "sound wave" is used to denote the traveling mode of lattice vibrations including both the acoustic and optical branches.

† The energy well is actually the polarization energy minus the kinetic energy of localization of an electron. This difference is about half the polarization energy itself.

terms of the electrical energy density of the sound wave, we will need to know the ratio of electrical to total energy in order to compute the attenuation of the sound wave itself, whose energy is predominantly elastic.

This ratio of electrical to total energy will play a central role in comparing the rates of loss of energy due to various phenomena. In fact, we list in Tables I and II (see pages 131 and 132) the several rates of loss of energy to be discussed in order to emphasize at the outset certain common features. These rates of loss of energy are either reproduced from the literature or are formal algebraic derivatives of the results as given in the literature. The common thread in all of these expressions is the ratio of electrical to total energy of the various wave phenomena considered. Tables I and II are useful in themselves as a convenient, common formalism for comparing rates of loss of energy due to the various phenomena. The tables also strongly suggest that there is a common set of physical concepts underlying the several phenomena. Our primary purpose is to explore these concepts.

To go beyond the central concept expressed in Equation (1), we need to compute the rates of energy loss for arbitrary velocities of the electrons relative to the wave phenomena with which they interact.

We begin with the several acoustoelectric effects because these phenomena are, for the most part, classical and present no conceptual difficulties. By introducing the ratio of electrical to total energy in a straightforward manner, the acoustoelectric effects offer an introduction to the phonon losses by individual electrons for which the same ratios of electrical to total energies appear as key parameters. As mentioned earlier, the relaxation by conduction currents of the electric field associated with the sound wave plays the same physical role as the relaxation by polarization of the electric field of individual electrons.

3. Acoustoelectric Effects

When a sound wave is propagated in a conducting crystal, the wave is attenuated owing to the I^2R losses incurred by the electric field associated with the wave. Parmenter[2] was the first to point out that the attenuation of the wave by free carriers should give rise to a force on the carriers tending to drag them in the direction of the wave. The result is a measurable acoustoelectric current or voltage. Weinreich[3]

[2] R. H. Parmenter, "The Acousto-Electric Effect," *Phys. Rev.*, Vol. 89, p. 990, March 1, 1953.

[3] G. Weinreich, "Ultrasonic Attenuation by Free Carriers in Germanium," *Phys. Rev.*, Vol. 107, p. 317, July 1, 1957.

re-examined the problem and gave a simple physical argument for expecting an acoustoelectric current to accompany the attenuation of the wave. The argument was that the work done on the wave represented a power that must be expressible as a force times a velocity. The velocity in this case was taken to be the wave velocity. The force must be the force of the wave on the free carriers and, hence, must reveal itself as a current or voltage.

Hutson and White[4] analyzed the attenuation of acoustic waves in piezoelectric materials where relatively strong electric fields accompany the wave motion. In a separate publication Hutson, McFee, and White[5] recognized and demonstrated that the attenuation of an acoustic wave could be symmetrically converted to an amplification of the wave by causing the electrons to drift faster than the wave and in the same direction. Hutson's analysis was a small-signal analysis that combined Maxwell's equations, the piezoelectric equations, and carrier diffusion effects into a single analytic solution.

Gunn[6] carried out an independent analysis of the amplification of polar optical sound waves by a drifting stream of carriers. Gunn's result matches that of Hutson when the ratio of electrical to total energy appropriate to polar optical waves is used to replace that appropriate to piezoelectric waves. Woodruff[7] carried out a more detailed analysis of the same problem.

A number of other somewhat more formal and more general analyses of the amplification of sound waves by Spector[8] and by Eckstein[9] have appeared.

We will first derive Hutson's result, ignoring diffusion, by making use of a relatively simple mechanical argument. The effect of diffusion will then be added by physical reasoning.

---

[4] A. R. Hutson and D. L. White, "Elastic Wave Propagation in Piezoelectric Semiconductors," *Jour. Appl. Phys.*, Vol. 33, p. 40, Jan. 1962.

[5] A. R. Hutson, J. H. McFee, and D. L. White, "Ultrasonic Amplification in CdS," *Phys. Rev. Letters*, Vol. 7, p. 237, Sept. 15, 1961.

[6] J. B. Gunn, "Travelling-Wave Interaction between the Optical Modes of a Polar Lattice and a Stream of Charge Carriers," *Physics Letters*, Vol. 4, p. 194, 1 April 1963.

[7] T. O. Woodruff, "Interaction of Waves of Current and Polarization," *Phys. Rev.*, Vol. 132, p. 679, 15 Oct. 1963.

[8] H. N. Spector, "Amplification of Acoustic Waves through Interaction with Conduction Electrons," *Phys. Rev.*, Vol. 127, p. 1084, Aug. 15, 1962; "Ultrasonic Amplification in Extrinsic Semiconductors," Vol. 130, p. 910, 1 May 1963; "Quantum Effects in the Amplification of Sound in the Presence of a Magnetic Field," Vol. 132, p. 522, 15 Oct. 1963.

[9] S. Eckstein, "Resonant Amplification of Sound by Conduction Electrons," *Phys. Rev.*, Vol. 131, p. 1087, 1 Aug. 1963.

3-A—Energy Exchange between Moving Systems

Consider two systems A and B in relative motion and let there be a force of interaction F between the systems. For definiteness, one may imagine (see Figure 2) a block A sliding on a block B and subject to a force of friction F. For convenience, let B rest (or slide) on a frictionless surface.

We move A at a constant velocity v_A such that it slides on B and exerts a force F on B. In this example, B will be uniformly accelerated.

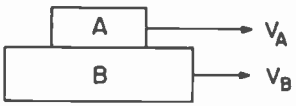

Fig. 2—Schematic diagram of body A sliding on body B.

However, we examine the power delivered to A and B at some particular velocity of B, namely $v_B < v_A$. We can write by inspection:

$$\left.\begin{array}{l}\text{power expended on A}\\ \text{by agency that moves A}\end{array}\right] \equiv P_A = Fv_A, \tag{5}$$

$$\left.\begin{array}{l}\text{power expended on B}\\ \text{to increase momentum of B}\end{array}\right] \equiv P_B = Fv_B, \tag{6}$$

$$\left.\begin{array}{l}\text{power dissipated into}\\ \text{"zero momentum" processes}\end{array}\right] \equiv P_D = F(v_A - v_B). \tag{7}$$

The velocities v_A and v_B are measured relative to a stationary observer. Since A by assumption is not accelerated, the power expended on A must be passed on *in toto* to increasing the momentum of B and to "dissipative" processes. This equality is evident by inspection of Equations (5)-(7).

The meaning of Equation (7) is perhaps not so obvious and needs a word of explanation. We have stated that the power input P_A to A must be passed on *in toto* to increasing the momentum of B and to other processes. Since P_B, the power used in increasing the momentum of B, is clearly less than P_A, there must, by conservation of energy, be a residual power, P_D, to make up the difference. By Newton's laws, this power cannot go to increasing the net momentum of the system and hence must go into processes whose net momentum is zero. Such processes in the case of a block A sliding on a block B are clearly the frictional heating of A and B at their surfaces. In a more general case, P_D can be associated with microscopic parts of B that are scat-

tered symmetrically to either side of the line of flight of A. The sidewise momenta of such parts would then add up to zero, but their energies would of course be finite. A mechanical illustration of this is the splitting by an axe of a block of wood hung from a string. There will then be two parts to the energy of the pieces of wood—that associated with the net forward momentum of the pieces along the line of flight of the axe and that associated with the lateral components of velocity of the pieces whose momenta sum to zero.

An illustration more pertinent to our discussion is the Cerenkov radiation emitted by a fast electron. The angle at which the radiation is emitted is readily computed to be the angle that satisfies Equations (6) and (7). We will return to this later in the discussion.

Equations (5)-(7) are quite elementary. They nevertheless permit a radical simplification in the computation of the gain or attenuation of sound waves by a drifting stream of carriers. In the acoustic problem we are given the velocity v_d corresponding to the drift velocity of the carriers, and we are given also the velocity v_p corresponding to the phase velocity of the sound wave. What we need to know in order to compute P_p, the power going into the acoustic wave, is the force F. But from Equation (7) we can compute F providing we have a means of computing P_D, the dissipative power. This turns out, as we shall show shortly, to be an elementary computation for the relative motion of sound waves and a drifting stream of carriers. Hence, we have a simple formalism for computing the rate of doing work (Equation (6)) on the sound wave.

3-B—Amplification and Attenuation of Sound Waves

Consider an acoustic wave having associated with it an electric field $\mathcal{E}$ that undergoes the same sinusoidal variation in time and space as does the sound wave. If the sound wave is immersed in a medium of free carriers and if the carriers are drifting with a velocity equal to the phase velocity of the wave, there will be no steady exchange of energy between the wave and the carriers. The carriers will, by ohmic conduction, relax the electric field of the wave much as if the problem were one of a stationary electric field in a stationary conducting medium. Once the relaxed distribution of carriers has been established, the pattern of carrier distribution will, by our assumption of equal velocities, keep step with the electric field pattern of the wave. For example, electrons bunched in the positive troughs of the wave will remain in the same positive troughs as they move along with the phase velocity of the wave. Under these circumstances, there will be zero exchange of energy between the two systems.

We should note parenthetically that while the drifting electrons do no work on the particular sound wave we have chosen, they *do* transmit energy to the system of phonons of the solid. This is the I^2R loss that exists due to a current I whether the particular sound wave we are considering is present or not. We ignore or subtract out this source of dissipation as being irrelevant to the problem at hand. That is, the two systems we are considering are the drifting electrons and a particular sound wave.

At this point we give the electrons a drift velocity larger than the velocity of the sound wave. Now the system of free electrons, instead of seeing a static field as they did when they kept step with the wave, will see an alternating electric field whose apparent frequency is given by

$$\omega_r = \frac{v - v_s}{v_s}\,\omega. \tag{8}$$

Here, v is the drift velocity of the electrons, v_s the phase velocity of the sound wave and ω its frequency. The alternating electric field will contribute a dissipative power over and above that necessary to merely give the electrons a drift velocity v. It is this added dissipation arising from the presence of a sound wave that we wish to compute.

The dissipation per unit volume in a medium of conductivity σ subjected to an a-c field is an elementary problem whose solution is

$$\begin{aligned} P_D &= \frac{\mathcal{E}_0^2\sigma}{2}\,\frac{1}{1+(\omega_c/\omega_r)^2} \\ &= \frac{\mathcal{E}_0^2\sigma}{2}\,\frac{(\omega_r/\omega_c)^2}{1+(\omega_r/\omega_c)^2}, \end{aligned} \tag{9}$$

where $\omega_c = 4\pi\sigma/K$, K is the relative dielectric constant, and $\mathcal{E}_0$ is the peak a-c field strength.

The physical problem and the equivalent circuit problem are shown in Figure 3. The physical problem consists of an a-c charge across a conducting dielectric while the equivalent circuit consists of an a-c voltage across a resistance in series with a capacitor.

From Equations (6)-(9) we compute the power delivered to the wave by the drifting stream of carriers:

$$\frac{dE}{dt} \equiv P_B = P_D\,\frac{v_s}{v - v_s} = P_D\,\frac{\omega}{\omega_r}$$

$$\frac{dE}{dt} = \frac{\mathcal{E}_0^2 K}{8\pi}\,\omega\,\frac{\omega_r/\omega_c}{1+(\omega_r/\omega_c)^2}. \tag{10}$$

Equation (10) matches Hutson's result if we ignore his diffusion term. To make the match with Hutson more evident we compute the gain constant ω_a defined by

$$E_{tot} = E_{tot}|_0 \exp \omega_a t, \tag{11}$$

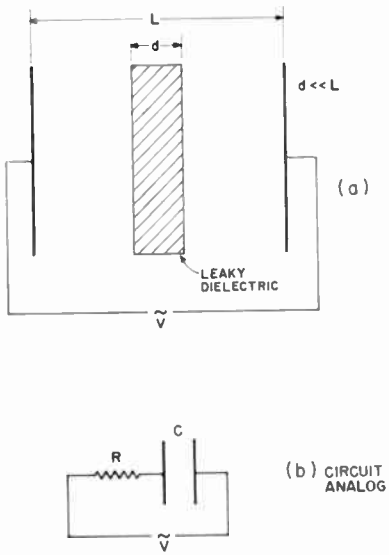

Fig. 3—Physical and circuit analogs of dissipation due to relative motion of the a-c electric field of a sound wave and a relaxable medium.

from which

$$\frac{dE_{tot}}{dt} = \omega_a E_{tot},$$

and

$$\omega_a = \frac{1}{E_{tot}}\frac{dE_{tot}}{dt}. \tag{12}$$

Here E_{tot} is the total energy density of the sound wave which is also equal to the kinetic or mechanical energy of the atoms at the time of zero displacement from their normal sites. That is, E_{tot} is the peak value of mechanical energy. It can be written in this form.

$$E_{tot} = \frac{1}{\beta} E_e = \frac{1}{\beta} \frac{\mathcal{E}_0^2 K}{8\pi}, \tag{13}$$

$$\text{where } \beta = \frac{\text{peak electrical energy}}{\text{total energy}} = \frac{\text{peak electrical energy}}{\text{peak mechanical energy}}. \tag{14}$$

In Equation (12) we replace E_{tot} by the right-hand side of Equation (13) and dE_{tot}/dt by the right-hand side of Equation (10) to obtain

$$\omega_a = \beta\omega \frac{\omega_r/\omega_c}{1 + (\omega_r/\omega_c)^2}. \tag{15}$$

Equation (15) is a particularly convenient form for quantitative estimates. For example, if $\beta \approx 1$ and $\omega_r = \omega_c$, the maximum rate of gain (or attenuation) is achieved, and corresponds to doubling (or halving) the energy of the sound wave at a rate of half the angular frequency of the wave. For $\beta < 1$, the maximum rate at which the wave gains energy would, according to Equation (10), be enough to double the *electrical* energy at this same rate of $\omega/2$. However, since the electrical energy is only a fraction of the total energy, and since the *latter* must be doubled to double the electrical energy, the rate of growth of either energy, that is, of the wave itself is reduced to $\beta\omega/2$.

We note also from Equation (10) that the maximum rate of change of energy of the sound wave is, as pointed out in section 2,

$$\left.\frac{dE}{dt}\right|_{\max} = \frac{1}{2} E_e \omega, \tag{16}$$

and occurs at $\omega_c = \omega_r$, that is, when the velocities of electrons and wave are such that their relative displacement is $\lambda/(2\pi)$ in the dielectric relaxation time ω_c^{-1}. This is the concept, already cited, that the critical relative velocity of two systems needed to produce a maximum rate of transfer of energy is given by the diameter of the energy well divided by the relaxation time of the medium.

At low relative velocities ($\omega_r \ll \omega_c$) the charge pattern moves adiabatically with the wave with vanishing dissipation and vanishing work done on the wave. This is a major factor responsible for the small attenuation of sound waves in metals for which $\omega_c \gg \omega_r$.

At high relative velocities ($\omega_r \gg \omega_c$) the electrons drift a distance of one wavelength in a time too short to relax the fields of the sound

wave. Hence, the work done on the wave again approaches zero. In this regime Equation (10) can be written to compare with Equation (1),

$$\frac{dE}{dt} = \left(E_e \frac{v_s}{v} \right) \omega_c, \tag{17}$$

where the depth of energy well is $E_e v_s / v$ and the relaxation time of the medium is ω_c^{-1}. The depth of well decreases as v^{-1}, as cited in the introduction.

3-C—Effect of Diffusion

Equation (15) for the gain constant was derived by computing the dissipation in a conducting medium due to an a-c field. Normally, one assumes that the density of carriers is not significantly perturbed in the process of relaxing the applied field. This is a valid assumption for long wavelengths of the applied field pattern. For sufficiently short wavelengths, however, the perturbed density of carriers can give rise to significant diffusion currents that tend to oppose the complete relaxation of the applied field. M. A. Lampert has shown (see Appendix I) that the inclusion of the diffusion term in the dissipation argument used to derive Equation (15) yields the complete Hutson result;

$$\omega_a = \beta\omega \frac{\omega_r/\omega_c}{(1 + \omega_D/\omega_c)^2 + (\omega_r/\omega_c)^2}. \tag{18}$$

where

$$\omega_D = \frac{4\pi^2 kT\mu}{e\lambda^2}. \tag{19}$$

Note that our definition of ω_D is the reciprocal of the diffusion transit time of an electron across $\lambda/(2\pi)$ and is not to be confused with Hutson's ω_D, which he defined as $v_s^2 e/(kT\mu)$.

There are several ways of interpreting the diffusion term ω_D/ω_c in Equation (18). The simplest is to say that when $\omega_D > \omega_c$ the electrons diffuse out of the positive trough of a wave in a time short compared with ω_c^{-1}, the dielectric relaxation time. It is as if the time allowed for relaxing the electric field of the sound wave were $(\omega_c/\omega_D)\omega_c^{-1}$ rather than ω_c^{-1}. Hence, only a fraction ω_c/ω_D of the maximum charge will be bunched in the troughs of the wave. In order to account for the diffusion factor ω_D/ω_c entering Equation (18) as a squared rather

than a first-power term, we need to recognize that the work done by the drifting stream of electrons on the sound wave is proportional not only to the amount of charge bunched in the troughs but also to the asymmetry of the bunching. That is, to be completely effective, the bunched charge should be on the forward flank of the wave. Diffusion attenuates the magnitude of bunched charge, as cited above, by the factor ω_c/ω_D and, at the same time, attenuates the asymmetry by the same factor. Both effects are due to the tendency for diffusion to smear the bunched carriers into a uniform distribution. Hence, the effect on the acoustic gain enters in as $(\omega_c/\omega_D)^2$ just as the term $(\omega_r/\omega_c)^2$ in the denominator of Equation (18). The factor ω_r/ω_c in the numerator of Equation (18) reflects the increased rate of doing work as ω_r (i.e., v) increases. This effect is physically distinct from that due to the term $(\omega_r/\omega_c)^2$ in the denominator, which reflects the incomplete bunching.

Other ways of interpreting ω_D/ω_c come from writing this ratio in the following forms:

$$\frac{\omega_D}{\omega_c} = \frac{4\pi^2 kT\mu}{e\lambda^2} \times \frac{K}{4\pi ne\mu}$$

$$= \frac{\pi kTK}{ne^2\lambda^2}$$

$$= \left(\frac{2\pi kT\Delta n}{e\lambda n}\right)\left(\frac{1}{\mathcal{E}}\right), \quad \text{where} \quad \mathcal{E} = \frac{2\Delta ne\lambda}{K} \approx \text{electric field of sound wave,} \tag{20}$$

$$= \left(\frac{kT\Delta n}{en}\right)\frac{1}{\Delta V}, \quad \text{where} \quad \Delta V = \frac{\Delta ne\lambda^2}{\pi K} \approx \text{potential trough of sound wave,} \tag{21}$$

$$= \left(\frac{2\pi\lambda_D}{\lambda}\right)^2, \quad \text{where} \quad \lambda_D = \text{Debye length} = \left(\frac{kTK}{4\pi ne^2}\right)^{1/2}. \tag{22}$$

Equation (20) converts ω_D/ω_c into the ratio of effective diffusion field to the electric field of the sound wave. In Equation (21) this ratio is

expressed as the ratio of the effective diffusion potential to the potential trough of the sound wave. In each case, the complete relaxation of the electric field of the sound wave is opposed by diffusion phenomena expressed either as a field or voltage.

In Equation (22) the ratio ω_D/ω_c is expressed as the square of the ratio of a Debye length to $\lambda/(2\pi)$, reflecting the well known fact that electric fields cannot be relaxed by conduction processes down to distances less than a Debye length.

3-D—Ratio of Electrical to Total Energy

(1) Meaning of Electrical and Total Energy

Consider for conceptual convenience a standing sound wave in a solid. At some phase in the oscillation of the sound wave all of the atoms will be at their maximum excursion and stationary. The energy of the sound wave is then entirely potential energy. At a later phase the atoms in the solid have zero displacement from their normal sites. The energy of the sound wave is then entirely the kinetic energy of moving atoms. We have called this kinetic energy the peak mechanical energy of the sound wave. The peak mechanical energy is clearly also the total energy of the sound wave.

At the phase when all of the atoms are at their maximum displacement, the total energy of the sound wave has been converted from kinetic energy to potential energy. We then compute how much of the potential energy can be dissipated by relaxation of the free carriers to lower energy states. This energy we have called the peak electrical energy and its ratio to the total energy (that is, the peak kinetic energy) we have called β, the ratio of electrical to total energy.

In this way we can distinguish between the general meaning of "electrical" and our restricted usage of it. The potential energy of a sound wave, for example, is finally an "electrical" energy since it is derived from the forces between neighboring ions and their valence electrons. But only a fraction of this energy is available for dissipation by the relaxation of free carriers, and it is this fraction that our restricted use of electrical energy refers to.

According to Equations (15) and (18), the distinction between the acoustoelectric gain constants for the several types of sound waves is contained in the coefficient β. The factor β enters in because the energy exchange between the sound wave and the free electrons is effected through the electrical energy accompanying the sound wave. At most, only the *electrical* energy of the wave can be doubled in one period of the wave. However, the energy needed to double the amplitude of sound wave is measured by the *total* energy of the wave. Maximum

gain is achieved when $\beta \rightarrow 1$, that is, when the electrical energy approaches equality with the total energy. As we shall see, this tends to occur both for the polar optical modes of highly polar solids and for the high-frequency limit of deformation-potential sound waves.*

(2) Polar Optical Waves

For ionic crystals, it has been shown[10] that the longitudinal and transverse modes of vibration are connected by the relation

$$\frac{\omega_t^2}{\omega_l^2} = \frac{\epsilon_\infty}{\epsilon_0}. \tag{23}$$

The energy of the transverse modes is almost purely elastic energy, since the average electric field of the transverse modes is substantially zero. By Maxwell's equations, the transverse field (which arises from the time variation of currents of ions) is negligible owing to factors of order v_s/c, where v_s and c are the velocities of sound and light, respectively. The potential energy of the *longitudinal modes*, however, is the sum of an elastic energy comparable with that of the transverse modes *and* an electrical energy arising from the relative displacement of positive and negative ions. Hence, we can rewrite Equation (23) in the form

$$\beta = \frac{\text{peak electrical energy}}{\text{total energy}} = \frac{\omega_l^2 - \omega_t^2}{\omega_l^2} = \frac{\epsilon_0 - \epsilon_\infty}{\epsilon_0}. \tag{24}$$

Note that for a crystal with point ions ($\epsilon_\infty = 1$), $\beta \doteq 1$ as one would expect. Here the total energy when the ions are at their maximum displacement is electrostatic potential energy. Subsequently, when the ions are at their normal sites, the total energy is the kinetic energy of the ions and is equal to the electrical potential energy that the ions had at their maximum displacement.

We note further that as the crystal changes from a purely ionic solid, $\epsilon_\infty \rightarrow \epsilon_0$ and the ratio of electrical to total energy as measured by Equation (15) approaches zero. For such nonpolar solids a new source of electrical energy enters in, as in germanium or silicon, to be derived from the deformation potential of the optical modes.[11]

---

* This expression denotes sound waves coupled to free carriers via a deformation potential.

[10] R. H. Lyddane, R. G. Sachs, and E. Teller, "On the Polar Vibrations of Alkali Halides," *Phys. Rev.*, Vol. 59, p. 673, April 15, 1941.

[11] R. H. Parmenter, "Uniform Strains and Deformation Potentials," *Phys. Rev.*, Vol. 99, p. 1767, Sept. 15, 1955.

When the value of β in Equation (23) is inserted in Equation (18), Gunn's expression[6] for the acoustoelectric effect for polar optical waves is essentially reproduced. The reproduction would be exact if Gunn had used the common approximation of a single frequency for his optical phonons.

(3) Piezoelectric Acoustic Waves

The ratio of electrical to total energy of a piezoelectric acoustic wave is given approximately by the square of the electromechanical coupling constant;

$$\beta_{PE} = \frac{\epsilon_p^2}{KC}, \tag{25}$$

where ϵ_p = piezoelectric constant, C = elastic modulus, and K = relative dielectric constant. In CdS, for example, $\beta_{PE} \approx 0.05$. Other materials that have appreciable values of β_{PE} are ZnO, GaAs, and quartz.

When the value of β_{PE} given by Equation (25) is inserted in Equation (18), the result of Hutson and White is reproduced.

While Equation (25) is a well-known expression, a short derivation of it is inserted here for convenience. We begin with the piezoelectric relations

$$T = CS - \epsilon_p \mathcal{E}, \tag{26}$$

$$D = K\mathcal{E} + \epsilon_p S, \tag{27}$$

where T is the applied stress, S the strain, and D the electric flux. We set $D = 0$, solve for $\mathcal{E}$ in Equation (27), and substitute the result in Equation (26) to get

$$T = CS + \frac{\epsilon_p^2}{K} S. \tag{28}$$

If we multiply both sides by $S/2$,

$$\frac{1}{2} ST = \frac{1}{2} CS^2 + \frac{1}{2} \frac{\epsilon_p^2}{K} S^2; \tag{29}$$

the first term on the right is an elastic energy and the second the electrical energy associated with the piezoelectric effect. The ratio of the electrical to the elastic energy terms reproduces Equation (25).

Since the electrical energy is small, this ratio is a good approximation to the ratio of electrical to total energy.

(4) Deformation-Potential Acoustic Waves

In order to derive a value for the electrical energy to be ascribed to deformation-potential acoustic waves, we make use of the equivalent electrical field $\mathcal{E}$ obtained from the spatial derivative of the potential due to deformation. One may question whether this is a real field in the sense that it should obey Maxwell's equations. However, there is no question that an electron moves in this field as if it were real. Hence, the electrical energy we are computing is the energy that is obtained when electrons slide into a potential trough in sufficient numbers to cancel the applied equivalent field. In brief, the electrical energy is $K\mathcal{E}'^2/(8\pi)$ as if $\mathcal{E}'$ were a real field.

The potential due to a deformation S is

$$V_D = \frac{B}{e} S, \tag{30}$$

where B is called the deformation potential,* e the charge on an electron, and S the mechanical strain. For an acoustic wave,

$$S = S_0 \sin\left(\frac{2\pi}{\lambda} x + \omega t\right). \tag{31}$$

The maximum field due to the deformation caused by the acoustic wave is, from Equations (30) and (31):

$$\mathcal{E}_0 = \frac{dV_D}{dx}\bigg|_{\max} = \frac{2\pi B}{e\lambda} S_0. \tag{32}$$

The maximum strain, S_0, can be written as

$$S_0 = \frac{2\pi}{\lambda} A. \tag{33}$$

* Note that B has the dimensions of energy (ergs) even though by convention it is called a "potential."[12]

[12] W. Shockley and J. Bardeen, "Energy Bands and Mobilities in Monatomic Semiconductors," *Phys. Rev.*, Vol. 77, p. 407, Feb. 1, 1950.

where A is the mechanical displacement amplitude of the wave. Hence Equation (32) becomes

$$\mathcal{E}_0 = \frac{4\pi^2 B}{e\lambda^2} A. \tag{34}$$

The peak electrical energy per unit volume is then

$$\begin{aligned} E_{elect} &= \frac{K\mathcal{E}_0^2}{8\pi} = \frac{KB^2}{8\pi e^2}\left(\frac{4\pi^2}{\lambda^2} A\right)^2 \\ &= \frac{KB^2\omega^4 A^2}{8\pi e^2 v_s^4}. \end{aligned} \tag{35}$$

The total energy is given by the peak kinetic energy per unit volume;

$$E_{tot} = \frac{1}{2}\rho A^2\omega^2, \tag{36}$$

where ρ is the density of the medium. From Equations (35) and (36) we get

$$\frac{E_{elect}}{E_{tot}} = \beta_{AD} = \frac{KB^2\omega^2}{4\pi\rho e^2 v_s^4}. \tag{37}$$

For long-wavelength phonons $\beta_{AD} \to 0$ since $\omega^2 \to 0$. At the other end of the spectrum, namely for $\omega = 10^{14}$ rad/sec, β_{AD} becomes of the order of unity for values of B of the order of ten electron volts per unit strain. [In Equation (32) the units of B are ergs per unit strain; the electronic charge is 4.7×10^{-10} esu.] This estimate is significant because it raises the question of whether β can, in principle, exceed unity. We will return to this question in Section 3-E(4) on spontaneous deformation.

(5) Nonpolar Optical Waves

Optical waves in nonpolar materials such as germanium and silicon do not have the obvious electric fields associated with them that the optical waves in ionic solids have. For our purposes an effective electric field can be constructed out of the concept of the optical deformation potential, first introduced by Parmenter,[11] which was defined as the energy shift of the band edge per unit displacement of the two

sublattices relative to each other. Conwell[13] quotes a value for the conduction band of germanium of 4×10^8 electron volts per centimeter.

We wish to compute the ratio of electrical to total energy (β_{OD}) for the nonpolar optical modes. If we take D to be the optical deformation potential, we can write, for the maximum effective electric field of a wave,

$$\mathcal{E}_0 = \frac{2\pi DA}{e\lambda}, \tag{38}$$

where A is the amplitude of displacement of the two sublattices relative to each other.

The peak energy density to be associated with the electric field is then

$$E_{elect} = \frac{K\mathcal{E}_0^2}{8\pi} = \frac{\pi K D^2 A^2}{2e^2\lambda^2}. \tag{39}$$

Here it is understood that the electrical energy is derived from the flow of electrons into the potential troughs.

As before, the total energy is given by energy density of the peak kinetic energy;

$$E_{tot} = \frac{1}{2}\rho A^2\omega^2. \tag{40}$$

Then

$$\frac{E_{elect}}{E_{tot}} = \beta_{OD} = \frac{\pi K D^2}{\rho e^2 \omega^2 \lambda^2}. \tag{41}$$

Parenthetically, it is worth noting that $\beta_{OD} \approx 1$ for $K = \rho = 10$, $D = 4 \times 10^8$ ev/cm, $\omega = 5 \times 10^{13}$ rad/sec, and $\lambda = 6 \times 10^{-8}$ cm.

(6) Intervalley Deformation-Potential Waves

The ratios of electrical to total energy that have been computed thus far for the several types of sound waves have all been limited by the amount of charge that can be accumulated in a potential trough of the sound wave. This charge was limited by the actual or effective electric field in the wave. In contrast to this spatial type of bunching of electrons, Holstein, as quoted by Weinreich,[14] has proposed that for

[13] E. M. Conwell, "Relative Energy Loss to Optical and Acoustic Modes of Electrons in Avalanche Breakdown in Ge," *Phys. Rev.*, Vol. 135, p. A1138, 17 Aug. 1964.

[14] G. Weinreich, T. M. Sanders, Jr., and H. G. White, "Acoustoelectric Effect in n-Type Germanium," *Phys. Rev.*, Vol. 114, p. 33, April 1, 1959.

deformations that remove the degeneracy of equivalent valleys in the energy band structure, a bunching in phase space will take place. That is, electrons that populate equivalent valleys equally in unstrained material will tend to populate the lower of the two valleys (Figure 4) when the material is strained and the valleys are energetically separated. The energy to be gained from the repopulation of valleys is proportional to the density of electrons and is not constrained by the

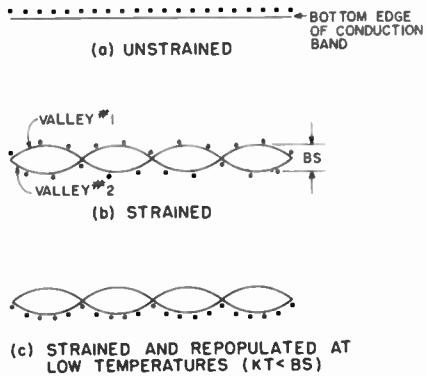

Fig. 4—Schematic diagram of electrical energy gained from a relative shift of valleys due to a shear deformation.

space charge that would arise from a spatial bunching. Pomerantz[15] gives the following expression for ω_a (translated into our terminology):

$$\omega_a = \left[\frac{nB^2}{9\rho v_s^2 kT} \right] \omega \frac{\omega_r/\omega_c}{1 + (\omega_r/\omega_c)^2}, \tag{42}$$

where n is the density of free electrons, B the deformation potential (energy spread between valleys per unit strain), and $\omega_c = \tau_c^{-1}$, where τ_c is the relaxation time for repopulation of the valleys.

Equation (42) matches our general relation, Equation (15), if we can show that the bracketed part of Equation (42) is equal to β, the ratio of electrical to total energy. To do so we write the electrical energy per unit volume as

$$E_{elect} = \frac{nBS}{2} \left(\frac{BS}{kT} \right). \tag{43}$$

[15] M. Pomerantz, "Amplification of Microwave Phonons in Germanium," *Phys. Rev. Letters*, Vol. 13, p. 308, 31 Aug. 1964.

Here $nBS/2$ is the electrical energy that would be gained if all of the electrons in the upper valley dropped into the lower valley. Since, however, the deformation energy BS is small compared with kT, only the fraction $BS/(kT)$ will undergo repopulation. For degenerate material, the fraction is $(3/2)(BS/E_f)$, where E_f is the Fermi energy.

The total energy, as before, is

$$E_{tot} = \frac{1}{2}\rho\omega^2 A^2 = \frac{1}{2}\rho v_s^2 \left(\frac{2\pi A}{\lambda}\right)^2 = \frac{1}{2}\rho v_s^2 S^2. \tag{44}$$

From Equations (43) and (44),

$$\beta_{VD} = \frac{E_{elect}}{E_{tot}} = \frac{nB^2}{\rho v_s^2 kT}. \tag{45}$$

This matches the bracketed part of Pomerantz's Equation (42) except for the numerical factor of 9. The numerical factor arises because our value of B is defined for valleys lying in the [100] direction while the valleys in germanium lie in the [111] direction. When B is resolved along the [111] direction the resultant deformation constant is $B/3$ (see Reference (14)).

(7) Metals

In the case of metals, the major source of electrical energy comes from the change in kinetic energy of the electrons when the lattice is compressed or expanded by a sound wave. Consider, for example, the compression half of a longitudinal sound wave (Figure 5b). The first effect of the compression is to increase the kinetic energy of the component of electron velocity along the line of propagation. The increase is a direct result of the increased density of electrons. After an energy relaxation time τ_c, determined by collisions with the lattice, the excess energy along the direction of propagation is distributed among all three dimensions, so that there is a common Fermi level (Figure 5c) somewhat higher than the thermal equilibrium Fermi level. It is this relaxation energy that constitutes the electrical energy of the system available for dissipation of the total energy of the sound wave (see Section 3-D(1)).

The magnitude of the electrical energy can be estimated as follows. Let an element of volume of the metal suffer a strain S along each direction so that the density of electrons will be

$$n = n_0 (1 + 3S), \tag{46}$$

and the Fermi level will be

$$E_f = An^{2/3} = An_0^{2/3}\,(1+3S)^{2/3}$$
$$= E_{f0}\,(1+2S). \tag{47}$$

Here n_0 and E_{f0} are the unstrained thermal equilibrium values.

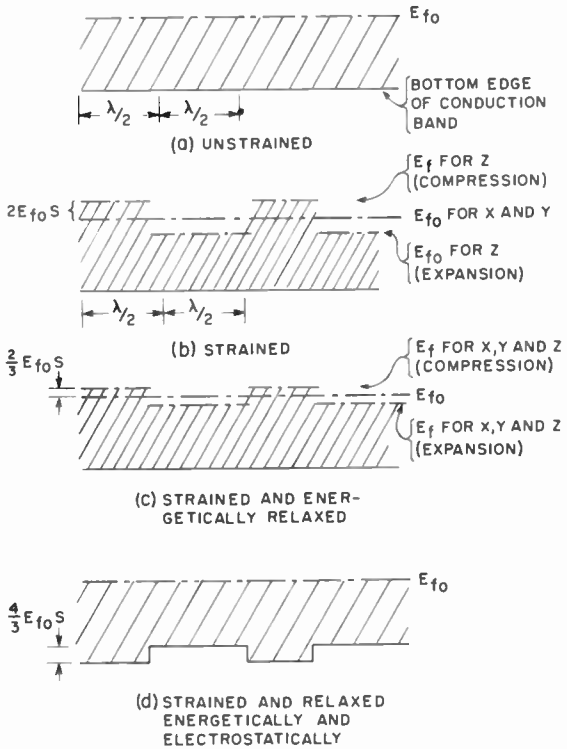

Fig. 5—Schematic diagram of electrical energy gained when a metal is deformed by a periodic wave.

Now if we remove the strain from two of the axes and retain it on the third, the above relations will remain valid for the third axis. Hence we have an excess density of kinetic energy along one axis. This energy will be relaxed until it is distributed along all three axes. The excess energy before relaxation is, from Equation (47),

$$\frac{3}{2}\left[\left(\frac{1}{3}\right)\left(\frac{1}{2}\right)\frac{(2E_{f0}S)}{E_{f0}}n_0\right]\times\left[2E_{f0}S\right] = n_0E_{f0}S^2. \tag{48}$$

The first square bracket is the number of electrons lying in the interval between E_{f0} and E_f, that is, in the energy range $2E_{f0}S$.* The factor 1/3 is due to counting electrons along one axis only. The factor 1/2 accounts for averaging the energy over the excess electrons. The second square bracket is the height by which the Fermi level was raised.

The excess energy after relaxation to a common Fermi level (see Figure 5c) is computed as in Equation (48) using all of the electrons and an energy, $E_f - E_{f0} = (2/3)E_{f0}S$. The result is 1/3 the result for Equation (48). Hence, the electrical energy is

$$E_{elect} = \left(1 - \frac{1}{3}\right) n_0 E_{f0} S^2 = \frac{2}{3} n_0 E_{f0} S^2. \tag{49}$$

and the ratio of electrical to total energy is

$$\beta_M = \frac{\frac{2}{3} n_0 E_{f0} S^2}{\frac{1}{2} \rho v_s^2 S^2} = \frac{4}{3} \frac{n_0 E_{f0}}{\rho v_s^2}. \tag{50}$$

In a simplified model of a metal, as shown by Bohm and Staver[16] and quoted by Pines,[17] the following relation holds:

$$\frac{1}{2} \rho v_s^2 = \frac{1}{3} n_0 E_{f0}. \tag{51}$$

From Equations (51) and (50),

$$\beta_M = 2. \tag{52}$$

This estimate of β_M is probably high, owing to the approximate nature of Equation (51). If true, it would lead to a gross instability of the metal (see Section 3-E(4)). The approximation, however, is sufficient for our immediate purpose.

---

* Since $n \propto E_f^{3/2}$ it follows that $\Delta n/n = (3/2)\Delta E_f/E_f$.

[16] D. Bohm and T. Staver, "Application of Collective Treatment of Electron and Ion Vibrations to Theories of Conductivity and Superconductivity," *Phys. Rev.*, Vol. 84, p. 836, Nov. 15, 1951.

[17] D. Pines, "Electron Interaction in Metals," *Solid State Physics*, Edited by F. Seitz and D. Turnbull, Vol. 1, p. 367, Academic Press, New York, 1955.

Equation (52) is inserted into Equation (15) to obtain

$$\omega_a = 2\omega \frac{\omega_r/\omega_c}{1 + (\omega_r/\omega_c)^2}. \tag{53}$$

While Equation (53) shows that, in principle, sound waves can be amplified by a drifting stream of carriers in a metal, such amplification is not likely, in practice, since drift velocities in excess of 3×10^5 cm/sec, corresponding to current densities in excess of about 10^9 amperes/cm^2, are needed. A more realistic test of Equation (53) is to evaluate it for the attenuation of sound waves, namely for $|\omega_r| = \omega$. Also we take $\omega_c = \tau_c^{-1} \gg \omega$. Equation (53) then becomes

$$\omega_a = 2\omega^2\tau_c. \tag{54}$$

Equation (54) is to be compared with the result obtained by Pippard[18] or, more recently, by Levy[19];

$$\omega_a = \frac{4}{15}\frac{mn}{\rho\tau_c}(ql)^2, \tag{55}$$

where $q = 2\pi/\lambda$, $l = v_0\tau_c$ and $(1/2)\ mv_0^2 = E_f$. These values substituted into Equation (55) yield

$$\omega_a = \frac{8}{15}\frac{nE_f\omega^2\tau_c}{\rho v_s^2}. \tag{56}$$

Pippard points out that τ_c is the velocity relaxation time and is twice as large as the energy relaxation time, which we have used. Hence, for comparison, Equation (56) should be multiplied by a factor of 2 to convert τ_c into an energy relaxation time.

Again making use of Equation (51), Equation (56) becomes

$$\omega_a = \frac{8}{5}\omega^2\tau_c. \tag{57}$$

Our Equation (49) is in close agreement with Equation (57).

---

[18] A. B. Pippard, "Ultrasonic Attenuation in Metals," *Phil. Mag.*, Vol. 46, p. 1104, Oct. 1955.

[19] M. Levy, "Ultrasonic Attenuation in Superconductors for $ql < 1$." *Phys. Rev.*, Vol. 131, p. 1497, 15 Aug. 1963.

Equation (57) is for longitudinal sound waves. The result for transverse sound waves, according to Pippard and Levy, is the same except that the numerical factor is 10% smaller. The substantial equivalence of longitudinal and transverse waves is not unreasonable, since the pattern of raising and lowering of Fermi levels that holds for successive half wavelengths of a longitudinal wave is reproduced in each half wavelength of the transverse wave. A shear distortion results in the increase in one dimension and a decrease in an orthogonal dimension without a change in volume.

Note that in the case of longitudinal waves the transfer of charge between the two half wavelengths needed to bring their Fermi levels to the same value (Figure 5d) contributes a negligible energy at long wavelengths but can be significant at wavelengths approaching lattice dimensions.

3-E—General Remarks

(1) Comparative Effects

It is clear that the parameter electrical energy/total energy assesses directly the relative strengths of the interaction between electrons and the several types of sound waves. At long wavelengths ($\lambda \geqq 10^{-5}$ cm), for example, the interactions with acoustic and nonpolar optical deformation-potential waves rapidly become small compared with piezoelectric or polar optical waves, since the ratios of electrical to total energy of the former decrease as λ^{-2}. The electrical energy decreases at long wavelengths owing to the reduction in charge that can be accumulated in the potential troughs. The reduction in charge arises from the reduced electric fields at long wavelengths. For piezoelectric and polar optical waves, the ratio of electrical to total energy is a constant independent of wavelength since the electric field is proportional to the elastic strain. In the case of the electrical energies arising from the relative shift of equivalent valleys, there is no spatial bunching of electrons, so that the ratio of electrical to total energy is again a constant independent of wavelength.

Figure 6 shows some representative curves for the ratio of electrical to total energy versus the reciprocal of the wavelength of the various types of sound waves. The curves for deformation-potential acoustic and optical waves exceed unity at the shortest wavelengths. It is questionable, of course, whether the deformation potential retains its validity in this range. At these short wavelengths the densities of carriers needed to relax the electric fields lie in the range of degeneracy. For effective relaxation the Debye length should be less than $\lambda/2$, that is,

$$\left(\frac{KkT}{4\pi ne^2}\right)^{1/2} \leqq \frac{\lambda}{2},$$

or

$$n \geqq \frac{KkT}{\pi e^2 \lambda^2}. \tag{58}$$

This leads to degeneracy at room temperature for $\lambda \leqq 10^{-6}$ cm.

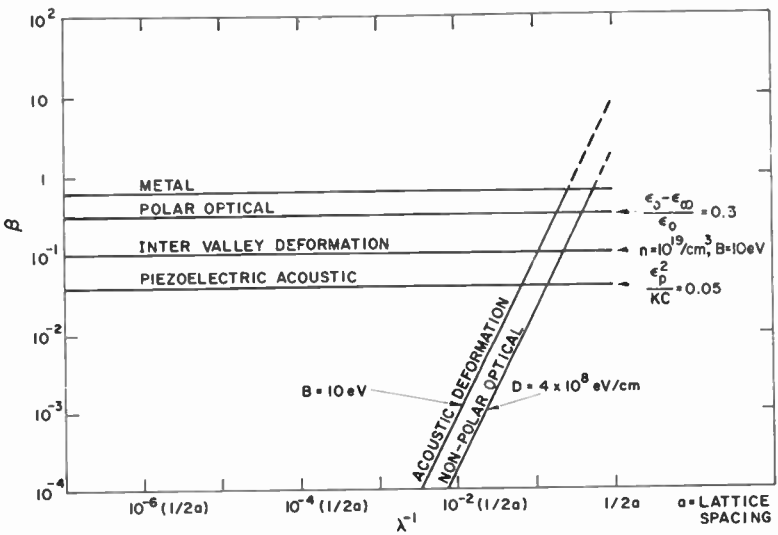

Fig. 6—Plot of β, the ratio of electrical to total energy, as a function of reciprocal wavelength for the various types of phonons. Parameters used in calculating these curves other than those shown on the figure are: $K = 10$, $\omega_{max} = 5 \times 10^{13}$ rad/sec, $\rho = 5$ grams/cm^3, $v_s = 5 \times 10^5$ cm/sec, $T = 300°$K.

The interaction of electrons with polar optical waves appears to be one of the strongest, since their ratio of electrical to total energy may be as high as 0.5 compared, for example, with 0.05 for piezoelectric waves or 0.1 for the intervalley deformation potential waves. The difficulty, however, is that the drift velocity of the electrons must exceed the *phase* velocity of the optical phonons. The latter increases toward long wavelengths as $\lambda\omega/(2\pi)$ where $\omega \approx 10^{14}$ rad/sec. Hence, for $\lambda \approx 10^{-6}$ cm, the phase velocity already exceeds 10^7 cm/sec—a reasonable upper limit to the drift velocity in most materials. A further limitation to the interaction with optical waves in accordance with Equation (18) is that the validity of this equation was based on the implied assumption that the mean free path of carriers was less than

$\lambda/(2\pi)$. Longer mean free paths would lead to a quantum rather than classical approach. If we take $\lambda \approx 10^{-6}$ cm as the longest reasonable wavelength with which carriers can interact (based on a drift velocity of 10^7 cm/sec), their mobility mean free path must be less than 2×10^{-7} cm and their mobility accordingly must be less than about 20 cm^2/volt-sec. The result is that Equation (18) has a rather narrow region of validity for optical waves. It lies in the neighborhood of $\lambda \approx 10^{-6}$ cm, carrier drift velocity $\approx 10^7$ cm/sec, and mobility ≈ 10 cm^2/volt-sec.

(2) Transverse Electric Fields

The method used here for computing the acoustoelectric gain (or loss) depends upon the presence of a relaxable field or energy associated with the sound wave. Hence, the method is valid for longitudinal electric fields and for the relaxation of energy involved in the repopulation of shifted valleys. It is not immediately evident that the method is also valid for electric fields transverse to the direction of propagation. Such fields are in any event almost vanishingly small for sound waves since, by Maxwell's equations, they must arise from a time rate of change of magnetic field associated with moving ions. Hence, these transverse fields are in the order of (velocity of sound)/(velocity of light) smaller than the longitudinal fields arising from the ionic charges themselves.

We do know that the transverse component of electric field of a sound wave can cause an attenuation of the energy of the sound wave at the rate $\mathcal{E}^2_{trans}\sigma$. Moreover, since this rate of dissipation is a function of the relative velocities of the sound wave and the drifting carriers we can still make use of Equations (5)-(6) to derive an acoustoelectric effect. For example, an electron drifting with the phase velocity of a sound wave should see a "static" surround, that is, no time-varying currents or magnetic fields and hence no electric field. For such drift velocities the dissipation should vanish. Similarly, electrons drifting much faster than the phase velocity of the sound wave should see a higher transverse electric field than that seen by nondrifting electrons and should lead to a higher rate of dissipation and, by Equations (5)-(6), to amplification of the sound wave.

Note that the transverse electric fields of a sound wave can also be relaxed by the motion of electrons but not in the same way longitudinal fields are relaxed. The transverse fields are derived from the time-varying magnetic fields of the ionic currents. If the electrons keep pace with the ions, the net current, and hence the transverse electric field, will approach zero. This is the situation that obtains in metals.

A more pertinent example of pure transverse fields is that of electromagnetic radiation. The absorption of light by free carriers leads to a d-c current since, by the well-known phenomenon of radiation pressure, the momentum of the light wave is first absorbed by the free carriers and then passed on to the crystal lattice. If, however, the electrons drift with the speed of light in the medium, they should see zero electric field since, by Maxwell's equations, the force on an electron is

$$F = e\left[\mathcal{E} - \frac{v}{c}H\right]$$

$$= e\left[\mathcal{E} - \frac{c}{\epsilon_x^{1/2}c}\epsilon_x^{1/2}\mathcal{E}\right] = 0. \tag{59}$$

since $H^2 = \epsilon_x \mathcal{E}^2$.

By the same argument, electrons drifting faster than the speed of light in the medium should see an increasing transverse electric field and suffer increasing dissipation and hence, by Equations (5)-(7), should amplify a coherent beam of light or a radio wave. (See Appendix II by Lampert.)

(3) Acoustoelectric Currents

Our discussion has emphasized the amplification of sound waves by a drifting stream of carriers. On the other hand, when the carriers are stationary the same expression (Equation (18)) gives the attenuation or rate of loss of energy of the acoustic waves. By Equation (6) we can convert the rate of loss of energy of the sound wave into an equivalent electric field acting on the free carriers:

$$\omega_a E_{tot} = F v_s = \mathcal{E} e n v_s. \tag{60}$$

Here E_{tot} is the energy density of the sound wave, n the density of the free carriers, and $\mathcal{E}$ the equivalent electric field acting on the carriers. The acoustoelectric current would then be $\mathcal{E} ne\mu$. It was this current and field that Parmenter identified in his pioneer paper as the acoustoelectric current and field.

(4) Spontaneous Deformation

If the electrical energy to be gained from the relaxation of electrons in a deformed lattice exceeds the work required to effect the deformation, the lattice will spontaneously deform to a lower energy state. The criterion for this spontaneous deformation is, by definition, $\beta > 1$.

Such an inequality is logically impossible for polar optical waves and piezoelectric waves because the form of β is

$$\beta = \frac{\text{electrical energy}}{\text{total energy}} = \frac{\text{electrical energy}}{\text{elastic energy} + \text{electrical energy}}.$$

That is, the energy of the electric field is itself a part of the total energy. In these cases there is a macroscopic, easily identifiable electric field.

In the case of the acoustic and the optical deformation-potential waves, however, it is not clear that the "field" that causes electrons to accumulate in the troughs of the waves is of such a character that its energy should be added to a separate elastic energy in order to obtain the total energy. If this were so, then, of course β would always be less than or equal to unity. If this were not so, then β could possibly exceed unity and lead to a spontaneous deformation of the lattice. Since β approaches unity only at the shortest wavelengths, the spontaneous deformation would occur only for metallic densities of electrons. The short-wavelength deformation of the lattice would then give rise to a small forbidden gap at the Fermi level. This is the type of model that Frohlich[20] proposed in 1953 for a superconductor.

Even when the electrical energy is less than the total energy, its presence can still be observed as a change in the elastic constant and, hence, of the velocity of sound. The electrical energy makes it easier to deform the solid. Such an effect was reported by Bruner and Keyes[21] for degenerate germanium with a carrier concentration of 3×10^{19}/cm^3. The effect was a 5 per cent decrease in the elastic constant. The electrical energy was derived from the relative energy shift of equivalent valleys. The electrical energy for intervalley deformation is given by Equation (45) for nondegenerate materials. Degeneracy is taken into account by replacing the factor $BS/(kT)$ by $(3/2)(BS/E_f)$. The resulting expression is

$$\beta_{VD} = \frac{3n_0B^2}{2\rho v_s^2 E_f}, \tag{61}$$

[20] H. Fröhlich, "On the Theory of Superconductivity: the One-Dimensional Case," *Proc. Roy. Soc.* (London), Vol. A223, p. 296, 6 May, 1954.

[21] L. J. Bruner and R. W. Keyes, "Electronic Effect in the Elastic Constants of Germanium," *Phys. Rev. Letters*, Vol. 7, p. 55, July 15, 1961.

which matches Bruner and Keyes' expression within a numerical factor of order unity.

(5) Recapitulation

Table I lists the time constant ω_a for amplification or attenuation of the various sound waves. Several comments on Table I need to be made.

(a) ω_a is the time rate of change of energy for the various sound waves, normalized to their energy density. For example, ω_a^{-1} is the time required to approximately double the energy density of the sound wave in the case of amplification ($\omega_r > 0$) or to halve the energy density in the case of attenuation ($\omega_r < 0$).

(b) ω_a can be converted into a space rate of change of energy by dividing by the group velocity v_g.

(c) The maximum value of ω_a is approximately ω, the frequency of the sound wave, and occurs for $\beta = 1$ and $\omega_r = \omega_c$.

(d) All of the expressions are taken from the published literature cited with the exceptions of the deformation potential acoustic and the nonpolar optical waves. For the acoustic waves there was no convenient expression with which to compare our results. For the optical waves, no published discussion was found.

(e) The dielectric constants for the polar optical waves are specifically labeled as ϵ_0 for the low-frequency value and ϵ_∞ for the high-frequency or optical value. In the case of the acoustic waves the symbol K is used for the dielectric constant. Its value will be a function of the doppler shifted frequency, ω_r. However, for nonpolar materials the dielectric constant varies by considerably less than a factor of two from low to high frequencies.

(f) The velocity of sound v_s is the phase velocity and for optical waves this velocity rapidly takes on large values as the wavelength increases. For optical waves $v_s \approx 10^{13}\lambda$ cm/sec.

(g) The arguments used to obtain most of the expressions in Table I involve the conductivity, σ, of the medium. In order for the conductivity to retain its d-c value, the collision time of the electron should be less than ω_r^{-1}. This condition is not appropriate for the case of intervalley deformation and metals where the collision time is itself the energy relaxation time.

(h) The diffusion term does not appear in the cases of intervalley deformation and of metals, because the energy relaxation processes considered do not involve a spatial redistribution of electrons.

Table II lists the time rates of energy loss by fast electrons to the various types of phonons and to plasmons and Cerenkov radiation. The

physical arguments for deriving these expressions will be given in Part II of this paper. These expressions have been taken out of the literature and recast algebraically in a common form to show that the key parameter for the energy losses to phonons is the ratio of electrical to total energy for the various phonons. It is this same parameter that characterizes the several acoustoelectric effects listed in Table I. In the case of energy losses to electronic excitations, β satisfies the more general definition, as will be discussed in Part II, namely, the fraction of available coulomb energy used in forming an energy well.

Appendix I*—Interchange of Energy between a Longitudinal Electric Wave and Drifting Carriers in a Solid

Consider a longitudinal electric wave in a solid in the absence of conduction electrons (or holes):

$$\vec{\mathcal{E}} = \hat{z}\mathcal{E}_0 \exp i(\omega t - kz). \tag{62}$$

For example, $\vec{\mathcal{E}}$ could be the electric field associated with a piezoactive acoustic wave in CdS.

In the presence of conduction electrons the "impressed" field $\mathcal{E}_0$ will be partially relaxed to a new value $\mathcal{E}_e$, which can be written

$$\mathcal{E}_e = \mathcal{E}_0 - \mathcal{E}_i, \tag{63}$$

where $\mathcal{E}_i$ is the field induced by the relaxation, i.e., by space charge ρ_i created in the relaxation process.

If further the conduction electrons are drifted in the direction $+z$ of the wave at velocity v, then the angular frequency "seen" by the electrons is

$$\omega_r = \omega \frac{|v - v_s|}{v_s}, \qquad v_s = \frac{\omega}{k}, \tag{64}$$

and all a-c quantities, in the frame of reference moving with the electrons, have the space–time variation $\exp i(\omega_r t - kz)$. Hence the operators $\nabla\cdot$ and $\partial/\partial t$, in this frame of reference, become $-ik\hat{z}\cdot$ and $i\omega_r$, respectively.

* The Appendixes to this paper were written by M. A. Lampert.

Table I—Time Constant (ω_a) for Rate of Change of Energy Density in Sound Waves

Phenomenon	ω_a	Source
Polar Optical	$\left[\frac{\epsilon_0 - \epsilon_\infty}{\epsilon_0}\right] \omega f(\omega_r,\omega_c,\omega_D)$	Gunn[6] Woodruff[7]
Piezoelectric Acoustic	$\left[\frac{\epsilon_p^2}{KC}\right] \omega f(\omega_r,\omega_c,\omega_D)$	Hutson, McFee and White[5]
Deformation Potential Acoustic	$\left[\frac{KB^2\omega^2}{4\pi\rho e^2 v_s^4}\right] \omega f(\omega_r,\omega_c,\omega_D)$	Parmenter[2] Weinreich[3]
Nonpolar Optical	$\left[\frac{\pi K D^2}{\rho e^2 \omega^2 \lambda^2}\right] \omega f(\omega_r,\omega_c,\omega_D)$	
Intervalley Deformation Potential	$\left[\frac{nB^2}{\rho v_s^2 kT}\right] \omega f(\omega_r,\omega_c)$	Weinreich[3] Pomerantz[15]
Metals	$[\approx 1] \quad \omega f(\omega_r,\omega_c)$ or $\omega^2\tau_c$ for $\omega_r = \omega$ and $\omega\tau_c \ll 1$	Pippard[18] Levy[19]

Note that the above expressions are valid for the mean free path of the electrons less than the wavelength of the sound wave.

Definitions for Table I

$\omega_a = \frac{1}{E}\frac{dE}{dt}$; E = energy density of sound wave

$f(\omega_r,\omega_c) = \frac{\omega_r/\omega_c}{1 + (\omega_r/\omega_c)^2}$,

$\omega_r = \omega(v_d - v_s)/v_s$,

$\omega_D = 4\pi^2 kT\mu/(e\lambda^2)$,

$\omega_c = 4\pi\sigma/K$, or $\omega_c = \tau_c^{-1}$ for metals and intervalley deformation, where τ_c is the time for an electron to come to thermal equilibrium,

v_d = drift velocity of electrons,

v_s = phase velocity of sound,

ϵ_0 = low-frequency dielectric constant,

ϵ_∞ = high-frequency (optical) dielectric constant,

K = dielectric constant,

Definitions for Table I (continued)

ϵ_p = piezoelectric constant,

C = elastic modulus,

B = deformation potential (electron volts in ergs/unit strain),

D = optical deformation potential (electron volts in ergs per centimeter relative shift of sublattices).

Table II—Time Rates of Loss of Energy by Electrons of Velocity v.

Phenomenon	dE/dt	Source
Polar Optical Phonons	$\left[\frac{\epsilon_0 - \epsilon_\infty}{\epsilon_0}\right]\frac{e^2\omega^2}{\epsilon_\infty v}\ln\left(\frac{2mv^2}{\hbar\omega}\right)$ Note: $\frac{1}{2}mv^2 > \hbar\omega$	Fröhlich[22] Callen[23]
Piezoelectric Phonons	$\frac{\pi}{4}\left[\frac{\epsilon_p^2}{KC}\right]\frac{e^2\omega^2}{Kv}$ Note: $2mv = \hbar\omega/v_s$	Tsu[24]
Acoustic Phonons	$\frac{1}{4}\left[\frac{B^2\omega^2K}{4\pi e^2\rho v_s^4}\right]\frac{e^2\omega^2}{Kv}$ Note: $2mv = \hbar\omega/v_s$	Seitz[25] Conwell[13]
Nonpolar Optical Phonons	$\frac{1}{2}\left[\frac{\pi KD^2}{\rho e^2\omega^2\lambda^2}\right]\frac{e^2\omega^2}{Kv}$ Note: $\frac{1}{2}mv^2 > \hbar\omega$ and $\frac{\lambda}{2\pi} = \frac{\hbar}{2mv}$	Conwell[13]
Electronic excitations	$\left[\frac{\omega_p^2}{\omega_e^2}\right]\frac{e^2\omega_e^2}{v}\ln\left(\frac{2mv^2}{\hbar\omega_e}\right)$ Note: $\omega_p = \frac{4\pi ne^2}{m} \leq \omega_e$ n = density of electrons whose excitation energy is $\hbar\omega_e$ $\frac{1}{2}mv^2 > \hbar\omega_e$	Bohr[26] Bethe[27]
Plasmons	[1] $\frac{e^2\omega^2}{v}\ln\left(\frac{2mv^2}{\hbar\omega}\right)$ Note: ω = plasma frequency and $\frac{1}{2}mv^2 > \hbar\omega$	Bohm and Pines[28]
Cerenkov	$\left[1 - \frac{1}{\epsilon_\infty}\right]\frac{e^2\omega^2}{v}$ Note: $v = c$ = velocity of light in vacuum	See, e.g., Schiff[29]

Definitions for Table II

ϵ_0 = low-frequency dielectric constant,

ϵ_∞ = high-frequency (optical) dielectric constant,

K = dielectric constant,

ϵ_p = piezoelectric constant,

C = elastic modulus (dynes/cm^2),

ρ = density (grams/cm^3),

v_s = phase velocity of sound,

v = velocity of electron,

ω = angular frequency of sound wave,

B = deformation potential (electron volts in ergs/unit strain)

D = optical deformation potential (electron volts in ergs per centimeter relative shift of sublattices),

m = effective mass of electrons.

References for Table II

[22] H. Fröhlich, "On the Theory of Dielectric Breakdown in Solids," *Proc. Roy. Soc.* (London), Vol. A188, p. 521, 25 Feb. 1947.

[23] H. B. Callen, "Electric Breakdown in Ionic Crystals," *Phys. Rev.*, Vol. 76, p. 1394, Nov. 1, 1949.

[24] R. Tsu, "Phonon Radiation by Uniformly Moving Charged Particles in Piezoelectric Solids," *Jour. Appl. Phys.*, Vol. 35, p. 125, Jan. 1964.

[25] F. Seitz, "On the Theory of Electron Multiplication in Crystals," *Phys. Rev.*, Vol. 76, p. 1376, Nov. 1, 1949.

[26] N. Bohr, *Phil. Mag.*, Vol. 25, p. 10, 1913; Vol. 30, p. 581, 1915.

[27] H. Bethe, *Ann. Phys.*, Vol. 16, p. 285, 1933; *Handbuch der Physik* (Geiger and Scheel, eds.), Vol. 24, Part I, Springer, Berlin, 1933.

[28] D. Bohm and D. Pines, "A Collective Description of Electron Interactions: III. Coulomb Interactions in a Degenerate Electron Gas," *Phys. Rev.*, Vol. 92, p. 609, Nov. 1, 1953 (Quoted by L. Marton et al. in *Advances in Electronics*, L. Marton, ed., Vol. 7, p. 230, Academic Press, New York, 1955.)

[29] L. I. Schiff, *Quantum Mechanics*, p. 271, McGraw-Hill Book Co., New York, 1955.

The Poisson and continuity equations are, respectively, (MKS units)

$$\epsilon \nabla \cdot \vec{\mathcal{E}}_i = \rho_i \rightarrow \mathcal{E}_i = \frac{i}{k\epsilon} \rho_i \tag{65}$$

$$\nabla \cdot \vec{J} + \frac{\partial \rho_i}{\partial t} = 0 \rightarrow \rho_i = \frac{k}{\omega_r} J = \frac{k\sigma_0}{\omega_r} \mathcal{E}_e, \tag{66}$$

where we have used

$$\vec{J} = \sigma \vec{\mathcal{E}}_e, \quad \sigma = \frac{\sigma_0}{1 + i\omega_r \tau} \approx \sigma_0 = \frac{e^2 n_0 \tau}{m^*}, \qquad (\omega_r \tau \ll 1). \tag{67}$$

Note that the current flows in response to the *net* field, $\mathcal{E}_e$, acting on the charges.

Combining Equations (65), (66), and (63) we obtain

$$\mathcal{E}_i = i \frac{\omega_c}{\omega_r} \mathcal{E}_e, \qquad \mathcal{E}_e = \frac{\mathcal{E}_0}{1 + i \dfrac{\omega_c}{\omega_r}}, \tag{68}$$

with $\omega_c = \dfrac{\sigma_0}{\epsilon}$.

Finally, the average power dissipation P_D is, taking $\sigma \simeq \sigma_0$,

$$P_D = \frac{1}{2} \operatorname{Re} (\sigma \mathcal{E}_e \mathcal{E}_e^*) \rightarrow P_D \simeq \frac{1}{2} \sigma_0 \mathcal{E}_0^2 \frac{1}{1 + \left(\dfrac{\omega_c}{\omega_r} \right)^2}. \tag{69}$$

Equation (69) is the same as Equation (9).

The inclusion of diffusive current flow in the analysis is straightforward. Equation (67) is replaced by

$$\vec{J} = \sigma \vec{\mathcal{E}}_e + D \nabla \rho_i \rightarrow J \simeq \sigma_0 \mathcal{E}_e - iDk\rho_i. \tag{70}$$

Now the continuity equation yields, in place of Equation (66),

$$\rho_i = \frac{k}{\omega_r} J = \frac{k\sigma_0/\omega_r}{1 + i \dfrac{Dk^2}{\omega_r}} \mathcal{E}_e, \tag{71}$$

and the relations in Equation (68) become

$$\mathcal{E}_i = \frac{i\frac{\omega_c}{\omega_r}\mathcal{E}_e}{1+i\frac{Dk^2}{\omega_r}}; \quad \mathcal{E}_e = \frac{1+i\frac{Dk^2}{\omega_r}}{1+i\left[\frac{Dk^2+\omega_c}{\omega_r}\right]}. \tag{72}$$

Using Equations (70) and (71), Equation (67) is replaced by

$$J \simeq \sigma_0 \mathcal{E}_e \frac{1}{1+i\frac{Dk^2}{\omega_r}}. \tag{73}$$

Finally, Equation (69) is replaced by

$$P_D = \frac{1}{2}\,\mathrm{Re}\,(J\mathcal{E}_e^*) \rightarrow P_D = \frac{1}{2}\sigma_0\mathcal{E}_0^2 \frac{1}{1+\left(\frac{\omega_D+\omega_c}{\omega_r}\right)^2}; \quad \omega_0 = Dk^2 \tag{74}$$

and

$$\frac{dE}{dt} = P_D\frac{\omega}{\omega_r} = \frac{\epsilon\mathcal{E}_0^2\omega}{L}\frac{\omega_r/\omega_c}{\left(1+\frac{\omega_D}{\omega_c}\right)^2+\left(\frac{\omega_r}{\omega_c}\right)^2}, \tag{75}$$

where we have used $\sigma_0 = \epsilon\omega_c$. (Equation (75) was used as the basis for Equation (18).)

Appendix II*—Amplification of Light by Cerenkov Electrons in a Solid

Since electrons drifting faster than the speed of light in a solid (i.e., Cerenkov electrons) can spontaneously emit light, we would also expect that they can coherently amplify light. The calculation presented below explicitly exhibits the expected amplification.

The relevant equations, written in MKS units, are the Maxwell Equations (76)-(79) and the Lorentz force Equation (80);

$$\nabla\cdot\vec{\mathcal{D}} = \epsilon\nabla\cdot\vec{\mathcal{E}} = \rho, \qquad (\vec{\mathcal{D}} = \epsilon\vec{\mathcal{E}}) \tag{76}$$

* The Appendixes to this paper were written by M. A. Lampert.

$$\nabla \cdot \vec{\mathcal{B}} = \mu_0 \nabla \cdot \mathcal{H} = 0, \qquad (\vec{\mathcal{B}} = \mu_0 \vec{\mathcal{H}}) \tag{77}$$

$$\nabla \times \vec{\mathcal{E}} = -\frac{\partial \vec{\mathcal{B}}}{\partial t} = -\mu_0 \frac{\partial \vec{\mathcal{H}}}{\partial t}, \tag{78}$$

$$\nabla \times \vec{\mathcal{H}} = \vec{j} + \frac{\partial \vec{D}}{\partial t} = \vec{j} + \epsilon \frac{\partial \vec{\mathcal{E}}}{\partial t}, \tag{79}$$

$$m\left(\frac{d\vec{v}}{dt} + \frac{\vec{v}}{\tau}\right) = e(\vec{\mathcal{E}} + \vec{v} \times \vec{\mathcal{B}}) = e(\vec{\mathcal{E}} + \mu_0 \vec{v} \times \vec{\mathcal{H}}). \tag{80}$$

Note that the ϵ in Equation (76) is the dielectric constant of the solid, at the light-wave frequency, in the absence of the conduction electrons. Also note that we have included a collision-induced friction term, in the usual manner, in the Lorentz-force equation.

The current density may be written

$$\vec{j} = en\vec{v} = \sigma\vec{\mathcal{E}}; \qquad \sigma = en\mu \text{ with } \mu = \vec{v}/\vec{\mathcal{E}}. \tag{81}$$

Finally, we have

$$\frac{d}{dt} = \frac{\partial}{\partial t} + \vec{v} \cdot \nabla. \tag{82}$$

In the absence of electron drift, the solid will support a uniform, transverse plane wave of the form

$$\vec{\mathcal{E}} = \hat{x}\mathcal{E} \exp i(\omega t - kz), \tag{83}$$

$$\vec{\mathcal{H}} = \hat{y}\mathcal{H} \exp i(\omega t - kz). \tag{84}$$

We now look for the same kind of solution in the presence of electron drift. Equation (76) is satisfied with $\rho \equiv 0$. Equation (77) is automatically satisfied. Equations (78) and (79) become, respectively,

$$k\mathcal{E} = \omega\mu_0\mathcal{H}, \tag{85}$$

$$k\mathcal{H} = (\omega\epsilon - i\sigma)\mathcal{E}. \tag{86}$$

Combining the two equations we get

$$k^2 = k_0^2 \left(1 - i \frac{\sigma}{\omega t} \right), \quad k_0^2 = \omega^2 \mu_0 \epsilon, \tag{87}$$

where k_0 is the propagation constant in the solid in the absence of conduction electrons.

Writing $\vec{v} = \vec{v_0} + v\hat{x} \exp i(\omega t - kz)$ and linearizing Equations (82) and (80), i.e., neglecting the product of a-c amplitudes, we obtain

$$\left[i(\omega - kv_0) + \frac{1}{\tau} \right] \vec{v} = \frac{e}{m} [\mathcal{E} - \mu_0 v_0 \mathcal{H}] \hat{x}. \tag{88}$$

Finally, substituting for $\mu_0 \mathcal{H}$ from Equation (85) into Equation (88) and using Equation (81) we obtain

$$\sigma = \sigma_0 \frac{1 - \dfrac{kv_0}{\omega}}{1 + c\omega\tau \left(1 - \dfrac{kv_0}{\omega_p} \right)}, \quad \sigma_0 = \frac{e^2 n_0 \tau}{m}, \tag{89}$$

where σ_0 is the d-c conductivity. Note that for nondrifting electrons, $v_0 = 0$, Equation (89) reduces to the well-known a-c conductivity.

Substitution of Equation (89) into Equation (87) gives the dispersion relation for the propagation. It is convenient now to separate k into its real and imaginary parts;

$$k = k_1 - ik_2. \tag{90}$$

Propagation is now described by

$$\vec{\mathcal{E}} = \hat{x}\mathcal{E} \exp i(\omega t - k_1 z) \exp(-k_2 z) \tag{91}$$

and likewise for $\vec{\mathcal{H}}$. Thus positive k_2 corresponds to attenuation, negative k_2 to growth.

Further, Equation (89) may be rewritten as

$$\frac{\sigma}{\sigma_0} = \frac{\left(1 - \frac{k_1 v_0}{\omega_p}\right) + i\frac{k_2 v_0}{\omega}}{(1 - k_2 v_0 \tau) + i\tau(\omega - k_1 v_0)}$$

$$= \frac{1 - \frac{k_1 v_0}{\omega}}{(1 - k_2 v_0 \tau)^2 + (\omega\tau)^2\left(1 - \frac{k_1 v_0}{\omega}\right)^2} + i\frac{\frac{k_2 v_0}{\omega}(1 - k_2 v_0 \tau) - \omega\tau\left(1 - \frac{k_1 v_0}{\omega}\right)^2}{(1 - k_2 v_0 \tau)^2 + (\omega\tau)^2\left(1 - \frac{k_1 v_0}{\omega}\right)^2}. \quad (92)$$

Separation of the dispersion relation into its real and imaginary parts gives the two equations:

$$\frac{k_1^2 - k_2^2}{k_0^2} = 1 + \frac{1}{\omega t_r}\frac{\frac{k_2 v_0}{\omega}(1 - k_2 v_0 \tau) - \omega\tau\left(1 - \frac{k_1 v_0}{\omega}\right)^2}{(1 - k_2 v_0 \tau)^2 + (\omega\tau)^2\left(1 - \frac{k_1 v_0}{\omega}\right)^2} \quad (93)$$

$$\frac{k_1 k_2}{k_0^2} = \frac{1}{2\omega t_r}\frac{1 - \frac{k_1 v_0}{\omega}}{(1 - k_2 v_0 \tau)^2 + (\omega\tau)^2\left(1 - \frac{k_1 v_0}{\omega}\right)^2}; \quad t_r = \frac{\epsilon}{\sigma_0} \quad (94)$$

where t_r is the well-known dielectric relaxation time.

Equations (93) and (94) are a pair of coupled algebraic equations in the unknowns k_1 and k_2. Letting $k_1 = 2\pi/\lambda$, we see from Equation (91) that the attenuation (growth) per wavelength is given by $\exp(-k_2\lambda) = \exp(-2\pi k_2/k_1)$. The simplest case to discuss is that of weak coupling, i.e., relatively slow attenuation (growth), $k_2 \ll k_1$, and a propagation characteristic very close to that in the solid in the absence of conduction electrons (second term on the right-hand side of Equation (93) small compared to unity). Then Equations (93) and (94) reduce to

$$k_1 = k_0 = \omega\sqrt{\mu_0\epsilon}, \quad v_w = \frac{\omega}{k_1} = \frac{1}{\sqrt{\mu_0\epsilon}} = \frac{c}{\sqrt{\epsilon/\epsilon_0}}, \quad (95)$$

$$\frac{k_2}{k_1} = \frac{1}{2\omega t_r} \frac{1 - \dfrac{v_0}{v_w}}{\left(1 - \omega\tau \dfrac{k_2 v_0}{k_1 v_w}\right)^2 + (\omega\tau)^2 \left(1 \dfrac{v_0}{v_w}\right)^2}. \tag{96}$$

It is immediately clear from Equation (96) that for

1. $v_1 = v_w$, $k_2 = 0$ and there is no interaction of the light wave with the synchronously drifting electrons. This is expected since, for the unperturbed light wave, the Lorentz force $\vec{\mathcal{E}} + \vec{v}_0 \times \vec{\mathcal{B}} = \vec{\mathcal{E}} + \vec{v}_w \times \vec{\mathcal{B}} = 0$.

2. $v_0 > v_w$, $k_2 < 0$ and the light wave is amplified. In particular, for $v_0 = 2v_w$ Equation (96) becomes approximately

$$k_2 = \frac{\sqrt{\epsilon/\epsilon_0}}{2ct_r(\omega\tau)^2}, \tag{97}$$

which is numerically just the expression for absorption of light by free carriers but with reversed sign, indicating amplification of the light wave. For larger values of v_0, k_2 decreases as $1/v_0$. Hence the behavior for light waves completely parallels that for acoustic waves.

ADSORPTION-TYPE RESERVOIR FOR GAS TUBES

By

K. G. Hernqvist and J. D. Levine

RCA Laboratories
Princeton, N. J.

Summary—A new type of reservoir for metallic-vapor tubes is described. The reservoir consists of atoms of the vapor adsorbed on the surfaces of a highly porous material. The adsorbent can be in the form of an assembly of spherical particles of a material such as tungsten or alumina powder sintered to form a sponge-like structure. Design criteria for such a reservoir are established. The application of adsorption storage of cesium for thermionic converters is discussed.

Introduction

THE EFFICIENT operation of gaseous discharge devices, such as fluorescent lamps and thermionic converters, requires specified gas or vapor pressures. In such devices, however, there is inevitably a loss of gaseous materials during the life due to a variety of causes, e.g., "clean-up," irreversible adsorption, and chemical effects. It is common practice to provide a gas reservoir to prolong the life of such gas tubes. Different types of reservoirs are used for different gases. For example, hydrogen thyratrons are provided with an *absorption* type of reservoir[1] where hydrogen is stored in a chemical compound (titanium hydride) and released upon heating. In metallic-vapor discharge tubes, such as thermionic converters[2] and mercury-vapor lamps, a liquid metal pool is usually provided as a means of vapor storage. It is well-known that such a liquid pool accumulates at the coldest part of the envelope and that the vapor pressure is controlled by the pool temperature. This liquid storage provides an almost inexhaustable supply of vapor for a relatively small storage volume and weight. It has several drawbacks, however, such as the need for separate and accurate temperature control, mechanical instability of the pool (important in space applications), and a relatively steep pressure-versus-temperature relation. This paper discusses an alternative

[1] S. Goldberg and J. Rothstein, *Advances in Electronics and Electron Physics*, Vol. 14, p. 211, Acad. Press, New York, 1961.

[2] V. C. Wilson, *Energy Conversion for Space Power*, p. 137, Acad. Press, New York, 1961.

method of storage suitable for metallic-vapor-discharge devices. In this method, the atoms are stored in *ad*sorbed form on an adsorbate having a relatively large surface area. The application of this method to storage of cesium in thermionic converters is described.

Principle of Operation

When liquid-pool storage is used in a metallic-vapor-discharge tube, the vapor pressure p is determined by the normal vaporization temperature T_v according to the well-known relation[3]

$$p = K_v \exp\left\{\frac{-\phi_v}{kT_v}\right\} \tag{1}$$

where K_v depends only weakly on temperature, ϕ_v is the heat of vaporization of the metal from its own liquid, and k is the Boltzmann constant.

Assume that such a device is suddenly provided with a large surface area of a substrate such that $\phi_a > \phi_v$ where ϕ_a is the heat of adsorption of the vapor atom on the substrate. To reach equilibrium, the pool will tend to vaporize and the atoms will be transferred and stored in adsorbed form[4] on the surface area of the substrate, which now serves the role of reservoir. The pressure will ultimately be determined by

$$p = K_a \exp\left\{\frac{-\phi_a}{kT_a}\right\} \tag{2}$$

where T_a is the temperature of the adsorption reservoir. The approximate condition necessary for the pool to transfer atoms to the adsorption reservoir is

$$\frac{\phi_a}{T_a} > \frac{\phi_v}{T_v}. \tag{3}$$

Equations (1) and (2) are plotted schematically in Figure 1. By proper choice of the adsorbate, ϕ_a can be chosen to give a predetermined temperature relation according to Equation (2). Thus, a new type of reservoir is provided where the atoms are stored in adsorbed

[3] S. Dushman, *Scientific Foundations of Vacuum Technique*, p. 740, John Wiley & Sons, New York, 1958.

[4] J. D. Levine and E. P. Gyftopoulos, *Jour. Surface Sci.*, Vol. 1, p. 171, 1964.

form. Here the liquid pool has been eliminated and a wider choice of operating conditions has been provided. The area of the reservoir must be large enough so that the number of atoms stored is large compared to the number of atoms normally present in the device (in the gas phase as well as adsorbed on other device surfaces). A method of providing such an adsorbate, with a minimum of weight and volume, is described in the next section.

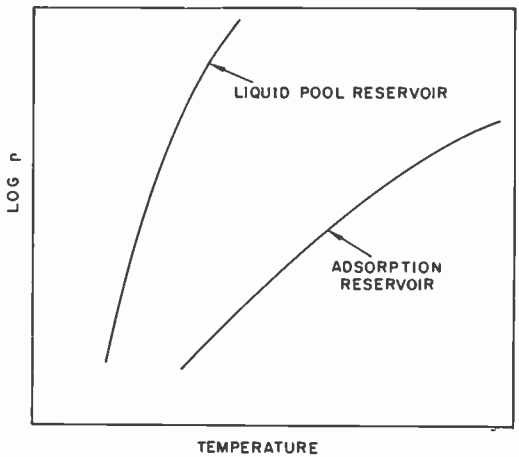

Fig. 1—Curves showing relation between vapor pressure p and temperature for vaporization reservoir and for adsorption reservoir.

Design Criteria

To obtain a large surface-to-volume ratio for an adsorption-type reservoir, an assembly of closely packed spherical particles is desirable. In practice, such an assembly of particles (e.g., tungsten or alumina powder) may be sintered together to form a sponge-like structure. Consider an assembly of spherical particles with diameter d in a cubic close-packed array. The ratio between surface area and the volume enclosed by the outer layer of particles is $\sqrt{2}\pi/d$. For a particle diameter of 1 micron, total reservoir surface area is 4×10^4 cm^2 per cubic centimeter of sponge volume. Let the density of adsorbed atoms on the particle surface be defined as $\sigma\,\theta$ where σ is the density of atoms at one monolayer coverage and θ is the fractional coverage. The total number of stored atoms in the adsorption reservoir is

$$N_{res} = \sigma\theta V_{res}(\sqrt{2}\pi/d) \tag{4}$$

where V_{res} is the actual reservoir volume.

The reservoir volume needed depends on the characteristics of the particular device and the storage safety factor chosen. In general, N_{res} should be made much larger than the number of atoms used up during the normal life of the device.

Pressure–Temperature Characteristics

In the adsorption reservoir concept, there are many more atoms located on surfaces of the adsorption reservoir than in the volume or on the device walls. The fractional coverage, θ, on reservoir surfaces is then fixed (due to conservation of atoms) and is invarient with respect to temperature. In other words, pressure–temperature relations are equivalent to lines of constant θ (isoteres).

To calculate isoteres, it is necessary only to review the theoretical equations previously established for this purpose.[4-6] The pressure can be expressed in terms of the desorption rate E, surface temperature T, and atomic mass m, by the standard relationship

$$p = \frac{E}{\sqrt{2\pi\, mkT}}. \tag{5}$$

The desorption rate is given by[5]

$$E = wv\sigma\theta \exp\left\{\frac{\Delta S}{k}\right\} \exp\left\{\frac{-\phi_a}{kT}\right\}, \tag{6}$$

where w is the statistical weight of the adsorbate, v is the vibration frequency perpendicular to the surface, and ΔS is the configuration entropy change.

In the case of cesium on transition metals, it is a good approximation[5] to set $w = 1$, $v = 10^{12}$ sec^{-1}, and $\sigma = 4.8 \times 10^{14}$ cm^{-2}. Theoretical analysis[5] of the ΔS term shows it to be approximately linear with θ and independent of T and the material. It is tabulated as a function of θ in Table I. The desorption heat ϕ_a decreases with increasing θ and depends on adsorbate and substrate materials. It can be theoretically predicted[4,6] for many metallic adsorbates and substrates using Pauling's electronegativity concepts. Values of ϕ_a as a function of θ

[5] J. D. Levine and E. P. Gyftopoulos, *Jour. Surface Sci.*, Vol. 1, p. 225, 1964.

[6] E. P. Gyftopoulos and J. D. Levine, "Work Function Variation of Metals Coated by Metallic Films," *Jour. Appl. Phys.*, Vol. 33, p. 67, Jan. 1962.

has been found[7] that cesium is lost by diffusion and trapping in the grain boundaries of metals and by chemical reactions with impurities. It has been observed that such losses may amount to as much as ten times the number of cesium atoms normally present in the vapor phase and in adsorbed form on envelope and electrodes. Thus, for long life, the reservoir should hold at least 10 to 100 times this number of cesium atoms.

The amount of cesium normally present in a thermionic converter can easily be estimated. Consider an idealized thermionic converter,[8]

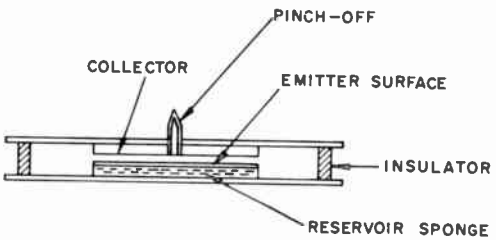

Fig. 4—Schematic drawing showing incorporation of adsorption reservoir for thermionic converter.

shown in Figure 4, consisting of two metal electrode discs (emitter and collector) closely spaced. Each disc has an area A. Insulators and support structure occupy but little area and volume, and may be neglected in this consideration. Assume that the converter operates at a pressure p and with a cesium coverage near unity ($\theta \sim 1$) on both electrodes. The number of cesium atoms adsorbed on both disc areas is $N_{surf} \sim 10^{15} A$. The number of atoms in the volume is $N_{vol} \sim 3 \times 10^{16} plA$, where p is the pressure in torr and l is electrode separation in centimeters. The criteria for having the adsorption-type reservoir dominate the device behavior is

$$N_{res} \gg N_{surf} + N_{vol} \tag{8}$$

To estimate the minimum required adsorption reservoir volume, assume $N_{res} = 100 \times (N_{surf} + N_{vol})$, $p = 1$ torr, $l = 0.025$ cm, $A = 100$ cm^2, and $d = 10$ microns. Then $N_{surf} \sim 10^{17}$, $N_{vol} \sim 10^{17}$ and $N_{res} \sim 1.5 \times$

[7] W. Harbaugh, F. G. Block, and A. Basiulis, Paper No. 65-472 of the *AIAA 2nd Ann. Mtg.*, San Francisco, Calif., July 26-29, 1965.

[8] K. G. Hernqvist, "Energy Conversion Techniques," *Proc. IRE*, Vol. 50, p. 1285, May 1962.

10^{19} V_{res} (from Equation (3) with $\theta = 1$). For a storage factor of 100, V_{res} must be approximately 1 cm^3. This value is acceptable for storage volume in a device of the assumed size.

If the adsorption reservoir consists of a sintered molybdenum sponge, the scope of pressure–temperature relationships can easily be found from Figure 2. For example, at $T = 1200°K$ and $p = 1$ torr, the invarient coverage, θ, is 0.51.

Experimentally, a predetermined coverage may be obtained in the following manner. The converter is provided with an external cesium pool or operated on a cesium still[9] from which it can be separated after cesium dosing. The converter, including the adsorption reservoir, is brought to its operating design temperatures and the external pool temperature is adjusted to give the desired pressure. After equilibrium is established, the converter is pinched off from the external pool section. Thereafter the adsorption reservoir serves as the proper reservoir provided the converter elements operate at or near design temperatures. No part of the converter should operate at a temperature much below the normal condensation temperature corresponding to the operating pressure. This will assure that no liquid pools are allowed to form anywhere.

The adsorption reservoir thus can be thermally associated with any part of the converter or it can have its own temperature control. The first alternative is particularly attractive if parts of the converter are normally operated within narrow temperature ranges, which is usually the case for the emitter or the collector or both. Thus, if the converter is operated at a constant heat-source temperature, the reservoir may become a permanent part of the emitter as shown in Figure 4. This arrangement simplifies operation of the converter to the point where it resembles a solid-state thermocouple.

Practical realization of a separately heated adsorption reservoir has also been accomplished in a cesium-vapor-type thermionic converter using a sintered molybdenum sponge.[10]

In certain applications it may be desirable to use two or more adsorption reservoirs. The p-T relationship must then be solved graphically from Figures 2 or 3. For any number of reservoirs at any temperatures, the constraints are (a) the sum of adsorbed atoms on all reservoir surfaces must be conserved and (b) the pressure through-

---

[9] J. R. Fendley, Jr., "Continuous Pumping of Cesium Vapor Devices," *Rev. Sci. Instr.*, Vol. 35, p. 905, July 1964.

[10] Private communication by F. G. Block, RCA Electronic Components and Devices, Lancaster, Pa. Work performed under AEC Contract No. AT(30-1)-3429.

out the envelope must be uniform. As an example of this kind of calculation, consider the realistic task of automatically tracking p with T so that power density or efficiency is maximized even though T may fluctuate. In other words, a predetermined p-T slope would give optimum device performance. Adsorption-reservoir conditions necessary to meet this slope requirement can be predicted graphically using the theory of this paper.

SOLAR-PUMPED MODULATED LASER*

By

C. W. Reno

RCA Defense Electronic Products
Camden, New Jersey

Summary—*Solar-pumped modulated lasers show great potential for deep space communications. This paper describes the solar pumping and modulation of $CaF_2:Dy^{2+}$, $YAG:Nd^{3+}$, and $YAG:Nd^{3+}:Cr^{3+}$ lasers. The inherent advantages and disadvantages of each laser are described. The transmission of a television picture using a gallium arsenide electro-optic modulator and a solar pumped $YAG:Nd^{3+}$ laser is reported.*

Introduction

SOLAR PUMPING of a laser was first reported by Kiss, Lewis, and Duncan at RCA Laboratories early in 1963.[1] A comparison of solar pumping of a laser and pumping by a broadband source (i.e., a tungsten lamp) reveals that solar pumping is attractive for spacecraft laser systems. For example, to achieve a power output of one watt, a laser pumped by a broad-band source in an "efficient" ellipse requires a lamp input power well in excess of 1 kilowatt. Solar cells providing this amount of input power would require about 100 square feet of active collection area. Add to this the disadvantages of weight, cooling requirements, and lamp replacement using a broad-band source, and the solar-pumped laser becomes quite attractive. It is expected that a solar-pumped $YAG:Nd^{3+}$ laser using a 31-inch parabolic mirror collector with a focal length of 21 inches will provide a 1-watt power output in use on earth at the present state of the art.

Laser Materials

A solar pumping system was assembled and three laser materials, $CaF_2:Dy^{2+}$, $YAG:Nd^{3+}$ and $YAG:Nd^{3+}:Cr^{3+}$, were evaluated. These materials are attractive for solar pumping because of their relatively broad absorption bands[2,3] (see Figure 1).

* Work performed under NASA contract NAS 9-3671.

[1] Z. J. Kiss, H. R. Lewis, and R. C. Duncan, "Sun Pumped Continuous Optical Maser," *Appl. Phys. Letters*, Vol. II, p. 93, 1 March 1963.

[2] J. Wittke et al., "Solid State Laser Exploration," Technical Report AFAL-TR-64-334.

[3] R. J. Pressley, private communication.

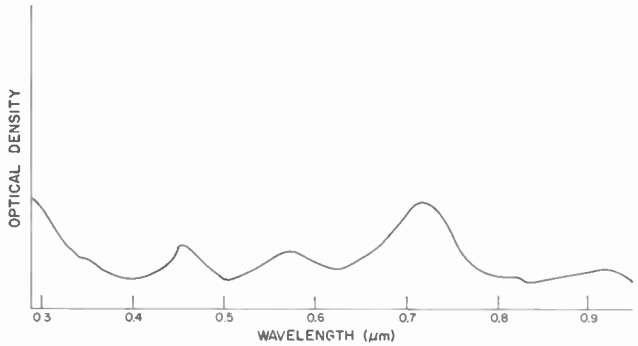

a. $CaF_2:Dy^{2+}$

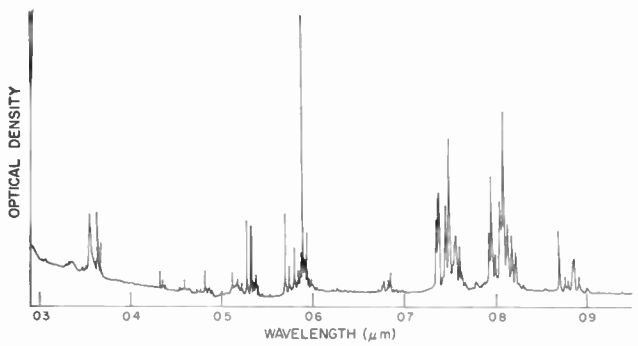

b. $YAG:Nd^{3+}$

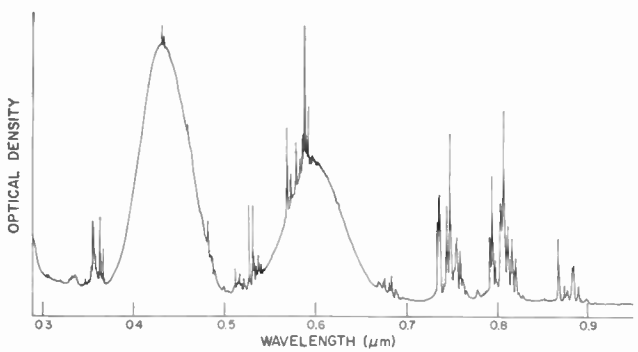

c. $YAG:Nd^{3+}:Cr^{3+}$

Fig. 1—Absorption spectra of laser crystals.

Most of the excitation in $CaF_2:Dy^{2+}$ occurs from pumping in the bands from 5000 to 8000 angstroms. This is well matched by the solar spectrum. As shown in Figure 2, the laser transition in $CaF_2:Dy^{2+}$ takes place between two triply degenerate states, $^1T_1^{(2)}(^5I_7) \rightarrow T_2^{(2)}(^5I_8)$. Laser output occurs at 2.36 microns. This transition has a fluorescent line width of 0.3 cm^{-1} at 77°K, the highest feasible operating temperature because of thermalization of the lower laser state and broadening of the fluorescent line width. For a magnetic field in the [100] direction, the fluorescent line due to the allowed

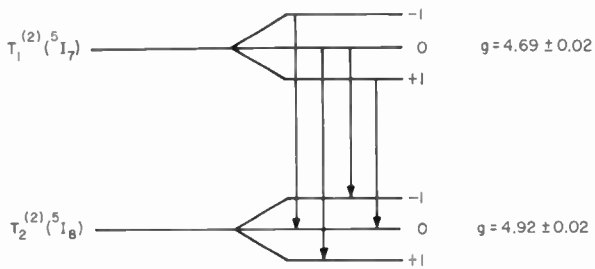

Fig. 2—Zeeman splitting of laser line in $CaF_2:Dy^{2+}$ showing allowed ($\Delta M = \pm 1$) transitions for [100] orientation of magnetic field.

transitions splits with an effective g of 9.6, corresponding to 4.5×10^{-4} cm^{-1} $gauss^{-1}$. Hence, the fluorescent line width can be doubled using a 600-gauss field. In this fashion,[4] magnetic modulation is easily introduced.

Pumping in $YAG:Nd^{3+}$ occurs principally in sharp lines at 6000, 7500, and 8000 angstroms. These lines all lie well within the broad peak in solar energy occurring in the visible and near infrared, making the sun quite a good pump source for this device. The laser transition occurs from the $^4F_{3/2}$ state to the $^4I_{11/2}$ state with a fluorescent line width of 2 cm^{-1}. This relatively wide fluorescent line width and a low effective g make magnetic modulation impractical. The laser wavelength is 1.06 microns.

With $YAG:Nd^{3+}:Cr^{3+}$, pumping can be accomplished by either of two mechanisms.[3] First, pumping can be at the same fluorescent lines as for $YAG:Nd^{3+}$. Second, cross pumping can be used through the broad Cr^{3+} to the Nd^{3+} absorption bands and the ^3E state of Cr^{3+} to the Nd^{3+} laser state, which Kiss[5] has demonstrated to exist.

[4] Z. J. Kiss, "Zeeman Tuning and Internal Modulation of the $CaF_2:Dy^{2+}$ Optical Maser," *Appl. Phys. Letters*, Vol. 3, p. 145, 2 Nov. 1963.

[5] Z. J. Kiss and R. C. Duncan, "Cross Pumped Cr^{3+}-Nd^{3+}:YAG Laser System," *Appl. Phys. Letters*, Vol. 5, p. 200, 15 Nov. 1964.

However, there is a long transfer time ($\approx$1 millisecond) for energy transfer between the ^3E state of Cr^{3+} and the Nd^{3+} laser state.

Based on our tests of these materials the following major advantages were found:

(1) *$CaF_2:Dy^{2+}$*

a. Magnetic modulation can be used with this material, providing ease in modulation up to 300 kilocycles. No losses are introduced due to external modulators.

b. Extremely low thresholds are possible due to the narrow laser line of $CaF_2:Dy^{2+}$.

(2) *$YAG:Nd^{3+}$*

a. This material can be operated at 300°K (room temperature) as opposed to 77°K for $CaF_2:Dy^{2+}$.

b. The laser output at 1.06 microns allows use of detectors (i.e., multiplier phototubes and silicon photocells) unusable with $CaF_2:Dy^{2+}$.

c. The output has little spiking compared to $CaF_2:Dy^{2+}$ and $YAG:Nd^{3+}:Cr^{3+}$.

(3) *$YAG:Nd^{3+}:Cr^{3+}$*

a. Lasing properties are the same as $YAG:Nd^{3+}$.

b. Broad absorption bands add greatly to the effective pumping through efficient energy transfer.

Thus it may be seen that for applications where cryogenic cooling is unavailable or impractical, one of the YAG laser systems must be used. Because $YAG:Nd^{3+}:Cr^{3+}$ exhibits a noisy output, $YAG:Nd^{3+}$ was used for modulation experiments described here.

Experimental Apparatus and Results

The experimental apparatus for solar pumping $CaF_2:Dy^{2+}$, shown in Figure 3, includes a 31-inch-diameter parabolic dish (21-inch focal length) affixed to an equatorial mount and a cylindrical lens that extends the solar image over a large portion of the crystal. The equatorial mount, tracking with a clock drive, allows stable operation over extended periods. Operation in excess of half an hour has been achieved with the principal difficulty being a gusty wind. With the equatorial mount, solar power is focused to a 3/16-inch spot at the focus of the mirror and has been found, by test measurements, to be as high as 60 milliwatts per square centimeter. Thus the 31-inch diameter mirror collects 290 watts, of which approximately 80 per cent, or 232 watts, is focused.

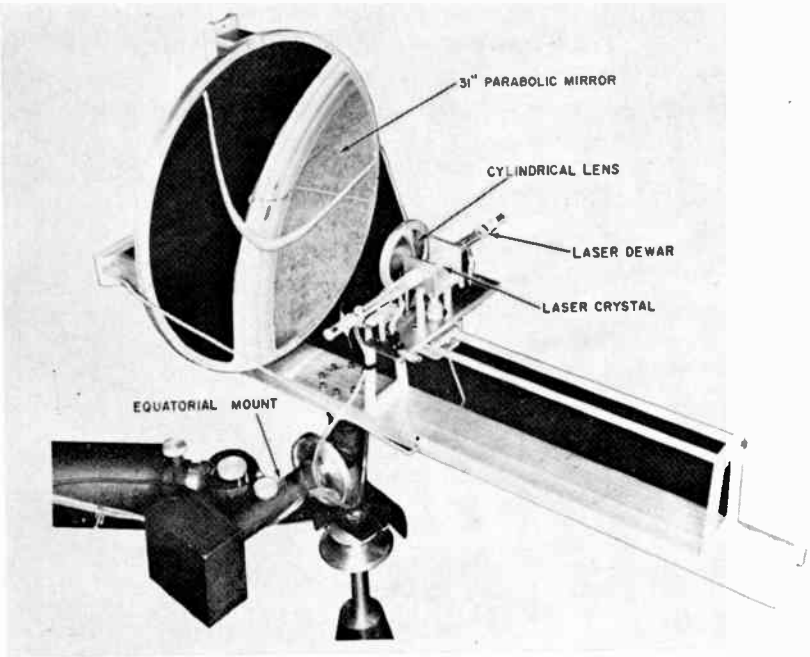

Fig. 3—Equational mount with dish and Dewar mounted for solar pumping $CaF_2:Dy^{2+}$.

$CaF_2:Dy^{2+}$

As $CaF_2:Dy^{2+}$ is not a true 4-level laser system at 68°K, it is necessary to pump as large a portion of the laser as practical to reduce absorptive losses in the unpumped volume. In this experimental setup, sub-cooled liquid nitrogen was allowed to flow through the Dewar that holds the laser at the focus of the parabola. An InAs photodiode was used to detect the lasing output. Continuous operation was achieved with about 30 per cent ripple.

Amplitude modulation was achieved by placing the crystal in a varying magnetic field.[4] The desired field was established by two coils (see Figure 4). Coil A was activated using a d-c current of about 10

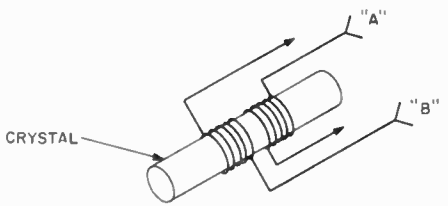

Fig. 4—Physical arrangement of coils and crystal for magnetic modulation.

amperes to split the laser line and bias the laser off. Coil B was energized with 5-ampere, 5-microsecond pulses at the required rate for modulation. Figure 5 shows typical modulation. Voice was transmitted by using this technique and varying the pulse rate.

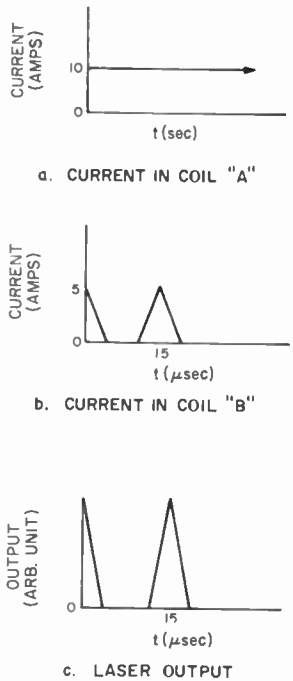

Fig. 5—Magnetic modulation.

YAG:Nd^{3+}:Cr^{3+}

Because of the very broad pump bands added by the Cr^{3+} cross pumping, this crystal was expected to be the most efficient of the lasers tested. Unfortunately, this material had such a large ripple on its d-c output that it was unusable for electro-optic modulation.

Continuous operation was easily achieved using end pumping. This configuration was chosen over side pumping because the small size of the image is well matched to the crystal end. Since side walls of the flow tube are reflective, a uniform brightness is achieved throughout the length of the flow tube (neglecting the absorption of the crystal) allowing a long effective path through the crystal volume for the pump light. End pumping in this manner allows much greater absorption

than does side pumping. As the Nd^{3+} doped lasers are 4-level systems, inhomogeneous pumping does not degrade performance. Threshold was 100 watts collected by the mirror, or 25 watts coupled to the crystal (because of the mismatch between crystal and solar image, only about 25% of the light is coupled into the laser crystal). The laser was pumped using the flow tube shown in Figure 6. This arrangement

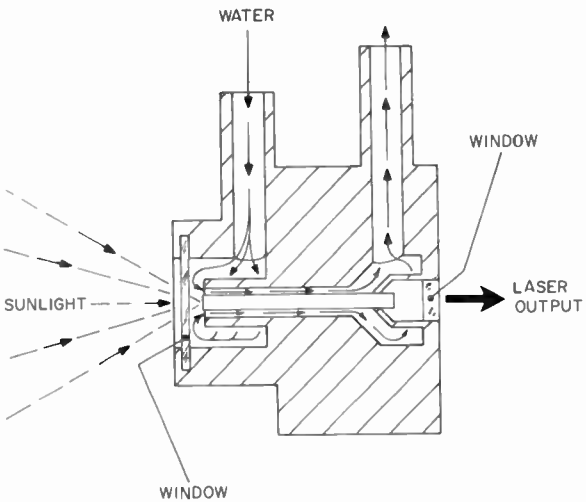

Fig. 6—Flow tube for YAG lasers.

allows water to flow over the crystal sides and provides complete access to the crystal end for pumping. Laser output is taken from the end opposite the pumping end. An output power of 100 milliwatts was observed for this nonoptimized system.

YAG:Nd^{3+}

Excellent continuous operation was achieved in confocal-ended crystals with the output "quiet" enough for modulation experiments, although some spiking was observed. For a crystal 0.094 × 1.5 inches, the threshold was 100 watts collected by the mirror, or about 25 watts into the laser crystal. This crystal was operated using the same physical setup as the double-doped YAG laser. Maximum power output achieved was 100 milliwatts.

Electro-Optic Modulation

Electro-optic modulation was used to transmit the picture shown

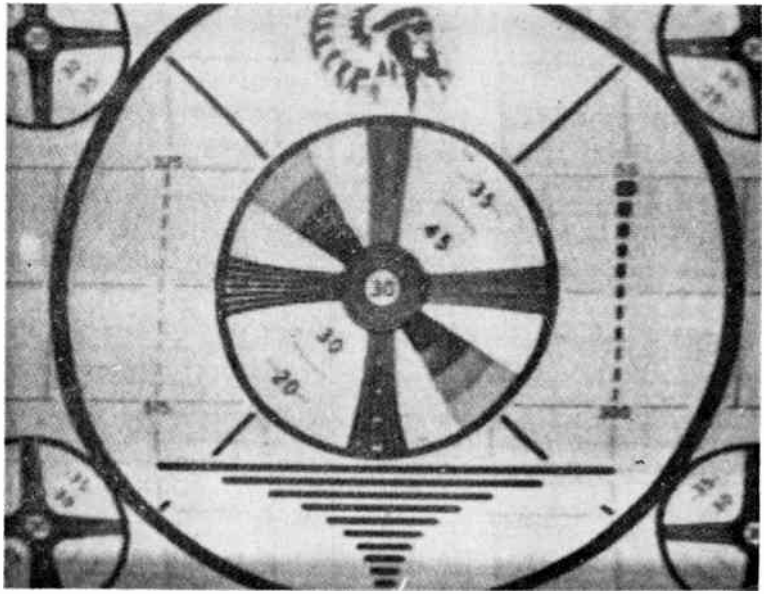

Fig. 7—Test pattern transmitted using electro-optic modulation of YAG:Nd^{3+} solar pumped laser.

in Figure 7. About 40% modulation was achieved using a GaAs crystal* and an applied voltage of 600 volts peak-to-peak.

Figure 8 shows the major components of the optical communication system. The polarizer permits light polarized in only one plane to

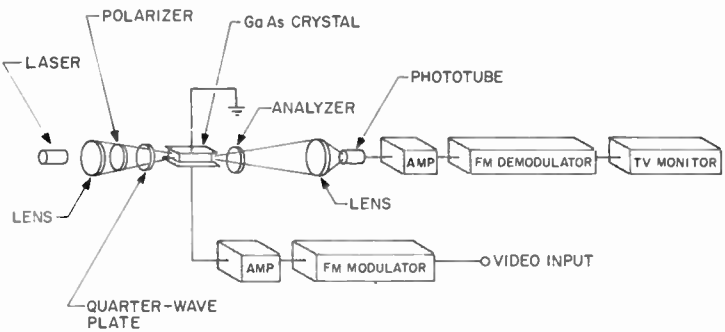

Fig. 8—Optical television communication system.

* Until recently, good optical quality, large cubic crystals having large electro-optic coefficients were unavailable. The GaAs crystals used here were obtained from RCA Semiconductor and Materials Division, Somerville, N. J.

reach the crystal. As the plane-polarized light passes through the crystal, it becomes elliptically polarized, the amount of ellipticity varying as a function of the voltage applied to the crystal. Since the analyzer transmits light polarized in only one plane, the intensity of the light transmitted through the modulator varies as the rotation of the polarization produced by the crystal, providing amplitude modulation.

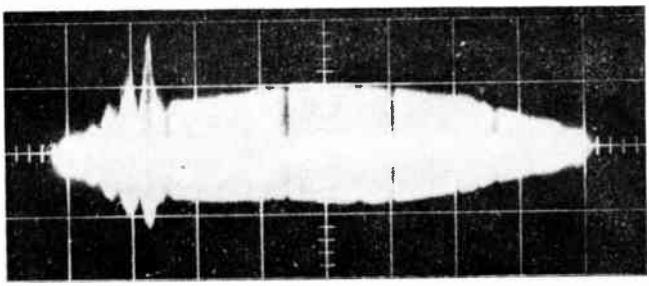

Fig. 9—Frequency response of GaAs crystal (markers are at 1, 3, 5 and 7 mc).

One major problem arises—piezoelectric resonances occur in the modulator material below 1 mc. Figure 9 shows this effect in the swept response of a GaAs electro-optic modulator system. However, the modulation spectrum can be shifted away from these perturbations by the use of FM subcarrier modulation, thereby avoiding signal distortion. This method was used to transmit the picture in Figure 7.

CONCLUSIONS

It has been shown experimentally that solar-pumped modulated lasers can operate efficiently and that modulation bandwidths in excess of 6 mc can be realized. Further refinements in the manufacture of laser crystals and optimization of pump-power-collection systems are expected to make possible practical communication systems employing solar-pumped lasers.

LOW-POWER LONG-RANGE DIGITAL COMMUNICATIONS SYSTEM

By

J. G. Arnold,* D. M. Chauvin,** J. C. Johnson,† and J. K. Oliver, Jr.*

Summary—A long-range digital communication system based on the use of a very low power narrow-bandwidth portable transmitter and a fixed-station receiver is described. The system operates with a bandwidth of approximately 1 cps and has a bit rate of 3 bits per minute. The transmitter, which employs a temperature-controlled quartz crystal oscillator, has a power output of approximately 100 milliwatts and operates on a nominal battery voltage of 9 volts. The receiving system is composed of a high-frequency communications receiver plus a developed third conversion intermediate frequency, filtering, and decision circuitry. The narrowband channel has an effective noise bandwidth of 0.75 cps. Tests conducted to determine system feasibility showed that Doppler shifts greater than 0.75 cps were, at most, infrequent. In a series of transmissions over distances of up to approximately 2000 miles, a signal-to-noise ratio of better than 30 db was consistently achieved.

Introduction

IN ANY successful communications system, noise is reduced by limiting the bandwidth to that necessary for the signal being used. Since noise power is proportional to the received bandwidth, i.e., $e_n^2 \simeq KTB$, a minimizing bandwidth will result in a minimal noise level. The required receiver bandwidth is usually determined by the additive effects of information rate (signal spectrum width) and system instability.

A system operating on an extremely narrow bandwidth, say 1 cps, would permit exceptional receiver sensitivities since the noise within the bandwidth all but disappears. However, the rate at which information could be transmitted by such a system is extremely low—one bit per second for a 1 cps bandwidth. Also, the stability requirements are very severe. For a 1 cps bandwidth at 10 megacycles, a stability of one part in 10^7 is required for both receiver and transmitter.

An inherent limitation, when using high-frequency ionospheric

* Formerly RCA Communications Systems Division, Tucson, Ariz., presently with Bell Aerosystems Laboratory, Tucson, Ariz.

** Formerly RCA Communications Systems Division, Tucson, Ariz., presently with Autonetics, Div. of North American Aviation, Anaheim, Calif.

† Formerly RCA Communications Systems Division, Tucson, Ariz., presently with Motorola, Western Military Division, Scottsdale, Ariz.

propagation, is the Doppler shift in a received frequency that results when the rate of change of phase of the signal is not constant with time. This shift is caused by two factors: (1) a change in the effective height of the ionospheric layer and (2) a variation with time of the electron density of the ionospheric layer over the propagation path.

While extremely low information rates are not attractive for most communications systems, there are applications where such rates can be tolerated in order to permit the use of extremely low transmitted power. For example, a pocket-size transmitter might enable a downed pilot to report his position. An experimental system suitable for such use is described.

Experimental System

The order of magnitude of the ionospheric Doppler shift has been studied by various workers.[1-5] Shifts of 0.1 to 0.4 cps may normally be expected at operating frequencies of 4 to 15 mc, with occasional shifts of up to 5 cps during solar flares. For our experiments, one-hop transmissions in the 10 to 20 mc range over distances of 1000 to 3000 miles were to be studied. Calculations indicated that we could expect the Doppler shift to be no more than 0.5 cps.

From the Doppler shift considerations alone, the system should be designed for operation with a bandwidth somewhat greater than 0.5 cps. A bandwidth of 1 cps was chosen. This seemed to be, at the onset, about the minimum that could be realized using relatively simple filters. (Actually, the filters developed for the system proved to have a noise bandwidth of about 0.75 cps—see Figure 3.) This means that at a 10-mc operating frequency, the system stability must be better than 1 part in 10^7. Stability in this order of magnitude is quite realizable for fixed station equipment, but for a small portable transmitter it is virtually out of the question. In the system developed, the transmitter exhibited a relatively long (one week) stability of better than

---

[1] K. Davies, "Doppler Studies of the Ionosphere with Vertical Incidence," *Proc. I.R.E.*, Vol. 50, p. 94, Jan. 1962; June 1962, p. 1544.

[2] J. M. Kelso, "Doppler Shifts and Faraday Rotation of Radio Signals in a Time Varying, Inhomogeneous Ionosphere," *Jour. Geophysical Research*, Vol. 65, p. 3909, Dec. 1960.

[3] J. V. Evans, *Journal of Atmospherics and Terrestrial Physics*, Vol. 11, pp. 259-271; 1957.

[4] T. Ogawa, S. Ando, A. Yoshida, "Vertical Incidence Doppler Ionogram," *Proc. I.R.E.*, Vol. 49, p. 643, Mar. 1961.

[5] I. Takahashi, T. Ogawa, M. Yamano, A. Hirai, M. Takiuchi, "Doppler Shift of the Received Frequency from the Standard Station Reflected by the Ionosphere," *Proc. I.R.E.*, Vol. 45, p. 1408, Oct. 1957.

1 part in 10^6. In order to obtain an effective stability of better than 1 part in 10^7, the bit rate was sacrificed from the maximum of 60 bits per minute to 3 bits per minute. This was done by sweeping the transmitter over a 20-cps range to ensure that the 1-cps receiver bandwidth was illuminated by each bit. To permit a build-up of energy in the bandpass, the sweep rate could not exceed 1 cps per second. Therefore, each sweep required 20 seconds or 3 sweeps per minute. For the experimental system, carrier frequencies between 13 and 16 mc were chosen.

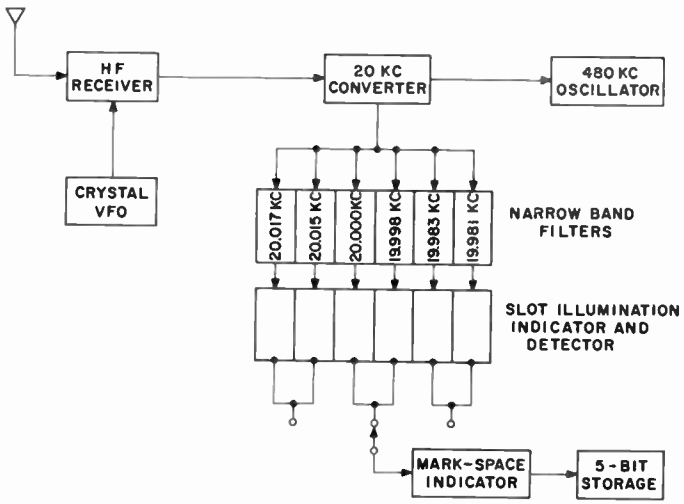

Fig. 1—Block diagram of receiving system.

Receiver

The receiving system is shown in Figure 1. The basic component is the narrowband filter. A high-Q crystal with a 20-kc series resonance was found very effective for the required filtering. In this receiver, two bridge circuits, as shown in Figure 2, were cascaded to obtain the filter selectivity shown in Figure 3. The simplicity and effectiveness of this arrangement was impressive.

The receiving system was composed of a high-frequency communications receiver plus a developed third conversion intermediate frequency, filtering, and decision circuitry. A 5-bit memory and display were also provided for convenience. The 500-kc intermediate frequency was derived from a commercial communications receiver. The required stability was achieved by substituting a crystal-controlled oscillator

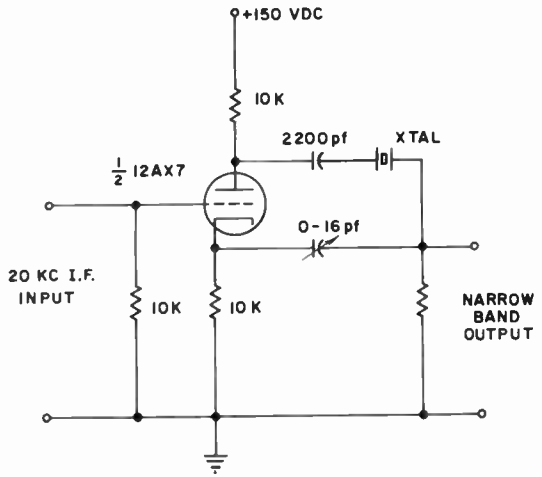

Fig. 2—Narrow-band filter.

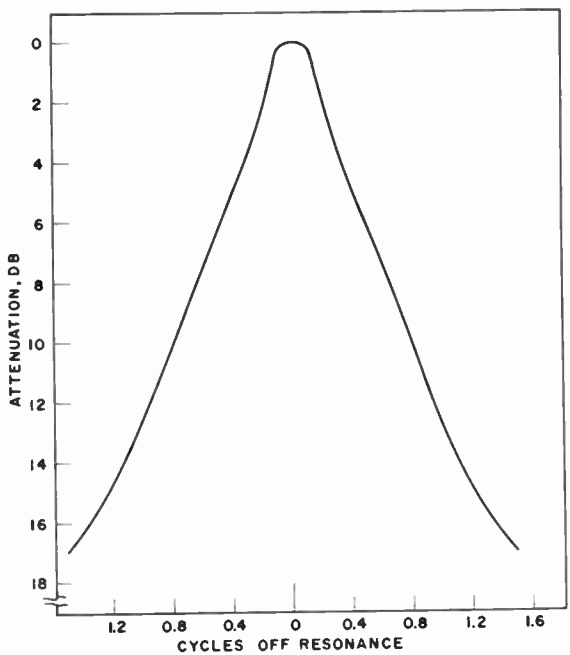

Fig. 3—Narrow-band-filter response.

for the variable frequency oscillator. The 500-kc signal was then converted to the 20-kc intermediate frequency, which provided a band pass of about 60 cps. Some peak limiting was allowed to occur in this intermediate frequency strip, thereby reducing impulse noise considerably. The 20-kc intermediate frequency output was fed into six parallel-connected narrow-band crystal filters. The frequency spacing of the filters was such that at least one of the three pairs would be illuminated by the transmitted signal even if it should be as much as 50 cps off frequency. The spacing used is shown in receiver block diagram, Figure 1.

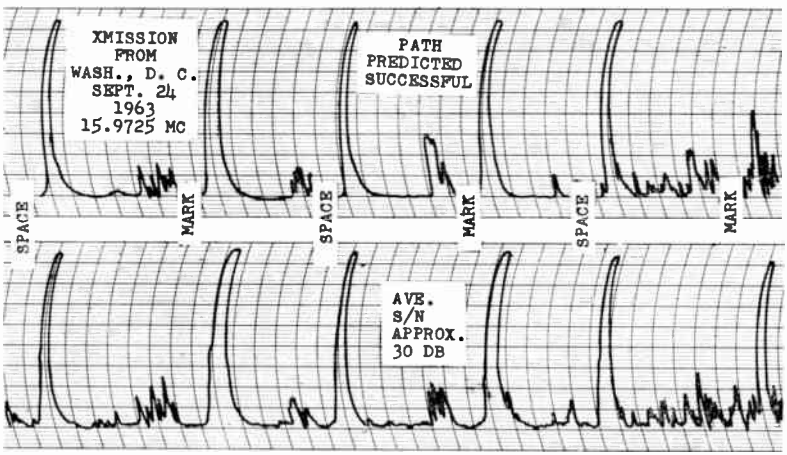

Fig. 4—Typical received signal (using dual-channel recorder).

Neon indicators were provided on the output of each filter detector. The illumination of any of the six narrow channels could thus be observed on the front panel of the receiver. The mark–space sense could be visually derived by observing the sequence of the lights or by the output of the decision circuitry. In addition, envelope detectors and a pen recorder were used to monitor the filter pair being used. This provided a permanent record and was found to be most advantageous in visual interpretation. Figure 4 shows the recorder output. As can be seen in these recordings, an observation of the sequence of channel illumination gives the bit sense.

Transmitter

Figure 5 shows the transmitter. The main case contains the complete transmitter with batteries, except for the oscillator, which is

assembled in the small case. Several distinct features were incorporated into the transmitter oscillator in order to achieve the high degree of stability required. This requirement suggested the use of a temperature-controlled quartz crystal as the stable element. However, the use of an oven would have been prohibitive in regard to power, size,

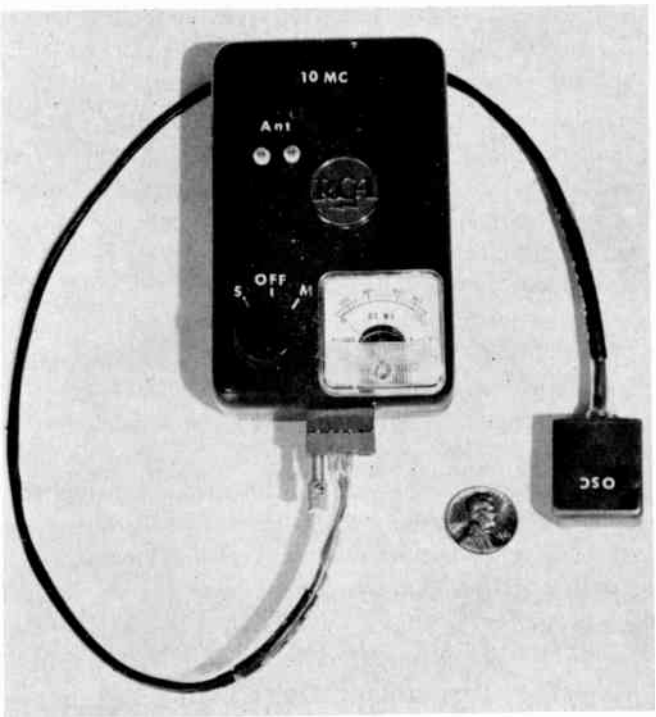

Fig. 5—Low-power, narrow-band, frequency sweep transmitter.

and weight. Therefore, the body heat of the transmitter operator was used to provide temperature stability. Published literature shows that there has been some success in applying this method of temperature control, usually by a type of "belt-buckle" oven enclosure, where one heat-conductive surface of a container is in direct contact with the abdominal skin. To obtain a greater operational convenience, several other placements were tested. Of the various methods investigated, the placement of the unit in the armpit showed the greatest convenience, and at the same time maintained the desired degree of temperature stabilization. It was found unnecessary to have direct contact between the skin and the crystal. Therefore, the complete oscillator circuit, including the quartz crystal was assembled in a small copper

enclosure. The unit is connected to the transmitter by a flexible cable and can be held comfortably in the operator's armpit while transmitting. Operation was judged to be quite convenient with this arrangement.

The oscillator circuit was especially designed to attain high stability. The crystal unit has a closely specified temperature "turning point" and resonant resistance. The "turning point" is controlled to match the human body temperature of 99°F. Crystal resistance is such as to assure oscillation for the worst-case condition.

The oscillator frequency must be swept at ±10 cps to fulfill the system requirements. For generating mark, the frequency must sweep down, and for space, up. The frequency sweeps are provided by applying linearized voltage functions to a semiconductor voltage-variable capacitor. Change in capacitance varies the series resonant frequency of the crystal the desired amount.

The remainder of the transmitter consists of a 3-stage, common-emitter, class C amplifier. The bandwidth is broadened to 3 megacycles to accommodate a wide range of carrier frequencies. The power output is approximately 100 milliwatts at a nominal battery voltage of 9 volts.

Various types of antennas, all of which were adjusted for a specific frequency to load the output of the transmitter properly, were tried. The most successful, yet most simple, was a quarter-wave vertical radiator with a driven quarter-wave element laid in the direction of desired transmission.

Preliminary Experiments

Before narrow-band long-distance communications experiments were attempted, feasibility tests were performed. Test equipment was constructed initially to facilitate measurement of Doppler shift by indirect means. The signal-to-noise (S/N) ratio was measured in the narrow-band and wide-band channels where the theoretical S/N improvement of the narrow-band channel was 40 db. A deterioration of this ratio was interpreted as indicating a degradation of received signal energy caused by the spectrum spread due to Doppler. Thus, if degradation occurred, it could be assumed that the Doppler shift was comparable to or exceeded the narrow bandwidth. The narrow-band channel had an effective noise bandwidth of 0.75 cps. In a series of measurements it was observed that no significant degradation of the 40-db S/N improvement occurred. It was concluded that Doppler shifts greater than 0.75 cps were, at most, infrequent.

In addition, a series of tests was made in which selected portions of radio station WWV sideband spectra were observed in the narrow pass band. It was possible in this manner to select signals radiated at milliwatt power levels in Washington, D. C., simulating low-power transmission between Washington and Tucson. These experiments provided typical S/N data. Actually, these data were considerably worse than those encountered in the actual system, since the receiver was obtaining age action from the WWV carrier rather than the side bands being observed. Since the side bands do not usually fade in phase with the carrier, this resulted in exaggerated fading.

Table I

Location	*Path Length (miles)*	*Frequency (mc)*
Dayton, Ohio	1550	13.35
Washington, D. C.	1900	15.97
Quantico, Va.	1900	15.97
Aberdeen, Md.	1900	15.97
Ft. Bragg, N. C.	1800	15.97

Long-Range Tests

Long-range tests were conducted by transmitting 5-bit messages from various eastern U.S. points to the narrow-band receiver in Tucson, Arizona. These tests proved successful from the locations given in Table I (all were made using a tree-supported quarter-wave vertical radiator with one or more ground radial wires). The received signal-to-noise ratio in these tests was consistently better than 30 db.

These tests demonstrated the effectiveness of the narrow-band milliwatt system for long-distance communications, since message transmission was essentially perfect. The few bits missed during tests were largely attributed to operator error. The number of tests were not, however, an adequate sample in view of the nature of the transmission medium. The tests were all based on a calculated path having a probability of success greater than 0.9. Thus, there is a significant indication that path performance is predictable.

Conclusions

The basis for reliable, long-range transmission of low bit rates by a compact low-power transmitter has been established. An experimental system has been designed, constructed, and tested. The system has been operated on long-haul paths.

RCA Technical Papers

Fourth Quarter, 1965

Any request for copies of papers listed herein should be addressed to the publication to which credited.

"Band Structure of Bismuth Telluride, Bismuth Selenide, and Their Respective Alloys," D. L. Greenaway and G. Harbeke, *Jour. Phys. and Chem. of Solids* (October) 1965

"Electron Spin Resonance of Tetraphenylporphine Chelates," J. M. Assour, *Jour. Chem. Phys.* (October) 1965

"Equipment Availability—An Improved Method of Prediction," W. J. C'Leary, *Trans. IEEE PTGAES* (October) 1965

"Gallium Arsenide MOS Transistors," H. Becke, R. Hall, and J. White, *Solid-State Electronics* (October) 1965

"Glass Compositions (New) Showing Electronic Conductivity," D. W. Roe, *Jour. Electrochem. Soc.* (October) 1965

"High-Energy Radiation Damage in Silicon Transistors," G. Brucker, W. Dennehy, and A. Holmes-Siedle, *Trans. IEEE PTGNS* (October) 1965

"The Inverted Pendulum," R. E. King, *Amer. Jour. Phys.* (Letters to the Editor) (October) 1965

"Isotropic Plasma Guide—TE_{11} Mode," T. W. Johnston, J. V. Gore, and F. J. F. Osborne, *Jour. Appl. Phys.* (Communications) (October) 1965

"New Excitation Mechanism for Magnetoacoustic Resonance in YIG," R. J. Ikola, *Jour. Appl. Phys.* (October) 1965

"Nodal Hydrogenic Wave Functions of Donors on Semiconductor Surfaces," J. D. Levine, *Phys. Rev.* (October) 1965

"Passive and Active Acoustics in Architectural Enclosures," H. F. Olson, *Jour. Aud. Eng. Soc.* (October) 1965

"Photoconductive Processes in Pure and Doped Triphenylene," N. Almeleh and S. Harrison, *Jour. Phys and Chem. Solids* (October) 1965

"Photoemission of Electrons from Silicon into Silicon Dioxide," R. Williams, *Phys. Rev.* (October) 1965

"Resolving Powers of Focussing Systems with Coherent Illumination," A. I. Carswell and C. Richard, *Applied Optics* (October) 1965

"Space-Charge Capacitance of an Intrinsic Semiconductor Film," F. P. Heiman and Coauthor, *Jour. Appl. Phys.* (October) ... 1965

"Surface Patterns Formed During the Application of High Currents and Magnetic Fields to N-InSb," M. Toda, *Appl. Phys. Ltrs.* (October) 1965

"A Transistorized Color Television Film Camera," D. M. Taylor, *Jour. S.M.P.T.E.* (October) 1965

"Unidirectional Wave Propagation in an Inhomogeneous Solid-State Plasma Waveguide," R. Hirota, *Jour. Phys. Soc. Japan* (October) 1965

"Electron Spin Resonance of Tetraphenylporphine Chelates," J. M. Assour, *Jour. Chem. Phys.* (1 October) 1965

"A Possible Lunar Magnetospheric Configuration," F. J. F. Osborne and M. P. Bachynski, *Jour. Geophysical Research* (October 1) 1965

"Measurement of the Longitudinal Component of the Electromagnetic Field at the Focus of a Coherent Beam," A. I. Carswell, *Phys. Rev. Letters* (18 October) 1965

"Audio Amplifier: Monolithic-Silicon Integrated-Circuit Type CA3007," *RCA Application Note ICAN-5037*, RCA Electronic Components and Devices, Harrison, N. J. (November) 1965

"DC Amplifier: Monolithic-Silicon Integrated-Circuit Type CA3000," *RCA Application Note ICAN-5030*, RCA Electronic Components and Devices, Harrison, N. J. (November) 1965

"DTL Gates (Low-Power): Monolithic-Silicon Integrated-Circuit Types CD2200, CD2201, and CD2203," *RCA Application Note ICAN-5024*, RCA Electronic Components and Devices, Harrison, N. J. (November) 1965

"ECCSL Gates (High-Speed): Monolithic-Silicon Integrated-Circuit Types CD2100 and CD2101," *RCA Application Note ICAN-5025*, RCA Electronic Components and Devices, Harrison, N. J. (November) 1965

"ECCSL Gates (Ultra-High Speed): Monolithic-Silicon Integrated-Circuit Types CD2150, CD2151, and CD2152," *RCA Application Note ICAN-5025*, RCA Electronic Components and Devices, Harrison, N. J. (November) 1965

"Electron Induced Surface Damage in Silicon Transistors," G. J. Brucker, W. Dennehy, and A. G. Holmes-Siedle, *Proc. IEEE* (Correspondence) (November) 1965

"Frequency Multiplication Using Transistors," H. C. Lee and R. Minton, *Microwaves* (November) 1965

"IF Amplifier: Monolithic-Silicon Integrated-Circuit Type CA-3002," *RCA Application Note ICAN-5036*, RCA Electronic Components and Devices, Harrison, N. J. (November) 1965

"A Large Signal Analysis Leading to Intermodulation Distortion Prediction in Abrupt Junction Varactor Upconverters," S. M. Perlow and B. S. Perlman, *Trans. IEEE PTGMTT* (November) 1965

"Microwave Scattering Measurements in the Rayleigh Region Using a Focused Beam System," A. I. Carswell, *Canadian Jour. Phys.* (November) 1965

"Memories in Present and Future Generations of Computers," J. A. Rajchman, *IEEE Spectrum* (November) 1965

"Modification of the Impulse Approximation for Ionization and Detachment Cross Sections," B. B. Robinson, *Phys. Rev.* (November) 1965

"Neutron Induced Displacement Damage in Integrated Circuits," J. A. McElroy, A. Boornard, and D. A. Gandolfo, *Proc. IEEE* (Correspondence) (November) 1965

"Operational Amplifier: Monolithic-Silicon Integrated-Circuit Types CA3008 and CA3010," *RCA Application Note ICAN-5015*, RCA Electronic Components and Devices, Harrison, N. J. (November) 1965

"The Past and Future of Test Equipment," J. R. Meagher, *Radio-Electronics* (November) 1965

"Progress in Solid-State Microwave Power Sources," F. Sterzer, *Trans. IEEE PTGMTT* (November) 1965

"RF Amplifiers: Monolithic-Silicon Integrated-Circuit Types CA3004, CA3005, and CA3006," *RCA Application Note ICAN-5022*, RCA Electron Components and Devices, Harrison, N. J. (November) 1965

"Solid State at Microwave Frequencies," H. K. Jenny, *Electronic Industries* (November) 1965

"Solvent Effects of the Spin Resonance Spectra of Cobalt Phthalocyanine," J. Assour, *Jour. Amer. Chem. Soc.* (November) 1965

"Stability Effects in MOS Enhancement Transistors," M. M. Mitchell and N. H. Ditrick, *Solid State Design* (November) 1965

Authors' Comment on "Threshold Dependency on Reabsorption Loss in Injection Lasers," M. F. Lamorte, T. Gonda, and H. Junker, *IEEE Jour. Quantum Electronics* (Correspondence) (November) 1965

"Video Amplifier: Monolithic-Silicon Integrated-Circuit Type CA3001," *RCA Application Note ICAN-5038*, RCA Electron Components and Devices, Harrison, N. J. (November) 1965

"We Got Across," F. D. Whitmore, *73* (November) 1965

"R-f Switching Matrix Cuts Out Crosstalk," W. Mergner, *Electronics* (November 1) 1965

"Determination of the Plasma Properties of High-Temperature Air by Microwave Attenuation Measurements," A. Boornard, *Appl. Phys. Ltrs.* (November 15) 1965

"The AFSCM 375-5 System Management and Coordination Process," R. C. Bradburn, Jr. and R. A. Stevens, *Signal* (December). 1965

Author's Comment on "Beam Noise Reduction in High Magnetic Fields," B. Vural, *Proc. IEEE* (Correspondence) (December) 1965

"The Bridge Cell—A New Superconductive Memory Cell for Random-Access Word-Organized Memories," R. W. Ahrons, *RCA Review* (December) 1965

"Canonical Tributary Networks," J. Sklansky and Coauthors, *Trans. IEEE PTGEC* (Short Notes) (December) 1965

"Cerenkov Interaction in a Uniformly Loaded Waveguide," J. J. Stekert, *RCA Review* (December) 1965

"Colorimetry in Color Television," J. F. Holahan, *Electronics World* (December) 1965

"Commercial Applications of Direct Energy Conversion," J. S. Greenberg, *Advanced Energy Conversion Jour.* (December). 1965

"Data Processing for the Mass Spectrographic Analysis of Solids," J. R. Woolston, *RCA Review* (December) 1965

"Deflection Yoke for 19-Inch 90° Color TV Picture Tubes," R. L. Barbin, *Trans. IEEE PTGBTR* (December) 1965

"Design and Performance of a 20-Kilowatt Latching Nonreciprocal X-Band Ferrite Phase Shifter," W. W. Siekanowicz, W. A. Schilling, T. E. Walsh, I. Bardash, and I. Gordon, *RCA Review* (December) 1965

"Electron-Hole Pair Creation in Gallium Phosphide by α Particles," B. Goldstein, *Jour. Appl. Phys.* (December) 1965

"Gain-Bandwidth Limitations and Optimum Design of Parametric RC Converters," J. Klapper and Coauthor, *Jour. Frank. Inst.* (December) 1965

"Manufacture of Color Picture Tubes," J. F. Holahan, *Electronics World* (December) 1965

"Memory Devices for Modern Computer Memories," A. C. Knowles, *Electronic Industries* (December) 1965

"On the Nature of Information—an Application of Entropy," M. Grossman, *IEEE Spectrum* (December) 1965

"Nomograph of the Temperature Dependence of the Fermi Level in a Degenerate Parabolic Band," J. I. Pankove and E. K. Annavedder, *Jour. Appl. Phys.* (Communications) (December) .. 1965

"Performance Analysis of 3- and 4-Coil FM Tuners Using RCA High-Frequency Transistors," R. V. Fournier, C. H. Lee, and R. T. Peterson, *Trans. IEEE PTGBTR* (December) 1965

"Remote Cable Pressure Monitoring System," J. H. Wolff, H. E. Goldstine, and E. Cohen, *Trans. IEEE PTGCOM* (December) 1965

"The Role of Surface States in the Photoelectronic Properties of Insulating Cadmium Sulfide Crystals," P. Mark, *RCA Review* (December) 1965

"A Simplified Approach to the Analysis of Electromagnetic-Wave Propagation Characteristics of Plasma-Coated Surfaces," L. W. Zelby, *RCA Review* (December) 1965

"The Staffing and Operation of a Technical Papers Support Group," C. W. Fields, *Trans. IEEE PTGEWS* (December) 1965

"Symbols for Electricity and Electronics," H. L. Cook, *Trans. IEEE PTGEWS* (December) 1965

"Utilization of the t^* Partial Switching Properties of Ferroelectrics in Memory Devices," G. W. Taylor, *Trans. IEEE PTGEC* (December) 1965

"New Target for Radar: Sharper Vision with Optics," A. J. Talamini, Jr. and E. C. Farnett, *Electronics* (December 27) 1965

"Excitation of Cyclotron Harmonics in Warm Plasmas," T. W. Johnston and I. P. Shkarofsky, *Bull. Amer. Phys. Soc.*, Ser. II, Vol. 10, No. 2 1965

AUTHORS

I. ABEYTA graduated with a B.S.E.E. from the University of New Mexico in 1949. From 1949 to 1951, he worked for Hemez Mountains Power Company. From 1951 to 1957, he was with the Signal Corps at Fort Monmouth, New Jersey, doing research and development work on microwave components and on radar vulnerability and countermeasures. In 1957, Mr. Abeyta joined RCA as a microwave engineer. In late 1957, he transferred to the Advanced Computer group of Electronic Data Processing, which later became part of RCA Defense Electronics Products, Applied Research. Here he has been engaged in the advanced development of computer circuits and computer memories.

Mr. Abeyta is a member of the Institute of Electrical and Electronics Engineers and of the Professional Group on Electronic Computers (PGEC).

JAMES G. ARNOLD received the B.S.E.E. from Alabama Polytechnic Institute in 1951. He joined RCA that year as an engineer in the Radiation Engineering Department. He has since been engaged in design and development of communications equipment and systems. Mr. Arnold is presently with Bell Aerosystems Co., Tucson, Arizona.

D. M. CHAUVIN received a B.S. in Electrical Engineering in 1942 from Louisiana State University and A and M College. From 1942 to 1946 he served in the U.S. Army Signal Corps as a Radio Officer. From 1946 to 1958 he was employed by Westinghouse Electric Corporation, Baltimore, Maryland, working on the design of communications apparatus. From 1958 to 1961 he was employed by Goodyear Aerospace Corporation in Phoenix, Arizona, performing research and design on high-resolution aircraft radar. He joined RCA in Tucson, Arizona, as a Senior Project Member, Technical Staff, in 1961. While there, he worked on a support information network and remote (transmission line) pressure monitor, single sideband transceiving equipments, and long distance digital communications system. In 1965 he joined Autonetics, Anaheim, California.

A. DANFORTH COPE graduated from Colgate University in 1938 and continued in graduate study at Yale University (Physics). He joined the Radio Corporation of America in 1941 and worked at Harrison, N. J. and Lancaster, Pa. Since 1949, he has been at the David Sarnoff Research Center, Princeton, N. J. During most of this period his area of interest has been phototube and camera tube design and performance problems. From 1949 to 1961, Mr. Cope worked on photoconductor materials suitable for application to camera tubes. At present he is associated with the RCA Astro-Electronics Division, Physical Research Laboratory, carrying out research in adapting scanning photosensors to the specific needs of space instruments. This has included such diverse problems as soft x-ray solar imaging, long integration television systems applicable to astronomy, and meteorological satellite sensors.

Mr. Cope is a member of Phi Beta Kappa, Sigma Xi, and the Optical Society of America.

KARL G. HERNQVIST graduated in Electrical Engineering at the Royal Institute of Technology, Stockholm, Sweden, in 1945. He received the Licentiate of Technology degree in 1951 and the Doctor of Technology degree in 1959. From 1946 to 1952 he was employed by the Research Institute of National Defense in Stockholm, working in the field of microwave electronics. From 1948 to 1949, Dr. Hernqvist was a trainee of the American-Scandinavian Foundation at RCA Laboratories, to which he returned in 1952; he is presently working on gas lasers. Dr. Hernqvist is a Member of the Institute of Electrical and Electronics Engineers and Sigma Xi.

JOHN C. JOHNSON received the B.S.E.E. from the University of Nebraska in 1951 and the M.S.E.E. from the University of Arizona in 1961. He joined RCA Electronic Components and Devices, Lancaster, Pa., where he worked on manufacturing and test equipment for electron tubes. From 1959 to 1965, he was with RCA Communications Systems Division, Tucson, Arizona, where he contributed to the design of the Support Information Network of Minuteman and various other unusual radio communications systems. Since 1965, he has been with Motorola, Inc., Western Military Electronic Center, Scottsdale, Arizona.

He is a member of Pi Mu Epsilon, Eta Kappa Nu, the American Society of Professional Engineers, and is a registered engineer in Pennsylvania and Arizona.

RALPH E. JOHNSON received the B.S. degree in Electrical Engineering from the University of Pittsburgh in 1952. He joined RCA Electronic Components and Devices the same year as a design engineer. He worked initially on the development of long-persistence-screen indicators for radar service, and later on image-orthicon design. From 1950 to 1957, as a field sales engineer he conducted educational seminars for camera-tube users and assisted them with field problems. In 1957, he was appointed Administrator, Sales Engineering Services by the RCA Distributor Products Sales Division. He is currently in the Camera-Tube Operations Division at Lancaster, Pennsylvania, working on applications for camera tubes.

M. M. KAUFMAN received a B.E.E. from the City College of New York in 1956 and an M.S.E.E. from the University of Pennsylvania in 1960. Upon receiving his undergraduate degree, Mr. Kaufman joined RCA where he has worked on memory systems utilizing diodes and capacitor storage, transistorized apertured ferrite-plate storage, transistorized peripherial circuits, tunnel-diode storage circuits and, most recently, snap diodes and laminated ferrites. He is a member of Eta Kappa Nu.

P. D. LAWRENCE received an A.B. degree majoring in Physics from Bowdoin College in June 1961. At that time he joined the RCA Memory Products Operation, Needham, Mass. His duties have been concentrated on evaluation of ferrite cores and laminates, and development of stack electrical organization for high-speed and very high-speed memory operation.

JULES D. LEVINE received the B.S.M.E. degree at Columbia in 1959. He then attended M.I.T. where he obtained an S.M. degree in 1961 and a Ph.D. degree in 1963; his thesis topic was based on a new theoretical analysis of adsorption phenomena on metals. For this he received the G.E. Annual Award for originality and creativity in research. Since joining RCA Laboratories in 1963 he has extended his theoretical studies to models of adsorption and surface states on metals, semiconductors, and insulators. Also he is involved in experimental studies on cesium adsorption and cesium compounds. Dr. Levine is on the planning committee for the Thermionic Energy Conversion Specialists Conference and he is a member of Tau Beta Pi, Sigma Xi, and the American Physical Society.

EDUARD LUEDICKE received his degrees in Electrical Engineering from the Technical University at Berlin and at Karlsruhe, West Germany—the Diplom Engineer in 1950, the Doctor degree (with honor) in 1955. From 1940 to 1945, he was a development engineer for radar and guidance techniques in the Telefunke Laboratories, Berlin, Germany and from 1951 to 1955 a development engineer in the field of industrial television at the Zentral Laboratorium of Siemens and Halske in Karlsruhe, West Germany. In 1955 he joined the RCA Victor Company Ltd., Montreal, Canada as a development engineer for television components. He was appointed manager of engineering of the RCA Victor Ranfrew Plant in Canada in 1956. In 1959, Dr. Luedicke transferred to the RCA Semiconductor and Materials Division, Somerville, N. J., where he worked on micromodules and from 1960 to 1961 on a computer in the 1000 megacycle range. In 1962 he transferred to the Astro-Electronics Division and is presently working in the field of camera-tube research.

Dr. Luedicke is a member of the Fernseh Technische Gesellschaft, Germany, and the Society of Motion Picture and Television Engineers.

J. K. OLIVER, JR., received the B.S. and M.S. degrees in Electrical Engineering from the University of Pennsylvania in 1956 and 1958. Mr. Oliver joined the RCA Communications Systems Division, Tucson, Arizona, in June of 1958. He has worked mostly in the field of radio frequency interference, propagation and communication systems engineering studies. During the past year and one-half he was responsible for the design and development of the 250 kiloband Saturn V Diphase Data Modem used in the ground checkout of the Saturn V vehicle. He is presently with Bell Aerosystems Co., Tucson, Arizona. Mr. Oliver is a member of the Institute of Electrical and Electronics Engineers, Sigma Tau, American Radio Relay League and is a registered professional engineer in the state of Arizona.

C. W. RENO received the B.A. and the M.A. degrees in physics from the University of Kansas in 1960 and 1962, respectively. He was a teaching assistant during part of his graduate studies, and he wrote his thesis on paramagnetic resonance in frozen solutions. Since joining RCA Defense Electronic Products, Applied Research, in 1962, Mr. Reno has worked exclusively on laser research. His main interest has been CW and high-pulse-rate solid-state oscillators for use in the laser radar programs. Recent work includes optical alignment of Gemini laser transmitters, development of laser arrays and selection of high performance laser diodes for these devices, and development of the solar-pumped modulated laser.

ALBERT ROSE received the A.B. degree from Cornell University in 1931 and the Ph.D. degree in Physics in 1935. From 1931 to 1934 he was a teaching assistant at Cornell University. From 1935-1942 he was with the RCA Tube Division in Harrison, N. J., and since 1942 he has been associated with RCA Laboratories at Princeton, N. J. From 1955 to 1957 he directed the research at Laboratories RCA, Ltd., in Zurich, Switzerland. Dr. Rose is a Fellow of the Institute of Electrical and Electronics Engineers and of the American Physical Society.

A. SCHNAPF received his B.S.M.E. degree from the City College of New York in 1948 and his M.S.M.E. degree from Drexel Institute of Technology in 1953. From 1948 to 1950, he was with Goodyear Aircraft Corporation as a development engineer. From 1950 to 1958, he was with the RCA Airborne Systems Department where he managed the development and design of the Automatic MOD II Shoran Bomb Systems. He was also responsible for the design and integration of an airborne weapon system for Mach 2 fighter interceptors. Mr. Schnapf joined the RCA Astro-Electronics Division, Princeton, N. J., in 1958 to work on the TIROS project. He is presently the TIROS Project Manager, as well as having responsibility for other space programs and activities at RCA.

Mr. Schnapf is a professional engineer in the State of New Jersey and a senior member of the AIAA.